



Provided by the author(s) and University of Galway in accordance with publisher policies. Please cite the published version when available.

Title	An experimental and computational investigation into procedural complications relating to transcatheter aortic heart valves
Author(s)	McGee, Orla
Publication Date	2018-02-20
Publisher	NUI Galway
Item record	http://hdl.handle.net/10379/14977

Downloaded 2024-04-25T10:29:07Z

Some rights reserved. For more information, please see the item record link above.



An Experimental and Computational Investigation into Procedural Complications Relating to Transcatheter Aortic Heart Valves

Orla M. McGee B.E. (2014)



A thesis submitted to the National University of Ireland as fulfilment of the requirements for the degree of Doctor of Philosophy

2018

Biomedical Engineering
College of Engineering and Informatics
National University of Ireland, Galway

Supervisor of Research: Prof. Laoise M. McNamara

Abstract

Although transcatheter aortic valves are widely used for treatment of high to medium risk patients with severe aortic stenosis, there are still many associated procedural complications. In particular, new on-set conductance interference is a common complication of transcatheter aortic valve implantation, but the exact cause is unknown. It has been proposed that this is due to injury in the vicinity of the heart's conductance system, which is located at the base of the interleaflet triangle between the non-coronary and the right coronary aortic sinus. However, a further understanding of the levels of stress in the vicinity of the conductance system after valve deployment and the impact of positioning on these stresses is required. Additionally, the impact of calcification on the tissue-stent interaction has not yet been quantified. In particular it is not yet known what role the calcification plays in securing the stent and preventing migration *in vivo*. Finally, as transcatheter valves are being touted as a treatment for younger patient cohorts, there is further knowledge required regarding the sizing of transcatheter valves in bicuspid patients. Therefore, the objectives of this thesis are to (1) develop a finite element framework simulating deployment of a Lotus™ valve in a patient-specific aortic root to investigate the impact of stent implantation depth and orientation on stress related to conductance interference, (2) quantify the impact of calcification on the tissue-stent interaction and (3) investigate valve sizing in a stenosed bicuspid aortic valve. The results of this thesis provide evidence that sub-annular positioning leads to higher stress in the vicinity of the heart's conductance system and demonstrate that preoperative planning of the Lotus™ valve stent orientation within the aortic sinus has the potential to minimise conductance interference. It was shown that calcification increases the coefficient of friction in the interaction between the aortic

root and stent further securing transcatheter aortic valves in place. Finally, the results of this thesis inform device positioning and patient sizing for the Lotus™ valve and provide knowledge for the development of next-generation transcatheter aortic valve devices.

Publications

The following publications have been generated from this thesis:

Published Journal Articles:

- O. M. McGee, P. S. Gunning, A. McNamara, and L. M. McNamara, "The impact of implantation depth of the Lotus™ valve on mechanical stress in close proximity to the bundle of His," *Biomechanics and Modeling in Mechanobiology*, 2018/08/20 2018.
- McGee, O.M., Sun. W., McNamara, L.M. Quantification of the Effect of Calcification on the Tissue-Stent Interaction in a Stenosed Aortic Root, Accepted for Publication in the *Journal of Biomechanics*, 2018

Journal Articles in Submission/Preparation:

- O. M. McGee, A. McNamara, and L. M. McNamara. The Relationship between Lotus™ Valve Stent Orientation and New On-Set Left Bundle Block Branch
- O. M. McGee, A. McNamara, and L. M. McNamara A Patient-Specific Model Investigating Sizing of Transcatheter Valves in a Stenosed Bicuspid Heart Valve.

Conference Presentations:

- **McGee, O.M.***, Harrison, N., McNamara, L.M. Image-Based Modelling and the use of a Patient-Specific Approach for Transcatheter Aortic Valve Simulation. *Cardiac and Computational Modelling*. July 2018, Galway, Ireland. (Invited Speaker)
- **McGee, O.M.**, Sun. W., McNamara, L.M. An Investigation into the Relationship between Transcatheter Valves and Conductance Interference. 8th

World Congress of Biomechanics. July 2018, Dublin, Ireland. (Poster Presentation).

- **McGee, O.M.***, Sun. W., McNamara, L.M. Quantification of the Effect of Calcification on the Tissue-Stent Interaction in a Stenosed Aortic Root. *Shape Memory and Superelastic Technology Ireland*. May 2018, Galway, Ireland. (Invited Speaker)
- **McGee, O.M.***, McNamara, L.M. An Investigation into the Relationship between Transcatheter Valves and Conductance Interference. *Biomedical Engineering in Ireland 24 Conference*, January 2018, Dublin, Ireland. (Podium presentation)
- **McGee, O.M.***, Sun. W., McNamara, L.M. Quantification of the Effect of Calcification on the Tissue-Stent Interaction in a Stenosed Aortic Root. *Summer Biomechanics, Bioengineering and Biotransport Conference*, June 2017, Tucson, AZ, USA. (SB3C Student Paper Competition)
- **McGee, O.M.***, Gunning, P.S., Sun. W., McNamara, L.M. Quantification of the Effect of Calcification on the Tissue – Stent Interaction in a Stenosed Aortic Root. *Sir Bernard Crossland Symposium*, April 2016, Belfast, Ireland. (Poster Competition 2nd Place)
- **McGee, O.M.***, Sun. W., McNamara, L.M. Investigation into the Role of Calcification in the Tissue-Stent Interaction in a Stenosed Aortic Root. *NUIG/UL Research Day*, April 2017, Galway, Ireland. (Theresis Competition)
- **McGee, O.M.***, Sun. W., McNamara, L.M. Quantification of the Effect of Calcification on the Tissue-Stent Interaction in a Stenosed Aortic Root. *Biomedical Engineering in Ireland 23 Conference*, January 2017, Belfast, Ireland. (EI Medal Presentation)

- **McGee, O.M.***, Gunning, P.S., McNamara, L.M. A Computational Investigation of the positioning of Transcatheter Aortic Heart Valves to Enhance Long-Term Performance. *Summer Biomechanics, Bioengineering and Biotransport Conference*, June 2016, National Harbour, MD, USA. (Podium presentation)
- **McGee, O.M.**, Gunning, P.S., McNamara, L.M. The Effect of Positioning of Transcatheter Aortic Heart Valves on Stress: A Computational Approach. April 2016 *NUIG/UL Research Day*, Limerick, Ireland. (Poster Presentation)
- **McGee, O.M.***, Gunning, P.S., McNamara, L.M. Computational Characterization of Transcatheter Aortic Valve Positioning. *Sir Bernard Crossland Symposium*, April 2016, Belfast, Ireland. (Poster Competition with Podium Presentation - 2nd Place)
- **McGee, O.M.**, Gunning, P.S., McNamara, L.M. Computational and Experimental Characterization of Bioprosthetic Heart Valve Positioning to Enhance Long-Term Performance. *Heart Valve Society*, March 2016, New York, USA. (Electronic Poster Presentation Competition)
- **McGee, O.M.***, Gunning, P.S., McNamara, L.M. A Computational Investigation of the positioning of Transcatheter Aortic Heart Valves to Enhance Long-Term Performance. *Biomedical Engineering in Ireland 22 Conference*, January 2016, Galway, Ireland. (Podium presentation)
- **McGee, O.M.**, Gunning, P.S., McNamara, L.M. Computational and Experimental Characterization of Bioprosthetic Heart Valve Positioning to Enhance Long-Term Performance. *IISSEC Mechanics Symposium*, November 2015, Dublin, Ireland. (Poster Presentation)

- **McGee, O.M.***, Gunning, P.S., McNamara, L.M. Computational and Experimental Characterisation of Bioprosthetic Heart Valve Positioning to Enhance Long-Term Performance. *NUIG/UL Research Day*, April 2015 Galway, Ireland. (Thesis Competition)
- **McGee, O.M.***, McNamara, L.M. Computational and Experimental Characterisation of Bioprosthetic Heart Valve Positioning to Enhance Long-term Performance. *Biomedical Engineering in Ireland 21 Conference*, January 2014, Maynooth, Ireland. (Podium presentation)

(*Oral presentation of a paper at conference)

Acknowledgements

Firstly, I would like to express my sincerest thanks to Professor Laoise McNamara for encouraging me to pursue a Ph.D. and for the continuous support throughout the past four years. I am deeply grateful to her for consistently pushing me to strive for higher standards of research and for providing constant drive and motivation. I would also like to express my thanks to Adrian McNamara for his wealth of insight and knowledge that he has shared with me. Additionally, I'd like to thank all the members of the structural heart team at Boston Scientific who have assisted me over the past few years. I would like to extend my gratitude to Dr Wei Sun for welcoming me into the Tissue Mechanics Lab in Georgia Tech and providing me with a broader research experience. I would like to particularly acknowledge the members of the Mechanobiology and Medical Device Research Group who have worked alongside me over the past four years; especially my soul mate Irene 'Simfu' and Myles who have been there since day one. Thanks for always putting a smile on my face whether you meant to or not. To Ikay, Kelsey, Andres, Vrishank, Shelly, Eric and Caitlin, thank you for making my time at Georgia Tech unforgettable. For all the nights out, hikes, road trips and for all the lifts around Atlanta, thank you all. A huge thanks to the extensive group of engineering postgrads who have join me throughout the years for all the half ten tea breaks, post-conference holidays, nights out, tag rugby matches and games nights, you have all made this PhD a lot more enjoyable. I have to specially mention Ciara, Eimear, Hollie, Laura, Sarah and Emily K (our pretend engineer) for the holiday adventures, road trips and advancing my knowledge of botanicals.

To my closest friends; Emily, thanks for joining me on my adventures, allowing me to expand my scratch map and always being at the other end of the phone. To Aisling, Ciara, Deirbhle, Denise, Jenny, Louise, Orlaith, Rosie, Sinead and Tracy, my 'Pineapples'. I couldn't ask for a better group of girls and I can't thank you all enough for providing me with some much-needed distraction over the past few years.

To my family, Tom and Diarmuid, thanks for keeping me grounded. And finally, Mum and Dad thanks for being my on and off housemates throughout my extended college experience, for all the advice and constant support, I couldn't have done this without you. This Thesis is dedicated to both of you.

Nomenclature

Roman Letters

D/d	diameter
e	eccentricity
E	Young's modulus
F	Force
p	Pressure
R	Radius
t	Time

Greek Letters

μ	Coefficient of Friction
σ	Stress
ν	Poisson's Ratio

Acronyms

AS	Aortic Stenosis
AV	Atrioventricular
BAV	Bicuspid Aortic Valve
BHV	Bioprosthetic Heart Valve
CFD	Computational Fluid Dynamics
CT	Computed Tomography
EOA	Effective Orifice Area

FE	Finite Element
FEA	Finite Element Analysis
HGO	Holzapfel-Gasser-Ogden
LBBB	Left Bundle Branch Block
LVOT	Left Ventricular Outflow Tract
MHV	Mechanical Heart Valve
MSCT	Multi-Slice Computed Tomography
PVL	Paravalvular leakage
PIV	Particle Imaging Velocity
PPM	Permanent Pacemaker Implantation
SAVR	Surgical Aortic Valve Replacement
STJ	Sinotubular Junction
TAVI	Transcatheter Aortic Valve Implantation
TAV	Transcatheter Aortic Heart Valve
TVG	Transvalvular Pressure Gradient

Table of Contents

Abstract	i
Publications	iii
Acknowledgements	vii
Nomenclature	ix
Table of Contents	xi
Table of Figures	xvii
Table of Tables.....	xxiii
1 Introduction.....	24
1.1 Thesis Objectives and Hypothesis.....	30
1.2 Thesis Structure and Overview	31
2 Literature Review	33
2.1 The Heart and Heart Valves	33
2.1.1 Aortic Root and Valve Anatomy.....	34
2.1.2 Aortic Valve Tissue.....	37
2.2 Biomechanics of the Aortic Valve	39
2.2.1 Fluid Mechanics and Hemodynamics	40
2.2.2 Solid Mechanics	41
2.3 Aortic Stenosis	44
2.4 Surgical Aortic Valve Replacement	46
2.4.1 Mechanical Heart Valves	46

2.4.2	Bioprosthetic Heart Valves	49
2.5	Transcatheter Aortic Valve Intervention	51
2.5.1	Types of Transcatheter Aortic Valves.....	52
2.5.2	Complications of Transcatheter Aortic Valve Implantation	55
2.5.3	Procedural Considerations of Transcatheter Aortic Valves	63
2.6	Biomechanical Evaluation of Transcatheter Aortic Valves	64
2.6.1	Experimental Studies	64
2.6.2	Computational Studies	67
2.7	Summary	78
3	The Impact of Implantation Depth of the Lotus™ Valve on Mechanical Stress in Close Proximity to the Bundle of His	80
3.1	Introduction	80
3.2	Materials and Methods	84
3.2.1	Aortic Root Model	84
3.2.2	Lotus™ Valve Model	85
3.2.3	Constitutive Models	86
3.2.4	Boundary Conditions	88
3.2.5	Eccentricity	89
3.3	Results	92
3.3.1	Eccentricity	92
3.3.2	Aortic Root Peak Stress and Stress Distribution.....	93
3.4	Discussion	97

3.5	Conclusion.....	102
4	<i>An In Vitro Model Quantifying the Effect of Calcification on the Tissue–Stent Interaction in a Stenosed Aortic Root</i>	103
4.1	Introduction	103
4.2	Materials and methods.....	106
4.2.1	Stent Radial Expansion Experiment	106
4.2.2	Root – Stent Interaction Experiment.....	108
4.2.3	Statistical Analysis	112
4.3	Results	112
4.3.1	Radial Force	112
4.3.2	Stent Eccentricity	113
4.3.3	Pullout Test and Friction Coefficient.....	114
4.4	Discussion	115
5	The Relationship between Lotus Valve Stent Orientation and New On-Set Left Bundle Block Branch	121
5.1	Introduction	121
5.2	Materials and Methods	124
5.2.1	Aortic Root Model	124
5.2.2	Lotus™ Valve Model.....	124
5.2.3	Constitutive Models	125
5.2.4	Boundary and Loading Conditions	126
5.3	Results	129

5.3.1	Model validation	129
5.3.2	Stress in the Interleaflet Triangle	131
5.3.3	The Impact of Stent Rotation	132
5.4	Discussion	134
5.5	Conclusion.....	138
6	A Patient-Specific Model of Transcatheter Valve Replacement in a Bicuspid Heart Valve.	139
6.1	Introduction	139
6.2	Materials and Methods	142
6.2.1	Aortic Root Model	142
6.2.2	Lotus™ Valve Model.....	143
6.2.3	Constitutive Models	143
6.2.4	Boundary and Loading Conditions	143
6.3	Results	144
6.3.1	Eccentricity	145
6.3.2	Stress	146
6.3.3	Paravalvular Leakage.....	147
6.4	Discussion	148
6.5	Conclusion.....	151
7	Discussion and Conclusion.....	153
7.1	Introduction	153
7.2	Main Findings of the Thesis.....	153

7.2.1	Hypothesis 1: Supra-annular positioning reduces stress in the interleaflet triangle in which the conductance system (Bundle of His) resides	154
7.2.2	Hypothesis 2: Calcification secures the TAV in place by increasing the friction in the interaction between the TAV stent and a stenosed aortic root	155
7.2.3	Hypothesis 3: Orientation of the Lotus valve impacts the stress in the vicinity of the bundle of His and can induce conductance interference	157
7.2.4	Hypothesis 4: Bicuspid patients with stenosed aortic valves can be effectively treated using the Lotus™ Valves in terms of stent eccentricity and tissue stress using traditional device sizing.	158
7.3	Implications of this Thesis in the field of Transcatheter Valves	159
7.4	Future Recommendations	165
7.4.1	Further Investigation of the Mechanism behind Conductance Disturbances.....	165
7.4.2	Further Consideration for Calcification Severity and Patterns	167
7.5	Conclusion.....	167
	References	168
	Appendix I: Theoretical Framework.....	189
A.1	Introduction	189
A.2	Notation	189
A.3	Finite Element Analysis of Solid Structures	190
A.3.1	Fundamental Principles and Theoretical Formulations	190

A.3.2	Finite Element Method.....	195
A.3.3	Constitutive Models	201
A.4	Summary	205

Table of Figures

FIGURE 2.1: (A) THE VALVES OF THE HEART IN (B) SYSTOLE AND DIASTOLE (ADAPTED FROM HTTPS://SMART.SERVIER.COM).	33
FIGURE 2.2: (A) THE HEART'S CONDUCTANCE SYSTEM, (B) THE AORTIC VALVE COMPLEX, WHERE THE VALVULAR LEAFLETS ARE ATTACHED ALONG THE VENTRICULOARTERIAL JUNCTION (VAJ), L IS THE LEFT CORONARY SINUS, R IS THE RIGHT CORONARY SINUS, N IS THE NON-CORONARY SINUS, VS IS THE VENTRICULAR SEPTUM, MV IS THE MITRAL VALVE, MS IS THE MEMBRANE SEPTUM AND LBB THE LEFT BUNDLE BRANCH, LFT AND RFT ARE THE RIGHT AND LEFT FIBROUS TRIGONES (ADOPTED FROM; HTTPS://SMART.SERVIER.COM , [64]).	36
FIGURE 2.3: SCHEMATIC OF (A) THE CELLULAR ARCHITECTURE OF A NORMAL AORTIC VALVE, (B) THE ARCHITECTURE OF COLLAGEN AND ELASTIN IN SYSTOLE AND DIASTOLE, (C) THE BIOMECHANICAL RESPONSE OF COLLAGEN AND ELASTIN DURING VALVE MOTION (IMAGE ADAPTED FROM [70, 71]).	39
FIGURE 2.4: FLOW VELOCITY AND STREAMLINES THROUGH THE AORTIC VALVE DURING, THE ACCELERATION PHASE (T=0.30 S), AT PEAK SYSTOLE (T=0.43 S) AND DURING THE DECELERATION PHASE (T=0.63 S) [75].	41
FIGURE 2.5: WIGGERS DIAGRAM ILLUSTRATING AORTIC PRESSURE, ATRIAL PRESSURE, AND VENTRICULAR PRESSURE VERSUS TIME (ADAPTED FROM WWW.WIKIWAND.COM).	42
FIGURE 2.6: THE MECHANICAL FORCES EXPERIENCED BY THE VALVE LEAFLETS DURING PEAK SYSTOLE AND DIASTOLE [78].	44
FIGURE 2.7: TYPES OF SURGICAL VALVES. MECHANICAL VALVES (A-C) INCLUDE A, CAGED BALL VALVE (STARR-EDWARDS); B, MONOLEAFLET VALVE (MEDTRONIC HALL); C, BILEAFLET VALVE (ST JUDE); BIOPROSTHETIC VALVES (E-F) D, STENTED PORCINE BIOPROSTHESIS (MEDTRONIC MOSAIC); E, STENTED PERICARDIAL BIOPROSTHESIS (CARPENTIER-EDWARDS MAGNA); F, STENTLESS PORCINE BIOPROSTHESIS (MEDTRONIC FREESTYLE); (ADAPTED FROM [12]).	51

FIGURE 2.8: TRANSCATHETER VALVE TECHNOLOGIES INCLUDE: (A) EDWARDS SAPIEN XT (EDWARDS LIFESCIENCES, IRVINE, CALIFORNIA); (B) SAPIEN 3 (EDWARDS LIFESCIENCES, IRVINE, CALIFORNIA); (C) LOTUS (BOSTON SCIENTIFIC INC, NATICK, MASSACHUSETTS); (D) INOVARE VALVE (BRAILE BIOMEDICA INC, SÃO JOSÉ DO RIO PRETO, BRAZIL); (E) MELODY (MEDTRONIC, MINNEAPOLIS, MINNESOTA); (F) DIRECT FLOW (DIRECT FLOW MEDICAL INC, SANTA ROSA, CALIFORNIA); (G) COREVALVE (MEDTRONIC, MINNEAPOLIS, MINNESOTA); (H) EVOLUT R (MEDTRONIC, MINNEAPOLIS, MINNESOTA); (I) ACURATE TA SYSTEM (BOSTON SCIENTIFIC INC, NATICK, MASSACHUSETT); (J) ENGAGER (MEDTRONIC, MINNEAPOLIS, MINNESOTA); (K) PORTICO (ST. JUDE MEDICAL INC., ST. PAUL, MINNESOTA); (L) JENAVALVE (JENAVALVE INC, MUNICH, GERMANY) [108].
..... 54

FIGURE 2.9: REGURGITATION MECHANISMS FOR TAVI (A) DEPICTS TRANSVALVULAR LEAKAGE OCCURRING DUE TO LEAKAGE THROUGH THE VALVE AND (B) DEPICTS PARAVALVULAR LEAKAGE OCCURRING BETWEEN THE PROSTHESIS AND AORTIC ANNULUS [122]. 56

FIGURE 2.10: A FINITE ELEMENT ANALYSIS PREDICTING AORTIC ROOT RUPTURE DUE TO THE DISPLACEMENT OF CALCIFICATION INTO THE LEFT CORONARY SINUS [39]. 59

FIGURE 2.11: FORCES EXPERIENCED BY A TAV IN (A) SYSTOLIC EJECTION AND (B) DIASTOLIC CLOSURE. WHERE F_D IS THE PRESSURE FORCE ACTING ON THE VALVE, F_{AO} IS THE RADIAL FORCE OF THE VALVE ON THE AORTIC ROOT, F_{TOR} IS THE TORSIONAL FORCE ON THE STENT DUE TO THE MOTION OF THE AORTIC ANNULUS AND ΔP IS THE PRESSURE GRADIENT ACROSS THE CLOSED VALVE [9]. 60

FIGURE 2.12: (A) CIRCULAR VALVE STENT WITH NO LEAFLET DISTORTION PRESENT AND (B) ELLIPTICAL STENT WITH VISIBLE LEAFLET DISTORTION [141]. 62

FIGURE 2.13: IMAGE FROM GUNNING *ET AL.* DEPICTING THE 99TH PERCENTILE MAXIMUM PRINCIPAL STRESS IN TAVI LEAFLETS UNDER IDEALIZED DEPLOYMENT CONDITIONS: (A) CIRCULAR, (B) ECCENTRIC-PARALLEL AND (C) ECCENTRIC-PERPENDICULAR AND UNDER REALISTIC DEPLOYMENT CONDITIONS IN (D) REALISTIC-PARALLEL, (E) REALISTIC-PERPENDICULAR AND (F) REALISTIC COMMISSURE ALIGNED ORIENTATIONS. WHERE THE RED BOXES INDICATE REGIONS OF PEAK STRESS [29]. 73

FIGURE 2.14: SIMULATION RESULTS FROM AURICCHIO <i>ET AL.</i> : THE VON MISES STRESSES ON THE AORTIC ROOT WALL AND STENT STRUTS ARE REPRESENTED (A) AFTER DISTAL POSITIONING	74
FIGURE 2.15: VARIOUS STAGES OF THE STENT DEPLOYMENT FOR THE THREE DEPLOYMENT LOCATIONS. VON MISES CONTOURS ARE PLOTTED ON THE NATIVE LEAFLETS (SECOND AND THIRD ROWS) AND CALCIUM DEPOSITS (FOURTH ROW) [171].....	76
FIGURE 2.16: CONTOUR PLOTS DEPICTING THE VON MISES STRESS DISTRIBUTION ON THE AORTIC ROOT WALL INDUCED BY STENT EXPANSION IS IN A : (A) RIGID CONFIGURATION; (B) AN ISOTROPIC LINEAR ELASTIC; (C) A NON-LINEAR ISOTROPIC HYPERELASTIC (D) AN ANISOTROPIC HOLZAPFEL–GASSER–ODGEN (HGO) MATERIAL MODEL. STRESS IS EXPRESSED IN MPA [176].	78
FIGURE 3.1: (A) SCHEMATIC OF THE HEART’S CONDUCTANCE SYSTEM (B) SCHEMATIC OF THE AORTIC VALVE AND THE REGION OF THE CONDUCTANCE SYSTEM PASSING IN CLOSE PROXIMITY TO THE AORTIC VALVE COMPLEX (C) THE PATIENT-SPECIFIC MODEL OF AORTIC SINUS WITH SCHEMATIC REPRESENTING THE AV NODE AND LEFT BUNDLE BRANCH AND THE PATH WHERE THEY PASS IN CLOSE PROXIMITY TO THE VALVE COMPLEX.....	82
FIGURE 3.2: CREATION OF THE PATIENT-SPECIFIC AORTIC ROOT GEOMETRY FROM (A) THE MSCT SCAN OF THE AORTIC ROOT, (B) SEGMENTATION OF THE AORTIC ROOT USING MIMICS 14.1 TO THRESHOLD THE MSCT SCANS AND (C) THE FINAL AORTIC ROOT MESH INCLUDING NATIVE LEAFLETS AND CALCIFICATIONS.....	85
FIGURE 3.3: THE LOTUS™ VALVE STENT GEOMETRY IN (A) UNLOCKED AND (B) LOCKED CONFIGURATION.	86
FIGURE 3.4: EXPERIMENTAL DATA VERSUS MODEL PREDICTIONS FOR THE STRESS-STRAIN RESPONSE OF THE HUMAN AORTIC SINUS AND ASCENDING AORTA.	87
FIGURE 3.5: CRIMPING AND DEPLOYMENT METHOD FOR THE VALVE STENT. (A) THE STENT IN ITS RELAXED POSITION. (B) THE CRIMPING OF THE STENT USING A CYLINDRICAL CRIMP THAT IS REDUCED INWARD RADIALLY AND USING CONTACT CRIMPS THE STENT TO A DIAMETER OF 18FR. (C) THE STENT IN ITS CRIMPED CONFIGURATION POSITIONED INSIDE THE AORTIC ROOT. (D) THE CRIMP IS EXPANDED ALLOWING THE SELF-EXPANSION OF THE NITINOL	

STENT AND DEPLOYMENT INTO THE AORTIC ROOT. (E) THE CONNECTOR ELEMENTS ARE DISPLACED INWARD TO LOCK THE STENT TO A HEIGHT OF 19 MM.	91
FIGURE 3.6: LOCKED LOTUS™ VALVE POST-DEPLOYMENT IN THE CALCIFIED AORTIC ROOT GEOMETRY.....	91
FIGURE 3.7: SECTION VIEWS OF THE STENT ECCENTRICITY THROUGHOUT THE STENT AT THE INFLOW, MID-PLANE AND OUTFLOW PORTIONS OF THE STENT FOR THE DIFFERENT DEPLOYMENT CONDITIONS WHERE E DENOTES STENT ECCENTRICITY.....	92
FIGURE 3.8: CONTOUR PLOTS OF THE PEAK VON MISES STRESS AND CORRESPONDING CALCIFICATION. IN THE 5 MM SUB-ANNULAR POSITION, A PEAK STRESS OF 0.892 MPA WAS CAUSED BY COMPRESSION OF THE CALCIUM DEPOSIT (INDICATED BY *) LOCATED ON THE NON-CORONARY. WHEN THE VALVE IS IMPLANTED IN THE ANNULAR POSITION, A HIGHER PEAK STRESS WAS PREDICTED (1.035 MPA) DUE TO ANOTHER PIECE OF CALCIUM ON THE RIGHT-CORONARY CUSP (INDICATED BY †). HOWEVER, WHEN THE VALVE WAS IMPLANTED AT THE 5 MM SUPRA-ANNULAR POSITION, THE STENT APPLIED A GREATER FORCE TO THE SAME CALCIUM DEPOSIT (†) LEADING TO THE HIGHEST PEAK STRESS (1.141 MPA) AT THE 5 MM ANNULAR POSITION.....	94
FIGURE 3.9: (A) THE AREA IN RED DEFINED AS THE INTERLEAFLET TRIANGLE BETWEEN THE NON- CORONARY (NC) AND RIGHT- CORONARY (RC) SINUS (B) CONTOUR PLOTS OF VON MISES STRESS DISTRIBUTION THROUGHOUT THE AORTIC SINUS AND THE INTERLEAFLET TRIANGLE BETWEEN THE NON-CORONARY (NC) AND RIGHT- CORONARY (RC) SINUS FOLLOWING DEPLOYMENT OF THE LOTUS™ VALVE STENT AT THE DIFFERENT IMPLANTATION POSITIONS.....	95
FIGURE 3.10: PERCENTAGE VOLUME GRAPH FOR THE THREE DIFFERENT POSITIONS SHOWING THE STRESS DISTRIBUTION THROUGHOUT THE INTERLEAFLET TRIANGLE BETWEEN THE NON-CORONARY AND RIGHT- CORONARY SINUS FOLLOWING DEPLOYMENT OF THE LOTUS VALVE STENT.....	96
FIGURE 4.1: (A) BRAIDING OF THE STENT ON A MANDREL (B) FINISHED STENT GEOMETRY.....	106
FIGURE 4.2: RADIAL FORCE TEST SET UP.	107
FIGURE 4.3: (A) UNCALCIFIED AND (B) CALCIFIED PORCINE AORTIC VALVE.....	109

FIGURE 4.4: CREATION OF THE STENT GEOMETRY FROM (A) THE MSCT SCAN OF THE STENT, (B) DEPICTS SEGMENTATION OF THE STENT USING MIMICS 14.1 TO THRESHOLD THE MSCT SCANS, AND (C) RECONSTRUCTION OF THE STENT POST-DEPLOYMENT IN THE CALCIFIED PORCINE AORTIC ROOT, MEASUREMENTS WERE TAKING OF THE MAXIMUM AND MINIMUM DIAMETERS AT THE TOP, MIDDLE AND BOTTOM OF THE STENT..... 110

FIGURE 4.5: PORCINE HEART WITH APEX DISSECTED AND PINNED IN PLACE PRIOR TO THE PULLOUT TEST. 111

FIGURE 4.6: RADIAL OUTWARD FORCE (N) VERSUS DIAMETER (MM) FOR THE STENT. 113

FIGURE 5.1: EXPERIMENTAL DATA VERSUS 100% INCREASE IN STIFFNESS FOR THE STRESS-STRAIN RESPONSE OF THE HUMAN AORTIC SINUS AND ASCENDING AORTA. 126

FIGURE 5.2: SCHEMATIC DEPICTING THE STENT (A) IN A RELAXED CONFIGURATION (B) PRIOR TO CRIMPING (C) IN A CRIMP CONFIGURATION IN THE AORTIC ROOT (D) UNSHEATHING INTO THE AORTIC ROOT AND (E) IN A LOCKED CONFIGURATION. 127

FIGURE 5.3: SCHEMATIC OF THE STENT AT DIFFERENT ORIENTATIONS (0°, 40°, 80°), AND THEIR INITIAL DEPLOYMENT POSITIONS IN THE LBBB AND NON-LBBB PATIENTS. THE VALVE POSTS ARE HIGHLIGHTED IN BLACK AND THE INTERLEAFLET TRIANGLE IN CLOSE PROXIMITY TO THE HEART'S CONDUCTANCE SYSTEM IS HIGHLIGHTED IN RED. 128

FIGURE 5.4: COMPARISON OF THE MODEL STENT GEOMETRY WITH THAT OF POST-DEPLOYMENT ANGIOGRAM FROM THE CLINICAL CASE. D1, D2, AND D3 ARE THE DIAMETERS AT PLANE 1, 2 AND 3 RESPECTIVELY. 130

FIGURE 5.5: CONTOUR PLOTS OF THE VON MISES STRESS (MPA) IN THE INTERLEAFLET TRIANGLE IN THE NON-LBBB PATIENTS AT DIFFERENT STENT ROTATIONS. 134

FIGURE 5.6: CONTOUR PLOTS OF THE VON MISES STRESS (MPA) IN THE INTERLEAFLET TRIANGLE IN THE LBBB PATIENTS AT DIFFERENT STENT ROTATIONS. 134

FIGURE 6.1: SCHEMATIC OF THE ANATOMICAL CLASSIFICATION OF BAVS WHERE THE PROMINENT BLACK LINE REPRESENTS THE FUSION OF THE LEAFLETS L, LEFT CORONARY SINUS; LAT, LATERAL; N, NONCORONARY SINUS; AND R, RIGHT CORONARY SINUS [213]. 139

FIGURE 6.2: COMPARISON OF MODEL STENT GEOMETRY WITH THAT OF POST-DEPLOYMENT ANGIOGRAM FROM THE REAL-LIFE CASE. D1, D2, AND D3 ARE THE DIAMETERS AT PLANE 1, 2 AND 3 RESPECTIVELY.	144
FIGURE 6.3: CONTOUR PLOTS VON MISES STRESS IN THE AORTIC SINUS (MPA) POST OF DEPLOYMENT THE 25 MM AND 27 MM VALVE.....	147
FIGURE 6.4: SCHEMATIC OF THE VALVE STENT AND AORTIC ROOT WITH POTENTIAL FOR PARAVALVULAR LEAKAGE.	148
FIGURE 7.1: GRAPHICAL REPRESENTATION OF THE WORK CONDUCTED AS PART OF THIS PHD THESIS IN THE CONTEXT OF PREVIOUS STUDIES.	160
FIGURE A.1: ILLUSTRATION OF FINITE ELEMENT DEFORMATION MECHANICS.....	191

Table of Tables

TABLE 2.1: AHA GUIDELINES FOR SEVERITY OF AORTIC STENOSIS [89].	46
TABLE 3.1: MATERIAL PARAMETERS OF HUMAN AORTIC SINUS AND ASCENDING AORTA.	87
TABLE 3.2: PEAK VON MISES STRESS AT DIFFERENT POSITIONS FOR THE LOTUS™ VALVE STENT.	93
TABLE 5.1: COMPARISON OF MODEL STENT DIMENSIONS WITH THAT OF POST-DEPLOYMENT ANGIOGRAM FROM THE REAL-LIFE CASE.	130
TABLE 5.2: A COMPARISON OF VON MISES STRESS (VMS) AND CONTACT PRESSURE, IN MPA, IN THE INTERLEAFLET TRIANGLE AT FINAL DEPLOYMENT.	131
TABLE 5.3: A COMPARISON OF MAXIMUM VON MISES STRESS AND CONTACT PRESSURE IN THE INTERLEAFLET TRIANGLE WHERE THE BUNDLE OF HIS RESIDES FOR THE PATIENT WITH NO NEW-ONSET LBBB FOR DIFFERENT ROTATIONS OF THE STENT (0°, 40°, 80°).	132
TABLE 5.4: A COMPARISON OF MAXIMUM VON MISES STRESS AND CONTACT PRESSURE IN THE INTERLEAFLET TRIANGLE WHERE THE BUNDLE OF HIS RESIDES FOR THE PATIENT WITH NEW-ONSET LBBB FOR DIFFERENT ROTATIONS OF THE STENT (0°, 40°, 80°).	133
TABLE 6.1: SIZING CHART FOR TRANSCATHETER VALVES [57].	142
TABLE 6.2: COMPARISON OF MODEL STENT DIMENSIONS WITH THAT OF POST-DEPLOYMENT ANGIOGRAM FROM THE REAL-LIFE CASE.	145
TABLE 6.3: TABLE OF RESULTS COMPARING ECCENTRICITY AND VON MISES STRESS BETWEEN THE FOUR CASES.	147
TABLE A.1: PARAMETERS IMPLEMENTED IN NITINOL VUMAT.	204

Chapter 1: Introduction

Aortic stenosis (AS) is a degenerative disease of the aortic heart valve that occurs due to the formation of calcium deposits on the leaflets of the aortic valve, which leads to a narrowing of the valve and restriction in the movement of the leaflets, causing a severe obstruction of blood flow [1]. Valvular diseases account for 10-20% of all cardiac surgical procedures in the United States [2] and AS is the third most prevalent cardiovascular disease in the Western world. If left untreated, AS can lead to complications such as cardiac ischemia, elevated left ventricle filling pressure and decreased cardiac output, as well as angina, syncope and heart failure, which are all associated with high mortality rates [3]. The average lifetime for a patient with AS, who does not receive any intervention, is within 2-3 years of the onset of symptoms [4-6]. Currently, there is no effective medical therapy to prevent or delay calcification of the aortic valve leaflets [7], and the gold standard treatment for severe AS is Surgical Aortic Valve Replacement (SAVR) [8], which can improve patient lifespan and offer relief of symptoms. In the absence of comorbidities, the procedure is associated with low mortality rates [9].

Surgical valves can be either Mechanical Heart Valves (MHVs) or Bioprosthetic Heart Valves (BHV) [10]. MHVs are synthetic prostheses designed to mimic the function of the heart valve in preventing backflow. These prosthetic valves have great durability but are associated with hemodynamic complications and patients require lifelong antithrombotic therapy [10, 11]. BHVs incorporate animal tissue, with/without a metallic supporting frame, to mimic the human valve and as a result are less thrombogenic, thereby mitigating the need for anticoagulation treatments [10, 12]. However, BHVs are not as durable as mechanical valves with lifespans limited to 10 years [10, 13]. Moreover, while surgical heart valves are effective in the treatment of AS, the procedure is highly invasive and poses a significant risk for elderly

patients with comorbidities. For this reason, approximately 33% of patients requiring this treatment are too high risk undergo this surgery [14].

Transcatheter Aortic Heart Valves (TAVs) are a minimally invasive alternative to surgical heart valves for the treatment of AS, which were initially conceived for the treatment of high-risk patients who were refused surgical valve replacement. TAVs consist of tissue leaflets mounted onto a collapsible valve stent, which is crimped and delivered to the site of the disease using a catheter and expanded by means of a medical balloon or a self-expanding nitinol frame. The first Transcatheter Aortic Heart Valve Implantation (TAVI) procedure was performed by Dr. Alan Cribier in 2002 [15]. The first-generation commercial TAVs, the Edwards SAPIEN® Valve and Medtronic Corevalve®, received CE approval in 2007 and were approved by the FDA in November 2011 and January 2014 respectively [16, 17]. Over 90,000 TAVI procedures were successfully performed worldwide in the decade following the first TAVI procedure in 2002 [7, 18]. However, there are a number of associated complications with the TAVI procedure, such as paravalvular leakage (PVL), stent and leaflet distortion, conductance interference, stroke, device migration, coronary occlusion, and aortic root rupture [19-25]. These complications have been associated with specific patient anatomies or comorbidities, device design or procedural complications, such as malpositioning or incorrect sizing of the valve leading to excessive or inadequate radial force acting on the native aortic root.

In recent years, in an effort to mitigate such complications, next-generation valves have been developed with reduced profile delivery systems, improved device durability and the ability for valve repositioning. Such technologies include the Direct flow valve (Direct Flow Medical, Santa Rosa, CA), the Evolut R (Medtronic, Minneapolis, MN) and the Lotus™ Valve (Boston Scientific SADRA, Los Gatos, CA) [9, 26-28]. Further to this, there are presently many other TAV technologies under development [9]. However, there is still a lack of understanding

regarding the optimal positioning of TAVs, the amount of radial force required to secure the valve in the aortic root and the appropriate sizing of TAV devices for particular patient cases. This PhD thesis seeks to derive an enhanced understanding of these parameters, specifically focusing on the LotusTM Valve, which is a next-generation repositionable TAV that combines the self-expanding properties of nitinol with a mechanical locking mechanism that allows for repositioning of the valve.

Positioning of Transcatheter Aortic Heart Valves

Computational studies have investigated the impact of TAV positioning on the biomechanical interaction between the TAV stent and the aortic root, specifically investigating the Edwards SAPIEN, CoreValve and a generic self-expanding valve. It was reported that valve positioning can affect peak von Mises stress in the stent and aortic root, stent-root contact area and stent distortion, which can lead to increased leaflet stress [29-31]. However, the impact of the positioning of the Lotus valve has not yet been investigated.

In recent years it has been proposed that injury following TAVI can result in interference with the heart's conduction system leading to the requirement for in-hospital temporary pacing and if unresolved, Permanent Pacemaker Implantation (PPM) [32, 33]. The bundle of His is an extension of the atrioventricular (AV) node and consists of a branch of specialised cells that facilitate electrical conduction [34]. The bundle of His is positioned at the base of the interleaflet triangle between the non-coronary and the right coronary aortic sinus in close proximity with the aortic root [32, 33, 35]. It has been proposed that injury in this area is an underlying cause of conductance interference [32, 33]. Clinical studies have found that supra-annular positioning of TAVs reduces the incidence of conductance interference [36-38], which may be due to reduced stresses in the interleaflet triangle between the non-coronary and the right coronary aortic sinus. Patient-specific computational modelling has been used to

investigate many TAV complications, such as aortic root rupture [39], PVL and coronary occlusion [40, 41], asymmetric expansion and leaflet stresses [29, 42] and poor hemodynamic performance [43]. Finite Element (FE) methods can provide an insight into the biomechanical consequences of TAVI deployment, which cannot be assessed *in vivo*. However, the relationship between stresses in the interleaflet triangle and TAV positioning has never been investigated quantitatively using a computational approach. Therefore, the first research hypothesis of this thesis is “*Supra-annular positioning reduces stress in the interleaflet triangle in which the conductance system (Bundle of His) resides*”.

Procedural Complications (Migration versus Injury)

Aortic injury, leading to conductance interference and more severe complications such as aortic root rupture, have been associated with excessive radial force during TAV implantation [39, 44]. However, inadequate radial force can lead to dislodgement and migration of the stent into the left ventricle [45]. Nevertheless, the amount of radial force required to keep the valve in place without damaging the native tissue is not yet fully understood.

Unlike surgical valves, TAVs are not sutured into place and the native stenotic valve is not removed. For this reason, the native valve and surrounding aortic anatomy play an important role in providing the radial force to secure the valve in place. Thus for TAVs, there is a heavy reliance on the tissue-stent interaction for valve performance [9]. The tissue-stent interaction has been quantified experimentally *in vitro* using ovine and porcine aortic roots and the coefficient of friction between the TAV and aortic root was found to be 0.10 ± 0.01 [46]. It has previously been proposed that calcification helps secure the valve in place [40]. However, the TAV-tissue interaction has never been quantified for a stenosed aortic root where calcification is present. Therefore, the second hypothesis of this thesis is “*Calcification secures*

the TAV in place by increasing the friction in the interaction between the TAV stent and a stenosed aortic root”.

As previously mentioned, excessive radial force is associated with aortic root rupture and conductance interference. Aortic root rupture is an uncommon complication occurring in 1% of TAVI cases [127, 128], which has previously been examined computationally [39]. However, incidences of new-onset conductance interference arise in 8-30% of balloon expandable valve implantations (438 patients in 5 studies) [47] and for 25-85% of cases (738 patients in 11 studies) for the self-expanding Medtronic CoreValve [47]. The most common post-TAV conductance interference is Left Bundle Branch Block (LBBB) [48], which is an independent indicator of mortality [49]. LBBB has been associated with injury and inflammation in the vicinity of the bundle of His [32, 33, 50]. This may be caused by higher levels of tissue stress during TAVI deployment. However, there is limited knowledge on the extent of tissue stress associated with conductance interference.

Patient-specific modelling approaches allow for the reconstruction of the specific patient anatomies to investigate, computationally, the levels of tissue stress *in-vivo*. A study by Rocatello *et al.* used a patient-specific modelling approach to investigate the levels of contact pressure on the membranous septum associated with conductance abnormalities [44]. This study simulated deployment of the CoreValve/Evolut R retrospectively into patients with and without new on-set conductance disorders. It was found that a maximum contact pressure greater than 0.39 MPa and contact pressure index greater than 14% are predictors of conductance abnormalities [44]. The impact of rotating the stent 6° and 12° was also investigated with no significant difference in contact pressure and contact pressure index reported. However, the Lotus valve was not investigated in this study. The unique locking mechanism of the Lotus valve has shown higher incidences of new on-set LBBB (55.2% [51]) when compared to other TAV devices (Edwards SAPIEN (13%) and CoreValve (38.8-50%))

[51]). Furthermore, the locking mechanism of the valve incorporates buckles and posts, which have potential to impact tissue stress in the aortic root as the valve is rotated. For these reasons further investigation of the relationship between the Lotus valve, the stresses leading to conductance interference and the impact of valve orientation are necessary. Therefore, the third hypothesis of this thesis is *“Orientation of the Lotus valve impacts the stress in the vicinity of the bundle of His and can induce conductance interference”*.

TAVI Sizing in the Treatment of Bicuspid Patients

Bicuspid Aortic Valves (BAVs) are a common congenital cardiac malformation of the aortic valve, where two cusps of the valve have become fused together due to a rheumatic or inflammatory process [52, 53]. While TAVI is often used in the off-label treatment of BAV stenosis, the efficacy of the TAV for treatment of the bileaflet geometry is still an area of controversy and further research is required [54, 55]. Unfortunately, many TAVI trials have contraindicated the treatment of bicuspid patients and they are generally excluded from TAVI trials [56]. For all TAVs on the market, each valve size is designed to cover a range of patient sizes based primarily on the diameter of their aortic annulus alongside their annulus perimeter and the height of the sinus of Valsalva. Each valve offers different degrees of oversizing dependent on the valve type [57]. Recently, it has been proposed that the application of traditional annulus measurement and device sizing, used for tricuspid aortic valves, are not appropriate in treating BAV stenosis [58]. A study investigating the Lotus valve in BAV patients reported good fixation, circularity and good hemodynamics, without significant paravalvular regurgitation [59]. However, the authors noted that results of using a different valve size, which may have improved patient outcomes, are unknown [59]. Therefore, the final hypothesis of this PhD thesis is *“Bicuspid patients with stenosed aortic valves can be effectively treated using the LotusTM Valves in terms of stent eccentricity and tissue stress using traditional device sizing”*.

1.1 Thesis Objectives and Hypothesis

The global objective of this thesis is to investigate the biomechanical interaction between a braided TAV stent and a stenotic calcified aortic root. In particular, the PhD thesis will (1) investigate the level of radial force that is required to keep the stent securely in position, whilst minimising damage to the surrounding native tissue and structures, and (2) investigate the relationship between stress in the aortic root and conductance interference with the aim of further informing specific patient sizing criteria. The first specific objective of this thesis is to use a computational approach to determine the impact of positioning on the tissue-stent interaction and the ensuing stress in the region of the aortic root in close proximity to the heart's conductance system. The second objective is to develop a calcified *in vitro* model, using artificially calcified porcine aortic roots, to investigate the effect of leaflet calcification on the tissue-stent interaction and its role in securing the stent in the aortic root. The third objective is to use a patient-specific computational framework combined with clinical outcomes to compare the stresses arising in patients with and without conductance interference. Additionally, this computational framework will be used to investigate the relationship between Lotus valve orientation and stresses leading to conductance abnormalities. The fourth and final objective is to determine the efficacy of using TAVI in the treatment of BAV stenosis and to assess if current sizing guidelines are appropriate for the abnormal patient geometry. Four hypotheses have been defined to address each of the objectives outlined above, each of which will underpin the research of Chapters 3-6 of this thesis.

Hypothesis 1: *Supra-annular positioning reduces stress in the interleaflet triangle in which the conductance system (Bundle of His) resides*

Hypothesis 2: *Calcification secures the TAV in place by increasing the friction in the interaction between the TAV stent and a stenosed aortic root*

Hypothesis 3: *Orientation of the Lotus valve impacts the stress in the vicinity of the bundle of His and can induce conductance interference*

Hypothesis 4: *Bicuspid patients with stenosed aortic valves can be effectively treated using the LotusTM Valves in terms of stent eccentricity and tissue stress using traditional device sizing*

1.2 Thesis Structure and Overview

This thesis comprises the work completed for the duration of the candidate's Ph.D. studies. In Chapter 2, a thorough review of the relevant literature is presented, detailing the anatomy and function of the heart and heart valves, the mechanics of the aortic valve, aortic valve disease, aortic valve replacement, fluid and leaflet mechanics of aortic valve replacements and computational and experimental approaches that have been developed to analyse the biomechanics of the TAVs. In Chapter 3 a patient-specific computational framework, which simulates deployment of the LotusTM valve into a realistic aortic root model derived from Multi-Slice Computed Tomography (MSCT) imaging, is developed. This framework is applied to investigate the impact of implantation depth of the LotusTM valve on mechanical stress in the interleaflet triangle in which the bundle of His resides, thereby testing hypothesis 1 of this thesis. In Chapter 4 an *in vitro* model of AS is created and used to investigate the role of calcification in the tissue-stent interaction in a calcified aortic root, thereby testing hypothesis 2 of this thesis. In Chapter 5, patient-specific computational models, derived from MSCT imaging of patients with and without new onset LBBB (post-deployment of the LotusTM valve), are applied to investigate the stresses experienced by the aortic root when LBBB occurs. This knowledge will be used to investigate the relationship of Lotus valve orientation and conductance abnormalities, thereby addressing hypothesis 3. In Chapter 6, deployment of a Lotus valve into a patient-specific model of a BAV patients is simulated and used to investigate sizing algorithms in BAV patients, thereby testing hypothesis 4 of this thesis. A summary of

the main findings of the thesis is contained in Chapter 7, placing them in the context of current research, along with recommendations for future research in the TAVI field.

Chapter 2: Literature Review

2.1 The Heart and Heart Valves

The human heart consists of four chambers; the left and right atria and the left and right ventricle. Deoxygenated blood flows into the heart entering the right atrium via the superior and inferior vena cavae. Ventricular relaxation then allows blood to flow through the tricuspid valve into the right ventricle. Ventricular contraction causes blood to be pumped through the pulmonary arteries to the lungs where the blood becomes oxygenated [60, 61]. Oxygenated blood returns to the heart via the pulmonary vein where it enters the left atrium. During ventricular relaxation, the mitral valve opens allowing blood to fill the left ventricle. As the ventricles contract blood is pumped from the left ventricle through the aortic valve and into the systemic circulation via the aorta [60, 61].

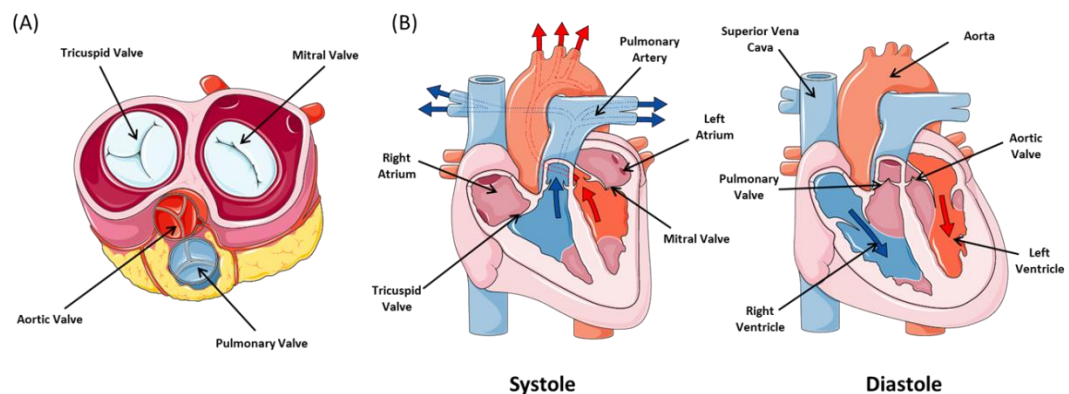


Figure 2.1: (a) The valves of the heart in (b) Systole and Diastole (adapted from <https://smart.servier.com>).

The four heart valves in the heart are responsible for unidirectional blood flow throughout the heart. On the oxygenated left side of the heart, the mitral and the aortic heart valves control flow, whereas the pulmonary and tricuspid valves

control blood flow on the deoxygenated right side [60, 61]. The tricuspid and mitral valves are known as atrioventricular valves and they control blood flow from the atria to the ventricles [62]. The pulmonary and aortic valves are known as the arterioventricular valves, as they are situated between a ventricle and an artery, or semilunar valves, due to their half-moon shaped leaflets [62]. The atrioventricular valves are attached to the myocardium by means of papillary muscle and fibrous cords and thereby actively respond to myocardial contractions. The semilunar valves do not have a connection between the mobile part of the leaflet and the myocardium [62]. The opening and closing of the heart valves are controlled by the pressure gradients created during the contraction and relaxation of the myocardial tissue [60, 61].

2.1.1 Aortic Root and Valve Anatomy

The aortic root is a direct continuation of the Left Ventricular Outflow Tract (LVOT) and refers to the aortic valve from its position at the outlet of the left ventricle to where it connects to the ascending aorta [35, 63]. The aortic valve is composed of the sinus of Valsalva, the Sinotubular Junction (STJ), the fibrous interleaflet triangles, the leaflet attachments and the valvular leaflets [32, 35, 63]. Normal aortic valves consist of three leaflets [35]. However, in some patient cases a common congenital cardiac malformation of the aortic valve occurs where two cusps of the valve have become fused together, this is known as a Bicuspid Aortic Valve (BAV) and is comprised of two, often unequally sized, leaflets instead of the normal tri-leaflet aortic valve. Anatomically these leaflets can be divided into three different regions: the free margin (the coaptation area), the “belly” of the leaflet and the basal part of the leaflet [32]. The free margin has a thickened circular node

known as the nodule of Arantius that provides a coaptation area for the corresponding leaflets, the basal part is where the leaflets are attached to the aortic wall by a thick fibrous crown shaped ring [32, 35]. The three apexes of the crown like annulus where the leaflets are attached to the aortic wall are known as commissures [33]. The STJ runs through the upper part of each commissure marking the upper end of attachment of each leaflet and the point of transition into the ascending aorta [33]. Under these commissures lie the interleaflet triangles, these triangles consist of thinned aortic wall [33]. Hemodynamically the interleaflet triangles are extensions of the LVOT and extend as far as the STJ in the area of the commissures. The triangle between the left- and non-coronary sinuses is inferiorly connected with the anterior leaflet of the mitral valve. The triangle between the right- and non-coronary sinuses is connected with the membranous septum proximally and faces the right atrium (Figure 2.1) [32, 33].

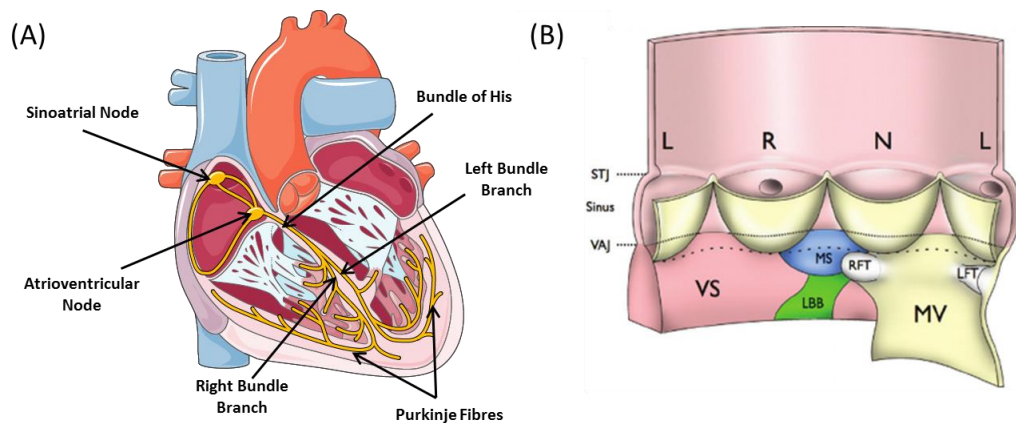


Figure 2.2: (A) The heart's conduction system, (B) the aortic valve complex, where the valvular leaflets are attached along the ventriculoarterial junction (VAJ), L is the left coronary sinus, R is the right coronary sinus, N is the non-coronary sinus, VS is the ventricular septum, MV is the mitral valve, MS is the membrane septum and LBB the left bundle branch, LFT and RFT are the right and left fibrous trigones (adopted from; <https://smart.servier.com>, [64]).

In this triangle, the conduction system comes into close proximity to the aortic root [33]. The AV node is located at the apex of the triangle of Koch in the wall of the right atrium and is relatively distant from the root [35]. The bundle of His is positioned at the base of the interleaflet triangle between the non-coronary and the right coronary aortic sinus [32, 33, 35]. The bundle penetrates through the central fibrous body providing atrioventricular protection, at the edge of the muscular ventricular septum. The left bundle branch then spreads out on the smooth left ventricular side (Figure 2.1) [33, 35]. Injury in these areas is of great concern during valve procedures as it has been proposed that this injury can result in temporary or permanent conduction abnormalities, which require in-hospital

temporary pacing and if unresolved, Permanent Pacemaker Implantation (PPM) [32, 33].

The aortic side of the annulus is comprised of three bulges of the aortic wall, known as the sinuses. The sinuses are proximally confined by the attachments of the valve leaflets and distally confined by the STJ [33]. Two of the sinuses contain the coronary arteries and the sinuses are termed according to the coronary ostia: right-, left-, and non-coronary sinus [33]. The height of each leaflet is considerably less than that of its sinus to prevent the leaflet from exceeding the height of the STJ and occluding the coronary ostias [35]. The sinuses are primarily made of aortic wall tissue, however, it is thinner than the native aorta [33]. The exact function of the Valsalva sinuses is unknown however evidence suggests that the vortices created in the aortic sinuses aid in valve closure, reduce stress on the aortic leaflets and support flow to the coronaries [32, 62, 65, 66].

2.1.2 Aortic Valve Tissue

The leaflets of the aortic valve are made up of heterogeneous tissue. This tissue consists of three main layers each containing varying amounts of connective tissue (proteins, collagen and elastin), glycosaminoglycans and valve interstitial cells, differing in density and composition; the fibrosa, the spongiosa and the ventricularis [62, 67]. The fibrosa is the most apparent layer [62], it is twice as thick as the ventricularis and twice as stiff [68]. The fibrosa predominantly consists of type I collagen fibres, whose alignment is dependent on the loading conditions experienced by the leaflet. These collagen fibres are crimped and when the tissue is stretched they straighten allowing the leaflet to extend until the point where the collagen fibre crimp disappears [68]. The two main layers, the fibrosa and

ventricularis are separated by the central spongiosa, which is a loose watery connective tissue that is highly concentrated with glycosaminoglycans and fibrous structures and acts as a lubricant during the cardiac cycle leading to shear and deformation of these two layers [1, 62, 67, 69]. The ventricularis, located at the inflow side of the valve [69], consists of both collagen fibres and elastin. The collagen fibres limit the extensibility of the ventricularis. However, the mechanical coupling with the radially aligned sheets of elastin and the manner in which the collagen fibres are highly folded in a contracted state allow for large radial extensibility [68, 69]. The function of the ventricularis appears to be to reduce large radial strains when the valve is fully opened. When the leaflet is relaxed the ventricularis is under slight tension due to its high elastin content, whereas the fibrosa is under slight compression due to the compressive forces exerted by the ventricularis keeping the fibrosa in the undulated collagen conformation [67, 68].

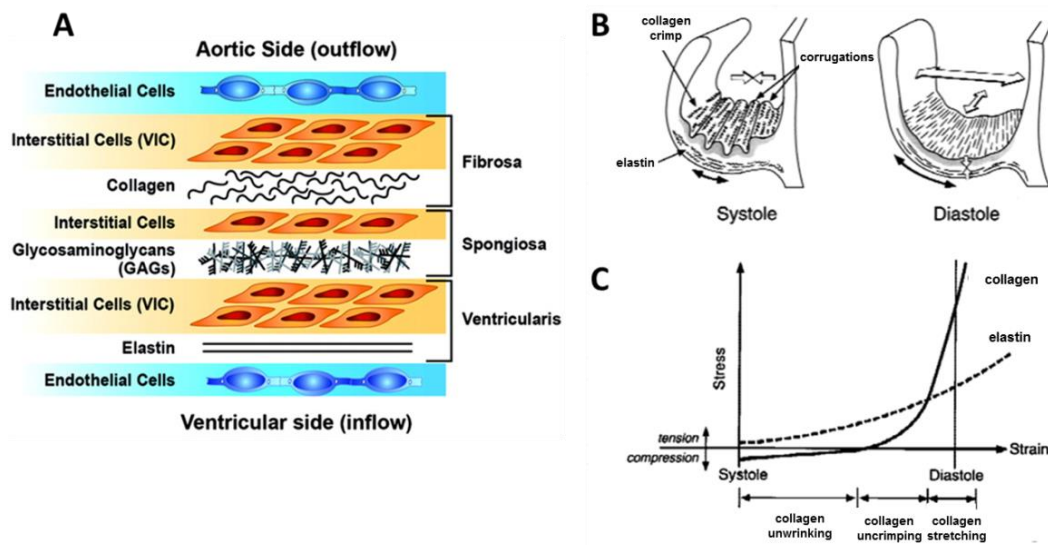


Figure 2.3: Schematic of (A) the cellular architecture of a normal aortic valve, (B) the architecture of collagen and elastin in systole and diastole, (C) the biomechanical response of collagen and elastin during valve motion (Image adapted from [70, 71]).

2.2 Biomechanics of the Aortic Valve

The aortic valve opens and closes approximately 103,000 times a day, and in a patient's lifetime the valve opens and closes 3.7 billion times [62]. The opening and closing of aortic heart valves are dependent on a complex combination of the blood flow and pressure gradients across the valve, the fluid mechanics and the structural deformation of the commissures and of the leaflets themselves [62]. The cardiac cycle can be divided into various parts in which valve mechanics can be examined; early systole (100-250 ms), peak systole (250 ms), late systole (250-400 ms) and diastole (400-860, 0-100 ms) [72].

2.2.1 Fluid Mechanics and Hemodynamics

Heart valves are essentially controlled by their hemodynamic environment and hemodynamics is critical to normal function and disease progression [73]. At early systole blood rapidly accelerates as the aortic valve opens [74], a jet originates from the valve orifice immediately forming a 3D vortex ring as the jet is ejected into the quiescent fluid in the aorta [72]. A central systolic jet is observed during the acceleration phase as the vortices behind the valve leaflets migrate to the tip of the leaflets at peak systole [75]. At peak systole, the flow reaches its highest velocity [72]. The vortex ring then migrates to the sinus where it increases the leaflet opening angle [76]. When the leaflets are fully open they are almost at 90° to their closed position. Towards the end of systole and the beginning of diastole ventricular relaxation occurs and leads to a decrease in pressure due to the deceleration of ejecting blood [61]. During deceleration, the Transvalvular Pressure Gradient (TVG) contributes to valve closure [75]. At late systole, the velocity fields are similar to those seen at peak systole with lower magnitudes [72]. The valve closes near the end of the deceleration phase of systole allowing little reverse flow through the valve [61]. As the leaflets of the aortic valve begin to close the column of fluid moves back into the aortic sinus creating vortices in the sinuses [75]. These vortices lead to a transverse pressure difference, which pushes the leaflets towards the centre of the aorta leading to rapid and synchronized closure of the valve leaflets and minimising the closing volume [61, 75]. During diastole, the valve is closed and the velocity of fluid flow is zero due to the gradual dissipation of momentum that occurred during late systole [72].

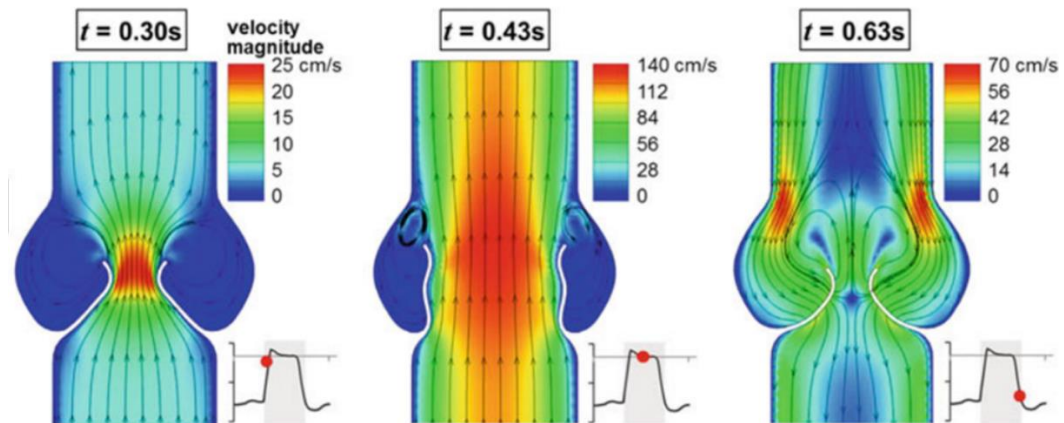


Figure 2.4: Flow velocity and streamlines through the aortic valve during, the acceleration phase ($t=0.30\text{ s}$), at peak systole ($t=0.43\text{ s}$) and during the deceleration phase ($t=0.63\text{ s}$) [75].

2.2.2 Solid Mechanics

The biomechanical function of heart valves is multi-modal [73]. The loading of heart valves is repeated with every cardiac cycle over an entire lifetime, meaning valves will repeat their cycle at least 3×10^9 times [73]. In Figure 2.5, at point (a), the beginning of systole, the TVG reduces due to the increase of the ventricular pressure, the leaflets of the valve relax and begin to open allowing for flow through the valve [77]. At (b) approximately 20 - 30 ms after systole begins a reverse in the TVG allows for rapid opening of the valve. Blood rapidly accelerates until peak flow is achieved, the valve becomes fully opened and the leaflets exhibit a “minor fluttering” until the closing phase begins [74, 77]. Ventricular pressure then decreases at late systole (at point (c)) leading to an adverse TVG causing a reverse flow and vortices formation in the sinus region leading to valve coaptation [74, 77]. At (d) the valve fully closes near the end of systole. After the valve has coapted it continues to stretch under the pressure gradient [74, 77]. At (e) TVG is at a

maximum and the valve is under maximum stretch, with slight changes in the gradient leading to minor axial displacements in the closed leaflets [77]. At (f) the TVG plateaus at the end of diastole before the pressure gradient is reversed and systole begins again.

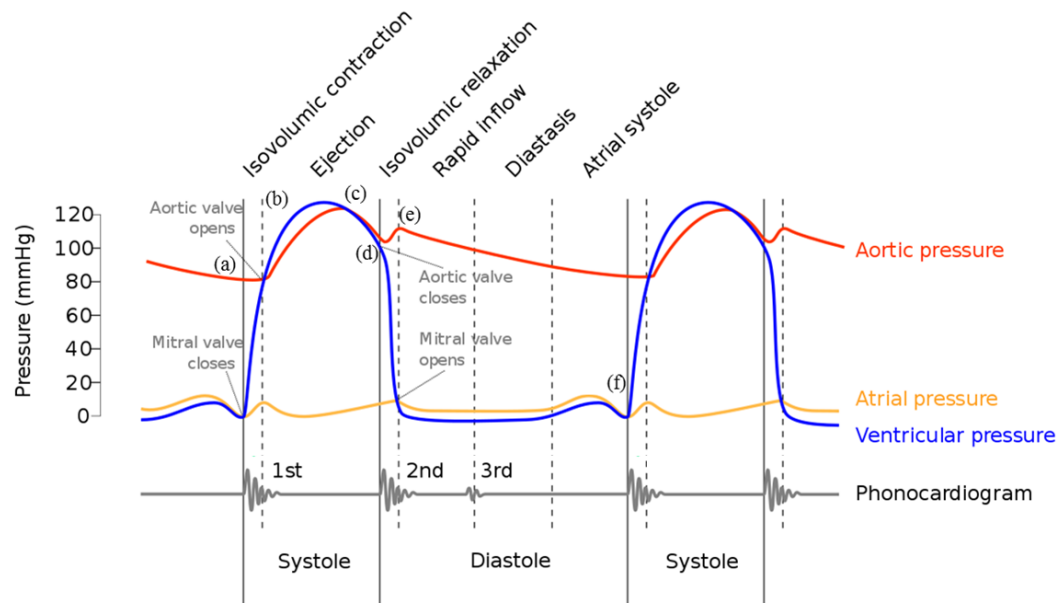


Figure 2.5: Wiggers diagram illustrating aortic pressure, atrial pressure, and ventricular pressure versus time (adapted from www.wikiwand.com).

The leaflets of the aortic valve experience three main types of loading conditions; tension, shear and flexure [62, 69]. During the diastolic phase, the leaflets undergo both radial and circumferential stretch. This increase in stretch allows for an adequate adaptive seal to prevent backflow through the valve [77-79]. A study examined the dynamic deformation of the aortic valve using porcine aortic valves that were marked with a grid of ink dots. Dual-camera stereophotogrammetry was used to determine the stretch magnitudes of the leaflets throughout the cardiac cycle, which was simulated using a physiological left heart

simulator [80]. It was found that during early and late diastole the stretch throughout the leaflets is homogenous, at peak diastole the circumferential, aerial and radial stretch decreases from base to coaptation area (with circumferential stretch significantly different at the base than the belly and coaptation area). Mid-diastole shows similar stretch patterns but at lower magnitudes [80]. During systole, the forward flow leads to stretch in the radial direction but compression in the circumferential direction [77]. The change in the curvature of the leaflets also leads to bending, shearing and buckling throughout the cardiac cycle [78]. Bending of the leaflets is compressive on the concave side of the leaflet while it is tensile on the convex side. The belly of the leaflet undergoes reversal of curvature during loading and unloading of the valve [78]. Furthermore, shear stress is exerted by blood flow on the leaflets of the valve on the ventricularis side when the blood flows past the valve in systole and then on the aortic surface when the blood gathers in the sinuses [78].

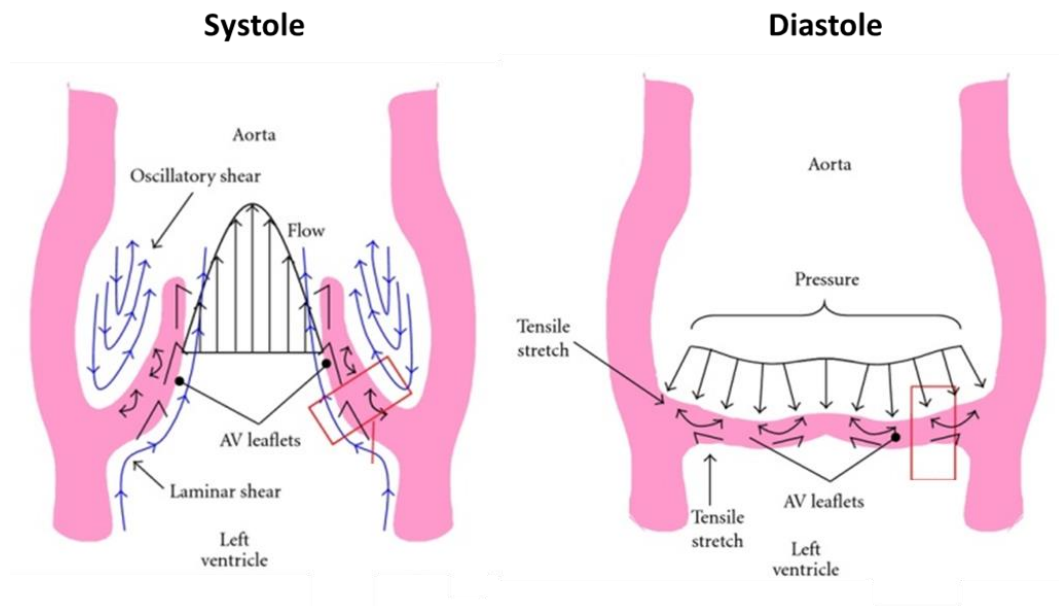


Figure 2.6: The mechanical forces experienced by the valve leaflets during peak systole and diastole [78].

The dynamic motion of the aortic annulus also plays a role in the solid mechanics of the aortic valve leaflets, optimising coaptation during diastole and opening during systole [9]. In systole, the contraction of the left ventricle causes a reduction in the perimeter of the aortic annulus allowing for the valve to open completely, leading to maximum systolic flow. However, during diastole, the perimeter of the aortic root increases by 22% and the myocardial section of the aortic root moves expanding outward as the ventricles relax [9].

2.3 Aortic Stenosis

Diseases of any of the four heart valves can compromise health but diseases in the mitral or aortic valves can lead to dire consequences [62]. For example, if left untreated, the average lifetime for a patient with Aortic Stenosis (AS) is within 2 - 3 years of the onset of symptoms [4-6]. AS is the third most common cardiovascular

disease in developed countries. It occurs in approximately 2.8% of people over the age of 75 making it one of the most common valvular diseases. It has been estimated that 1 million people in the US and 1.3 million people in Europe will develop severe AS by 2025, and these figures are predicted to double in 2050 [81]. AS can be caused by congenital valvular defects or a build-up of calcium deposits on the leaflets of the aortic valve [82-85], which arises as a result of an active inflammatory process [86]. Mechanical stress first causes damage to the endothelium of the leaflets. This then leads to lipid penetration and accumulation of lipids in areas where inflammation has occurred, which is followed by the differentiation of fibroblasts into myofibroblasts. Calcification can be accelerated in some patients due to the differentiation of myofibroblasts into osteoblasts [86], resulting in thickening of the leaflets and calcification [1, 82, 86-88]. As AS progresses the functional area of the valve decreases and obstructs flow through the valve allowing for a significant pressure gradient from the left ventricle to the aorta [70]. The obstruction of blood flow due to AS is considered to be severe when the velocity in the aortic jet is greater than 4 m/s, the EOA (Effective Orifice Area) is less than 1 cm² or the mean pressure gradient is greater than or equal to 40 mmHg or more (Table 2.1) [56, 89].

Table 2.1: AHA Guidelines for Severity of Aortic Stenosis [89].

	Valve Area (cm ²)	Maximum Aortic Velocity (mmHg)	Mean Pressure Gradient (mmHg)
Mild	1.5-2	2.5-3.0	<25
Moderate	1.0-1.5	3.0-4.0	25-40
Severe	0.6-1.0	4.0	40
Critical	< 0.6		

2.4 Surgical Aortic Valve Replacement

The gold standard treatment for AS is Surgical Aortic Valve Replacement (SAVR); this is a highly invasive procedure that requires open heart surgery. However, SAVR currently remains the preferred treatment for patients who have severe degenerative calcific AS [8]. There are two types of surgical heart valves; Mechanical Heart Valves (MHVs) and Bioprosthetic Heart Valves (BHV) [10].

2.4.1 Mechanical Heart Valves

MHVs have been developed over the past 50 years. Several different types of MHVs designs have been developed to date. These include ball-and-cage valves, tilting disc valves, bileaflet valves and polymeric heart valves [10].

Ball-and-Cage Valves

The ball-and-cage valve was the first MHV to be developed [10, 90, 91] and represented a significant development in the treatment of valvular heart disease.

Ball-and-cage valves consist of a silastic ball with a circular ring and a cage formed by three metal arches [12]. Ball-and-cage valves have shown good durability properties, however, the design results in a large pressure drop across the valve in the open position and thus high mechanical stresses in the valve [10]. Ball-and-cage valves also have a relatively large profile that increases the probability of interference with the native structures post-implantation [10]. Further to this, the valve led to high shear stresses in the blood leading to promotion of thrombus formation [92]. Due to the many complications associated with high-pressure drops and poor hemodynamic characteristics accompanying these valve types they are no longer implanted [10, 12, 93, 94].

Tilting Disc Valves

Tilting disc valves were introduced with the aim of overcoming the poor hemodynamic performance of ball-and-cage valves. A flat disc was used instead of a ball in an effort to reduce the profile of the valve. However, although these valves were lower profile, they were still associated with hemodynamic problems as the leaflet obstructed flow in the open position [10, 95]. This led to the development of a disc that tilted within a valve ring. These tilting disc valves consisted of a single disk secured by either lateral or central metal struts. The disk opened at an angle of 60° to 80° relative to the annulus resulting in two different orifice sizes [12]. This lowers the obstruction of blood flow in comparison with ball-and-cage valves [10].

Bjork-Shiley introduced a significant design concept in 1967 with a valve that involved a free-floating disc. This free-floating disc tilts to an angle, dependent on the design of the disk retaining struts, when in the open position. This design

allowed blood to flow around it leading to a decrease in flow abnormalities [10, 95]. Tilting disc valves have improved hemodynamic characteristics over ball-and-cage valves but have complications such as stent fracture, which has been associated with cavitation [10, 13], wherein bubble formation occurs at the rigid stent and leaflets. Cavitation can lead to eventual failure of the valve leaflets or cause damage to blood cells and increase the risk of thromboembolic complications [10, 96].

Bileaflet Valves

Bileaflet valves were created in an attempt to improve on the hemodynamic complications associated with tilting disk valves and ball-and-caged valves [10]. The design consists of a rigid valve ring that uses small hinges to attach two semi-circular leaflets. The leaflets open at an angle of 75°-90° relative to the annulus. The open valve consists of 3 orifices: a small orifice between the two valve leaflets and two larger semi-circular orifices positioned laterally [12]. Due to the bileaflet design, there is a low possibility of restriction in the movement of the leaflets due to interference with the native structures because the leaflets are positioned in the middle of the bloodstream when opened and remain enclosed within the ring when they are closed [10]. Bileaflet valves allow for a large EOA with less obstruction to the flow compared to earlier generation valves [10]. However, complications in the valve design such as thrombus formation on hinges, valve failure and leaflet escapement (embolization of the heart valve disk) have been reported in bileaflet designs. The rate of thromboembolism associated with MHVs requires the need for lifelong anticoagulation [10, 11].

Polymeric Heart Valves

Polymeric heart valves have a flexible structure used to simulate the stiffness of natural heart valves, allowing them to expand and contract freely conforming to the aortic root during the cardiac cycle. This increases their ability to simulate natural hemodynamics [10, 97]. Currently, polymeric valves are only available for short-term use. A polymeric MHV design for long-term implantation is yet to be developed [10, 98].

2.4.2 Bioprosthetic Heart Valves

BHVs were designed to mimic the anatomy of the native aortic valve [12]. A major breakthrough in the development of BHVs occurred when tissue fixation using glutaraldehyde was found to increase the stability of biological tissue and reduce biodegradation [99, 100]. This allowed for the combination of tissue and mechanical structures to develop heart valves with reduced thrombogenicity [99]. BHVs are made from porcine aortic valves or bovine pericardium tissue leaflets [12, 99]. BHVs can be stented bioprostheses, wherein the tissue leaflets are mounted onto a supporting stent, or stentless, whereby the valves are solely fabricated from whole porcine heart valve or bovine pericardial tissue [12]. Tissues valves with no stent are believed to be preferable as they distribute the mechanical stress of the aortic root into the tissue instead of focusing them on the regions of the leaflet close to the stent [12], however, due to known difficulties of this technique such as longer cardiopulmonary bypass and cross-clamp times compared to those for stented valves many surgeons are reluctant to perform this procedure [101]. The advantage of BHVs are that they are less thrombogenic than MHVs and therefore, do not require the need for anticoagulation treatments [10, 12].

BHVs are effective and durable for many years after implantation. However, their durability is limited to 10-15 years [10, 13]. Although mechanical prostheses require the need for lifelong anticoagulation therapies they assure a long-term solution and are generally preferred for the treatment of younger patients [102]. However, in approximately 30% of patients, their age, poor health and their comorbidities prevent them from having open heart surgery [14]. These patients receive medical management or undergo balloon aortic valvuloplasty treatments, which are considered to be short-term solutions [9].

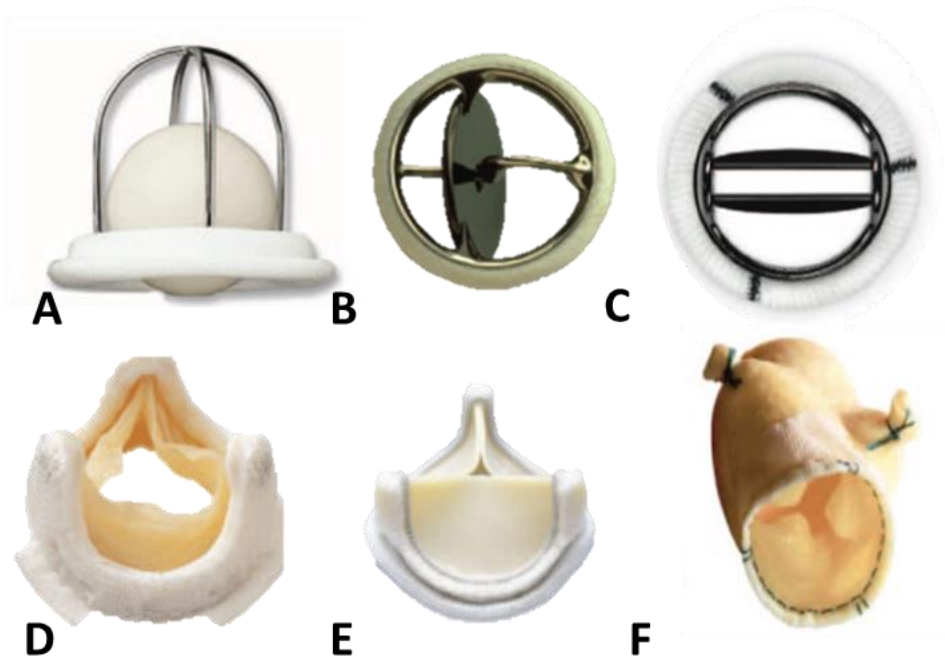


Figure 2.7: Types of Surgical Valves. Mechanical valves (A-C) include A, Caged ball valve (Starr-Edwards); B, Monoleaflet valve (Medtronic Hall); C, Bileaflet Valve (St. Jude); Bioprosthetic valves (E-F) D, stented porcine bioprosthesis (Medtronic Mosaic); E, stented pericardial bioprosthesis (Carpentier-Edwards Magna); F, stentless porcine bioprosthesis (Medtronic Freestyle);) (adapted from [12]).

2.5 Transcatheter Aortic Valve Intervention

Transcatheter Aortic Heart Valve Implantation (TAVI) is a minimally invasive alternative to SAVR. TAVI devices consist of tissue leaflets mounted onto a collapsible valve stent, which is either crimped onto or sheathed into a catheter and delivered percutaneously to the site of the disease. TAVI avoids risks, such as aortic cross-clamping and cardiopulmonary bypass associated with surgical valves, providing a treatment for higher risk patient cohorts [9]. The first-in-human TAVI took place in 2002 [15]. Since the first TAVI procedure over 100,000 patients have

been treated in over 750 different centres using TAVI [22]. The number of centres performing the procedure has doubled in the US in recent years with the procedures showing great outcomes in higher-risk patients with fewer patient complications being reported [103, 104].

2.5.1 Types of Transcatheter Aortic Valves

The first generation commercial TAVs, the Edwards SAPIEN® Valve and Medtronic Corevalve®, received CE approval in 2007 and were approved by the FDA in November 2011 and January 2014 respectively [16, 17]. The Edwards SAPIEN and CoreValve were the first TAV's to receive FDA and CE approval.

The Edwards SAPIEN is a balloon-expandable valve, it consists of tri-bovine pericardial leaflets mounted onto a collapsible cobalt chromium or stainless-steel frame. The frame is percutaneously delivered transfemorally or transapically to the diseased native valve where the balloon uses a radial force to expand the valve frame and force back the native calcified leaflets [9].

The CoreValve is a self-expanding valve, it consists of a porcine tri-leaflet mounted on to a nitinol stent, the valve is crimped and using a catheter, delivered to the site of the disease where the self-expanding nitinol valve stent exerts a radial force to push back the native leaflets and hold the valve in place [9].

Although these first-generation TAVs have shown great success there are still limitations to these TAVs. Such limitations include large diameter delivery sheaths, the recommended size for successful transfemoral access is 18-Fr or less [22] whereas first-generation valves required 24-Fr catheter for delivery of larger valves [105]. Inconsistent positioning also has been shown to lead to problems with

valve embolization, obstruction of the coronary ostias, interference with the mitral valve or the conductance system, PVL or aortic injury, and overcoming these issues is the focus of design evolution and next-generation valves [19-22].

New TAVs have been developed to allow for slower and more controlled deployment of the valve and allow for the valve to be fully repositionable and retrievable, which allows the operator to have greater control over device deployment [22]. Furthermore, due to the fact that TAVs are not sutured into place like surgical valves, there is an increase in the incidence of problems such as PVL and eccentric stent geometries. New devices are attempting to address this by creating better methods of maintaining good stent tissue apposition [22]. However, the durability of the stent frame is still an area of concern when moving into younger patient cohorts [22].

TAV technologies that currently have CE approval include the Edwards balloon expandable SAPIEN XT and SAPIEN 3, which have lower profile delivery systems and changes in valve geometry to improve durability [22]. Alongside these valves there are next generation valves including the Direct flow valve (Direct Flow Medical, Santa Rosa, CA), a non-metallic valve that is anchored into the aortic root with two self-setting polymer rings that allow for repositioning of the valve during the procedure [9, 28], the Evolut R (Medtronic, Minneapolis, Minnesota), a valve with a self-expanding laser cut nitinol frame and a delivery catheter that allows valve repositioning [27] and the LotusTM Valve (Boston Scientific SADRA, Los Gatos, CA), a braided stent with a self-centering, self-expanding nitinol frame and a unique buckle mechanism that allows the valve to be repositionable and fully retractable [9, 26]. Other CE approved valves include the Medtronic Engager, the

St. Jude Portico, Symetis Acurate, the Jena valve and Edwards self-expanding valve the Centra [22]. Alongside these valves, there are many other valves that are currently being developed (Figure 2.8) [9]. It has been shown that these next-generation valves address procedure-related shortcomings and improve patient outcomes such as aortic regurgitation and moderate/severe PVL [106, 107].

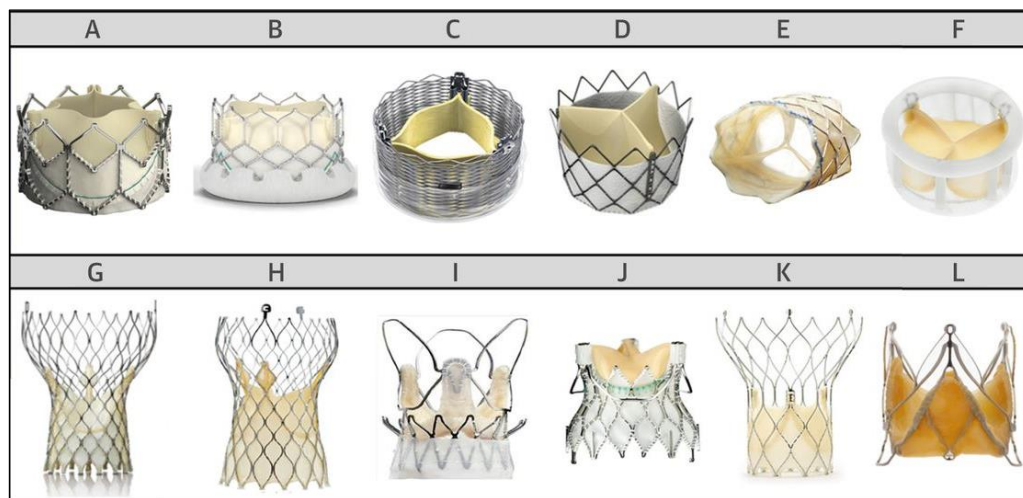


Figure 2.8: Transcatheter Valve technologies include: (A) Edwards SAPIEN XT (Edwards Lifesciences, Irvine, California); (B) SAPIEN 3 (Edwards Lifesciences, Irvine, California); (C) Lotus (Boston Scientific Inc, Natick, Massachusetts); (D) Inovare valve (Braile Biomedica Inc, São José do Rio Preto, Brazil); (E) Melody (Medtronic, Minneapolis, Minnesota); (F) Direct Flow (Direct Flow Medical Inc, Santa Rosa, California); (G) CoreValve (Medtronic, Minneapolis, Minnesota); (H) Evolut R (Medtronic, Minneapolis, Minnesota); (I) Acurate TA system (Boston Scientific Inc, Natick, Massachusetts); (J) Engager (Medtronic, Minneapolis, Minnesota); (K) Portico (St. Jude Medical Inc., St. Paul, Minnesota); (L) JenaValve (JenaValve Inc, Munich, Germany) [108].

2.5.2 Complications of Transcatheter Aortic Valve Implantation

Despite the rapid acceptance and the success of TAVI, there are still many complications and challenges associated with TAVI that remain to be addressed. Ideally, an implanted TAV should provide negligible regurgitation, minimize TVG, and mimic physiological flow patterns, reducing areas of turbulence and high shear flow patterns while avoiding stagnant flow [9].

During SAVR the native stenotic valve is removed and the surgical valve is sutured into place. However, unlike surgical valves, TAVs are not sutured in place. In TAVI the native valve and anatomy play an important role in providing the radial force to secure the valve in place. This leads to a heavy reliance on the tissue-stent interaction in the valve performance [9]. This means there is a higher risk of complications such as paravalvular leakage, stent and leaflet distortion, conductance interference, stroke, device migration, coronary occlusion, and aortic root rupture associated with TAVI procedures. [19-25].

2.5.2.1 Paravalvular leakage

Paravalvular leakage (PVL) is the most common TAVI complication and occurs due to incorrect apposition of the stent to the aortic root [20]. This can be due to an eccentric native annulus, the extent of calcification of the native valve, undersizing or malpositioning of the valve [20]. Currently, there is no accepted treatment for PVL. Post-implantation balloon expansion has been shown to reduce PVL in the most patients however this may lead to cerebrovascular events [20, 109]. The PARTNER trial showed that trace or mild PVL was found in 66% of patients, with moderate to severe PVL in 12% of patients [20, 110, 111]. Year 1 data from the FRANCE 2 trial showed that rates of PVL were higher in the self-expanding

Corevalve (19.8%) than the balloon expandable Edwards SAPIEN (12.2%) [20, 112]. It has been found that moderate to severe PVL is associated with increased mortality rates at 30 days, 1 and 2 years [113-121].

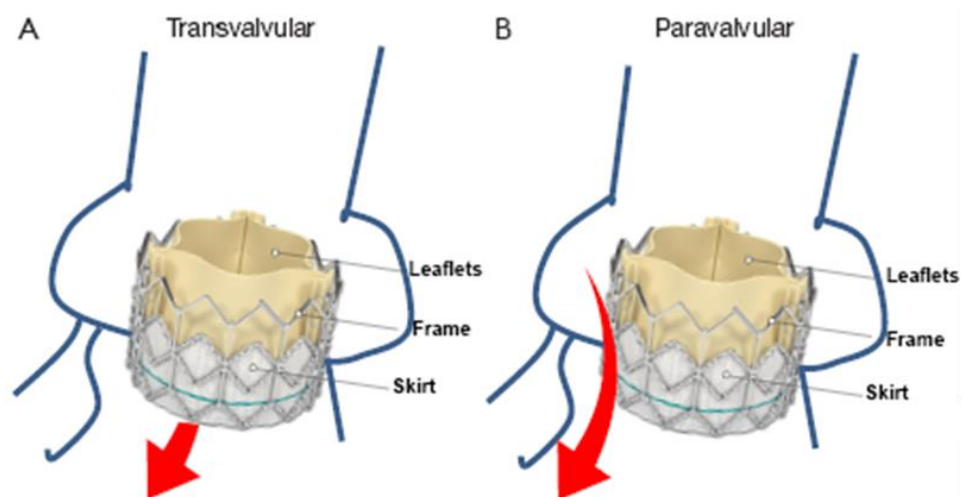


Figure 2.9: Regurgitation mechanisms for TAVI (A) depicts transvalvular leakage occurring due to leakage through the valve and (B) depicts paravalvular leakage occurring between the prosthesis and aortic annulus [122].

2.5.2.2 Stroke

Stroke is a major concern for TAVI patients as it can lead to a significant deterioration in the quality of the life of the patient and may lead to increased risk of death [22]. The rate of cerebral embolism after TAVI has been shown to be nearly as high as 80% in some studies [22, 123-125]. However, in contrast, a meta-analysis of 10,037 patients found the peri-procedural rate of stroke to be 1.5% and the rate of stroke/transient ischemia to be 3.3% 30 days following the procedure [22, 126]. Post-deployment balloon dilation, dislodgement of the valve and new-onset atrial

fibrillation were associated with cerebrovascular events. Similar rates were observed in balloon expandable and self-expanding TAVs [127].

2.5.2.3 Conductance Interference

As previously mentioned in section 2.2.1 the conductance system comes in close proximity to the aortic root in the area under the interleaflet triangle between the right- and non-coronary sinuses. Avoiding injury in this area is of great concern during TAVI procedures, as temporary or permanent conduction abnormalities in the heart, such as Left Bundle Branch Block (LBBB) or atrioventricular block, can arise, which in turn may lead to the need for in-hospital temporary pacing and, if unresolved, PPM [32, 33]. The incidence of new-onset LBBB in patients with TAV implantation has been shown to be 48.8% [128]. It has been proposed that elevated tissues stresses in the tissue close to the AV node could be the cause of injury and thereby lead to conductance issues [32]. A study of 40 patients with a CoreValve ReValving TAV System reported that patients with new-onset LBBB had a significantly greater mean distance from the proximal edge of the valve stent to the lower edge of the non-coronary cusp ($10.3 \text{ mm} \pm 2.7$) compared to patients without new-onset LBBB ($5.5 \text{ mm} \pm 3.4$), thus suggesting that superior positioning of the valve can prevent LBBB conduction problems [36, 37]. More recently it has been shown clinically that implantation depth is a factor in cardiac conduction disorders in TAVI patients [129, 130]. The increased occurrence of cardiac disorders due to lower implantation depth has been attributed to increased risk of compression of the left bundle branch [38].

2.5.2.4 Coronary Occlusion

Coronary occlusion is not a common occurrence in TAVI procedures, occurring in 0.66% of patients. However, it can be life-threatening with a 30-day mortality rate of 40.9% [131]. Predictors of coronary occlusion include female sex, a balloon-expandable valve, lower left coronary artery ostia height and sinus of Valsalva diameters [131, 132]. Coronary occlusion can be treated with percutaneous coronary intervention in most cases [131].

2.5.2.5 Aortic Root Rupture

Aortic rupture is another rare but serious complication of TAVI occurring in about 1% of patients [133, 134]. Risk factors for aortic root rupture include high degrees of sub-annular/LVOT calcification, valve oversizing $\geq 20\%$ and balloon post-dilatation [135]. Annular rupture is a life-threatening complication, however; it can be treated successfully with open heart surgery if it is immediately recognised [134].

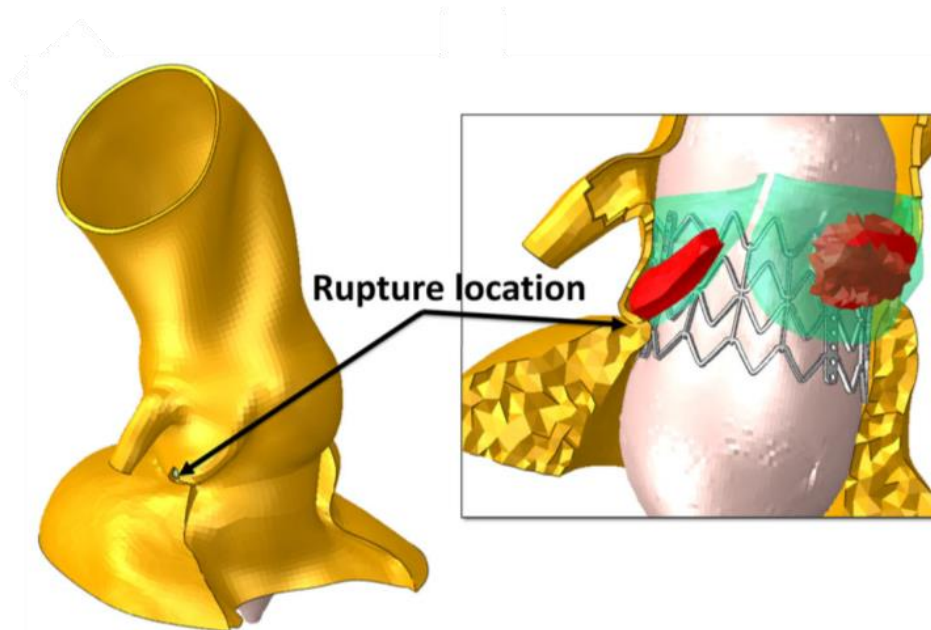


Figure 2.10: A finite element analysis predicting aortic root rupture due to the displacement of calcification into the left coronary sinus [39].

2.5.2.6 Stent Migration and Eccentricity

As mentioned in Section 2.3.2 the dynamics of the aortic annulus play an important role in the mechanics of the aortic valve leaflets [9]. When a TAV is placed in the aortic root the TAV relies strongly on the interaction between the TAV stent and the dynamic aortic root, because it is not sutured into place. The TAV stent will experience both antegrade and retrograde forces from the systolic blood ejection and retrograde forces from the pressure gradient across the closed valve in diastole [9, 136]. In systole TAVs also experience compressive and torsional forces due to ventricular contraction [9].

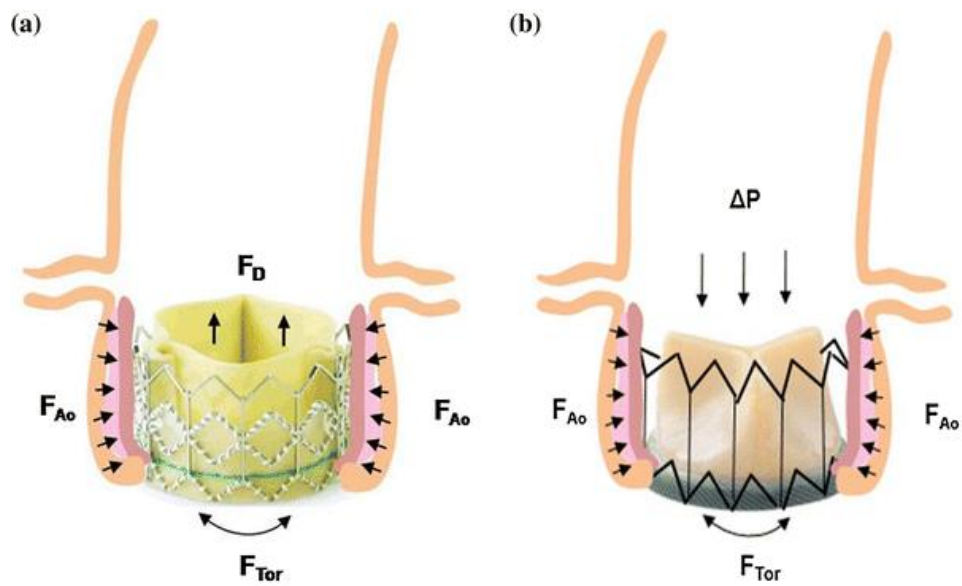


Figure 2.11: Forces experienced by a TAV in (a) systolic ejection and (b) diastolic closure. Where F_D is the pressure force acting on the valve, F_{Ao} is the radial force of the valve on the aortic root, F_{Tor} is the torsional force on the stent due to the motion of the aortic annulus and ΔP is the pressure gradient across the closed valve [9].

Dwyer *et al.* used Computational Fluid Dynamics (CFD) to investigate stent migration forces, finding the antegrade force to be 10 times smaller than the retrograde force (6.01 N) with the dynamic pressure gradient being the largest contributor to the migration force experienced by TAVs [45]. Similar axial force values (5.8 – 6.1 N) were found when using FEA (Finite Element Analysis) to apply a static diastolic pressure to TAV leaflets [42]. For the balloon expandable Edwards SAPIEN it is important that the elastic recoil of the stent must be less than that of the recovery geometry of the aortic root to prevent the stent from dislodgement into the aorta due to axial loads [9, 137]. The CoreValve must exert a large enough radial force so that dislodgement into the left ventricle does not occur due to retrograde

forces during annular relaxation [9, 137]. It has been previously shown, using numerical analysis to investigate different mechanisms of radial force exerted on the annulus, that the hoop forces of the CoreValve vary from 2-7 N in aortic annuli ranging from 20 – 23 mm and Edwards SAPIEN has a hoop force of 12-14 N when deployed in a 22 mm aortic annulus of varying stiffness [137]. One of the advantages of self-expanding stents is this lower radial force that allows the stent to conform to the aortic root. This is thought to be advantageous in reducing volumes of PVL [29, 138, 139]. However, clinically, higher volumes of PVL have been seen in the CoreValve. This increase may be due to malpositioning of the stent allowing for leakage through the uncovered cells [20]. The disadvantage of conformance of the stent to the aortic root geometry is that it leads to eccentric stent geometries. Eccentricity is a measure of stent distortion which can be quantified using [140]:

$$e = 1 - \left(\frac{D_{min}}{D_{max}} \right) \quad (\text{Eq. 2.1})$$

where D_{max} and D_{min} are the major and minor axes of the ellipse respectively and zero is the optimal eccentricity.

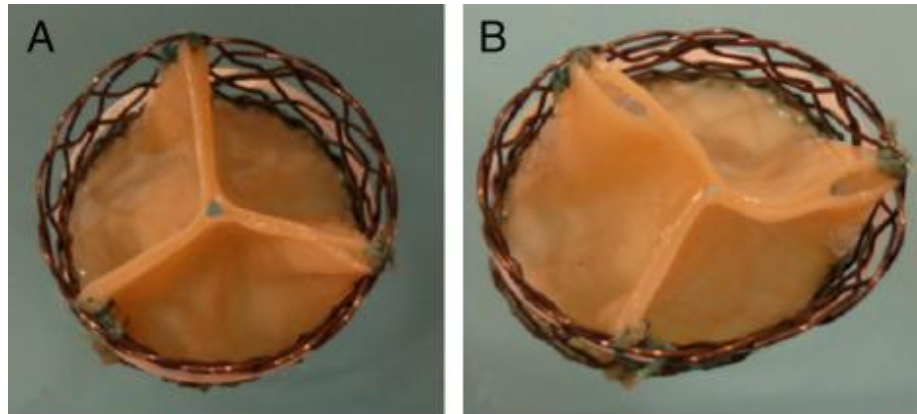


Figure 2.12: (a) Circular valve stent with no leaflet distortion present and (B) elliptical stent with visible leaflet distortion [141].

Clinically, the CoreValve has shown non-uniform and incomplete expansion at all levels of the stent [138]. Whereas, when circularity is considered as an eccentricity of $<10\%$, circularity was observed in only 17% of patients ($n=5$) with the CoreValve. Circularity was only observed at the level of the commissures and central coaptation [136, 138].

The CENTRA (Edwards Lifesciences) self-expanding valve was found to have an eccentricity of between $18.7 \pm 10.9\%$ at the inflow level, which did not differ from that of the annular eccentricity pre-TAVI which was $19.4 \pm 11.5\%$ [142]. It has also been found that the self-expanding Portico (St Jude Medical) had an eccentricity of $12.0 \pm 7.3\%$ at the valvular level. One case out of ten showed intermittent leaflet dysfunction with 18% eccentricity observed at the valvular level [143]. A study by Zegdi *et al.* found asymmetric stent expansion occurred in 32% of patients with severely stenosed tricuspid aortic valves. However, this was seen to increase to 86% in BAVs [141].

Numerous studies have shown that eccentric stent geometries can lead to leaflet distortion [9, 42, 138, 141-143]. It has been shown that leaflet distortion may lead to irregular leaflet kinematics with increased peak stress concentrations in the valve leaflets and altered fluid mechanics [29, 42, 139, 144]. It has also been shown with BHVs that distortion of the valve leaflets leads to premature fibrosis, calcification and deterioration of the leaflets [145].

2.5.3 Procedural Considerations of Transcatheter Aortic Valves

Case Selection

Since regulatory approval of TAVs, there has been debate over the classification of the difference between high risk and prohibitive risk AS patients. Currently, online risk scores such as EuroSCORE and the Society of Thoracic Surgery are used in risk assessment [22]. However, these score systems do not take into account a series of patient co-morbidities, such as severe pulmonary hypertension, right ventricular dysfunction, severe liver disease, prohibitive anatomy, disability, or frailty [22]. It has been shown that costly and invasive therapies in patients with very severe co-morbidities do not offer any real benefit [146]. There is a need to overcome one of the biggest challenges in the assessment of patient risk through the development of a quantitative algorithm for risk assessment [22].

Valve Sizing and Positioning

The challenge of valve sizing and positioning in TAVI procedures should not be underestimated. It requires meticulous examination of MSCT images and transesophageal echocardiography [22]. It has been shown that incorrect positioning and sizing of TAVs can cause adverse effects such as the extension of the heart valve into the left ventricle, mitral insufficiency, arrhythmias, PVL, prosthesis embolization, coronary obstruction, or aortic injury [19-22]. In particular, there is much debate over sizing in relation to BAV patients. Due to the abnormal valve geometry of BAVs, the treatment of BAV stenosis with TAVI is still considered off-label [54, 55]. There are particular concerns with PVL and incomplete stent expansion in relation to BAV patients, issues related to under- and over-sizing respectively [20, 58]. With the rapid growth of TAVI, it has been argued that studies including BAV patients have not had adequate sample sizes and recent expert analysis stating that the simple application of traditional annulus measurement and device sizing are not necessarily appropriate in treating BAV stenosis [58].

2.6 Biomechanical Evaluation of Transcatheter Aortic Valves

2.6.1 Experimental Studies

Regulatory guidelines required for regulatory approval of Heart Valves are outlined in the International Organization For Standardization (ISO), ISO 5840:2005, “Cardiovascular Implants - Cardiac Valve Prostheses”[147]. This outlines the need for bench tests including; material property testing, biological safety, structural performance, MRI safety, accelerated wear testing, fatigue testing of different valve components, durability & hydrodynamics performance. Further to this additional

device-specific testing may also be required. More in depth details of the design validation can be found in [147].

Previous studies using *in vitro* experiments to assess the hemodynamics and structural mechanics of TAVs are outlined below in Sections 2.6.1.1 and 2.6.1.2.

2.6.1.1 In Vitro Hemodynamics

Particle Imaging Velocity (PIV) has been widely used in investigating hemodynamics of TAVs in-vitro. PIV is an optical method of flow visualization that involves measuring the average displacement of a group of tracer particles, illuminated by a laser light sheet, in the fluid over a given time [148]. A study to assess the velocity fields of the Edwards SAPIEN valve showed it has the potential to imitate near physiological flow conditions [149]. Using PIV, it was shown that for the Boston Scientific LotusTM Valve, the buckle region of the valve does not significantly increase the potential of hemolysis [26]. However, a study investigating the hemodynamics of the sinuses of Valsalva using PIV found that both the CoreValve and Edwards SAPIEN implants reduced flow in the Valsalva sinuses allowing for regions of stagnation at the bases of the sinuses, which could be associated with ischemic events [150]. PIV has also been used to investigate the impact of suboptimal deployment conditions. A study investigating noncircular deployment of the Edwards SAPIEN XT found that deployment into non-circular aortic annuli leads to increased transvalvular leakage. Although, it was also found that pressure gradients were not influenced by valve distortion [151]. In a study by Kuetting *et al.*, the regurgitant flow, EOA and systolic pressure TVG across a Medtronic CoreValve were assessed at different degrees of ovality using PIV [152]. It was found that, for the CoreValve, increasing ovality led to an increase in

regurgitation and the pressure difference across the valve, with only a slight impact on the EOA. High-speed videos showed minor leakage and reduced apposition at higher ovalities. However, no interaction between the leaflet and the valve stent was observed [152]. Gunning *et al.* used PIV to assess the impact of eccentric deployment on hemodynamic performance of TAVs finding that the EOA and TVG did not differ substantially from circular deployment. However, it was found that eccentric TAV deployment leads to asymmetric jet formation with increased shear stresses and regions of turbulence indicating potential for hemolysis [139]. A study investigated the positioning of TAVs using an *in vitro* heart-flow simulator and analysed the fluid dynamics of the flow using digital PIV. The results of that study revealed that blood residence time and aortic fluid shear stresses are favourable if the position of the annulus of the TAV is as close to the native aortic annulus as possible [153]. The limitation to these *in vitro* studies is that many use silicone or other materials to represent the aortic root, not allowing for accurate assessment of the tissue-stent interaction.

2.6.1.2 In Vitro Mechanics

The tissue-stent interaction has been previously quantified experimentally using an *in vitro* model, which involved carrying out a radial force test on a braided stent that was then deployed into porcine and ovine aortic roots. Post-deployment ultrasound images were taken of the deployed stent and the stent dimensions were measured. From the stent dimensions, the radial stent expansion force was extrapolated from radial force test data. An axial stent pullout force test was performed and using the ratio of the pullout force to the radial force the coefficient of friction was calculated [46]. This study showed that the radial force increased by

30-40% when crimped at body temperature versus room temperature, the coefficient of friction between the TAV and aortic root was 0.10 ± 0.01 , the minimum dilation of the aortic root was 2.5 mm and a radial expansion force of 60 N was needed to anchor the stent in the aortic root and avoid migration [46]. However, this study is limited due to the fact that calcification of the leaflets and the stenotic aortic root and their impact on the biomechanical interaction were not taken into account.

2.6.2 Computational Studies

Finite Element (FE) modelling is widely used in the design and assessment of TAVI devices and is required by the FDA to evaluate the mechanics and kinematics under appropriate conditions [154]. Modern imaging modalities allow for the accurate reconstruction of patient-specific models which can inform decision making regarding the design of TAV devices and preoperative planning [155]. FEA has been used to investigate both the deformation and stress distribution of the valve leaflets, and to investigate the tissue-stent interaction between the TAV and the aortic root.

2.6.2.1 Leaflet Modelling

FEA has been used to evaluate the stress distribution, coaptation and deformation of valve leaflets. A study by Li *et al.* examined the deformation of a percutaneous aortic heart valve design with glutaraldehyde-treated bovine and porcine pericardium under different static, pressure only, loading conditions [156]. The deformation of the valve leaflets was modelled by applying a uniform TVG of 120 mmHg to the unloaded valve. The study examined the impact of tissue thickness and anisotropy on the valve deformation and stress distribution. It was found that

the peak maximum principal stress and strain occurred at the commissure regions of the leaflet with the lowest stress and strain observed at the free edge of the leaflet when under 120 mmHg loading conditions. The study also found that the maximum principal stress of bovine pericardium leaflets (915.62 kPa) was lower than that of porcine pericardium (1565.80 kPa). Furthermore, it was also found that smaller leaflet thickness indicated higher tissue stress [156]. Smuts *et al.* similarly used FE methods to inform the design of tissue leaflets for a percutaneous valve. Biaxial testing was performed on the leaflets and a FE model of the biaxial test was used to validate the material models of the tissues. FEA was then used to apply a 230 mmHg pressure gradient across two different valve designs. It was found that kangaroo pericardium was favourable over bovine pericardium as it has lower thickness and greater extensibility [157]. Sun *et al.* combined FEA and CFD to investigate the deformation and degree of central backflow leakage of different idealised eccentric TAV geometries [42]. It was found that an eccentricity of 0.267 leads to a predicted increase of 143% in the peak stress in the leaflet when compared to a circular TAV. It was also found that if the eccentricity was greater than 0.134 backflow leakage was predicted [42].

Current guidelines for TAVI suggest upsizing the device relative to the native annulus to reduce volumes of PVL, however, this may lead to incomplete stent expansion [138, 158, 159]. Abbasi and Azadani used FE modelling to investigate the stress and strain patterns of leaflets in incompletely expanded TAVs [159]. A 3D laser scanner was used to obtain the geometry of the leaflets of a 23 mm Edwards SAPIEN XT, the TAV was then expanded in diameters ranging from 18 to 23 mm. A computational model was created to apply a pressure waveform

representing the cardiac cycle to the extracted leaflet geometries. It was shown that after complete expansion the highest stress regions were observed in the commissure regions of the valve. A 2-3 mm incomplete expansion of the TAV stent led high localised stresses in the commissure region, whereas a 4-5 mm incomplete expansion of the TAV stent led to high localised stresses in the belly region of the leaflets. This indicates underexpansion of TAV's may lead to accelerated tissue degradation and reduce long-term valve performance [159].

Martin *et al.* created a fatigue damage model to assess the effect of leaflet and stent elastic properties for glutaraldehyde-treated bovine pericardium BHVs [160]. This model included stress softening and permanent set for glutaraldehyde-treated bovine pericardium leaflets [161]. It was found that the heterogeneity of the leaflet elastic properties, poor leaflet coaptation and little stent-tip deflection lead to an acceleration in the fatigue of the valve leaflets [161]. In addition to this, a fatigue simulation model was also used to compare the durability of TAVs with BHVs. The results suggested that the durability of TAVs is significantly reduced when compared to BHVs [162]. Furthermore, the impact of under expansion of TAVs on leaflet durability was investigated and it was reported that an underexpansion of $\geq 9.1\%$ can significantly impact device durability [163]. This lies within the range of current guidelines that consider 10-15% under expansion acceptable [163, 164].

Bailey *et al.* deployed a SAPIEN XT into a patient-specific aortic root at eight different orientations (15° increments) and found that, for that patient, aligning the prosthetic leaflets with the native leaflets was the optimal position for decreased leaflets stress [165]. Using a computational simulation of TAVI

deployment into a patient-specific root it was shown that excluding the leaflets from the valve stent leads to negligible (0.236%) discrepancies in the average frame position [166].

2.6.2.2 Tissue-Stent Interaction

Among the first studies to use patient-specific modelling to investigate percutaneous valve implantation were the investigations of pulmonary valve implantation using patient-specific FEA to investigate stent fracture by Schievano *et al.* [167, 168]. This study showed the impact of realistic geometries on the final configuration of the deployed device and the importance of investigating patient-specific models to assess device performance [167, 168]. In recent years there has been a push to develop computational models to investigate the impact of patient-specific geometries on the tissue-stent interaction for TAVs and also to provide an enhanced understanding of specific procedural complications.

A study by Gessat *et al.* was one of the first studies to investigate the deformation of a TAV stent in a realistic patient geometry using CT images of an implanted CoreValve stent and using a spline-based method to measure local deformation of the stent [169]. In a more recent study, Gessat *et al.* have used an iterative relaxation method to adapt information extracted from CT images and implement it into an FE model of a CoreValve stent and use it to calculate the radial forces between the stent and tissue [170]. However, these studies do not include the surrounding tissue and the deployment process making the mechanisms of this deformation difficult to fully understand.

Capelli *et al.* and Wang *et al.* were among the first studies to apply patient-specific FEA to investigate TAVI [40, 41]. Capelli *et al.* developed five patient-specific geometries modelling the deployment of the balloon expandable Edwards SAPIEN valve demonstrating the feasibility of valve-in-valve implantation in four patients with different degenerated BHVs and one native stenotic valve. The patient-specific roots were modelled using shell elements and the isotropic Mooney-Rivlin model fitted to experimental test data of human ascending aorta was used to model the aortic root behaviour. Calcification was modelled by increasing the Young's modulus and thickness to 10 MPa and 1.4 mm respectively in the region of the commissures. It was found that the stresses in the aortic root were approximately ten times higher when the stent was deployed in native root versus those seen in the aortic root in the presence of a BHV suggesting BHVs act as a scaffold for the TAV stent [41]. Wang *et al.* used a patient-specific model incorporating the aortic sinus, the ascending aorta, the native leaflets and the surrounding myocardium. The materials were modelled using an anisotropic material model. The model was used to investigate the biomechanical interaction when a TAV is deployed into an aortic root at normal pressure conditions taken from MSCT scans as well as rapid pacing which was found by uniformly applying at -10% strain to the reconstructed geometry [40]. It was found that the contact forces, stress and strain predicted were higher in the rapid pacing model than the model of the MSCT scans. This model included the native leaflets, with the basal plane of the leaflets stiffened using the material properties of hydroxyapatite to represent the calcifications. The potential for PVL and occlusion of the coronary ostia was also predicted [40].

Tzamtzis *et al.* investigated the radial force exerted by the balloon expandable Edwards SAPIEN and the self-expanding CoreValve. It was found that the force exerted by a self-expanding stent is dependent on the diameter of the LVOT while for balloon expandable valves the radial force is dependent on the tissue stiffness and the geometry. It was shown that the hoop forces exerted by the CoreValve vary from 2-7 N in aortic annuli ranging from 20 – 23 mm whereas for the Edwards SAPIEN a hoop force of 12-14 N was predicted when deployed in a 22 mm aortic annulus of varying stiffness. However, the hoop forces produced by the two prostheses in their recommended ranges were very similar [137].

A study by Gunning *et al.* [29], used a simplified patient-specific aortic root geometry without the inclusion of the native leaflets and calcification to show the effect of positioning on the tissue-stent interaction and the TAV leaflets. The aortic root was modelled using shell leaflets with an assigned thickness of 2 mm and the aortic root was modelled as a homogenous isotropic hyperelastic material using the Mooney-Rivlin material model. It was shown that positioning of the TAV can affect the stent distortion which can lead to increased leaflet stress and that aligning the commissures of the TAV with the commissures of the native valve was shown to reduce the effect of stent distortion on leaflet stress (Fig. 2.13).

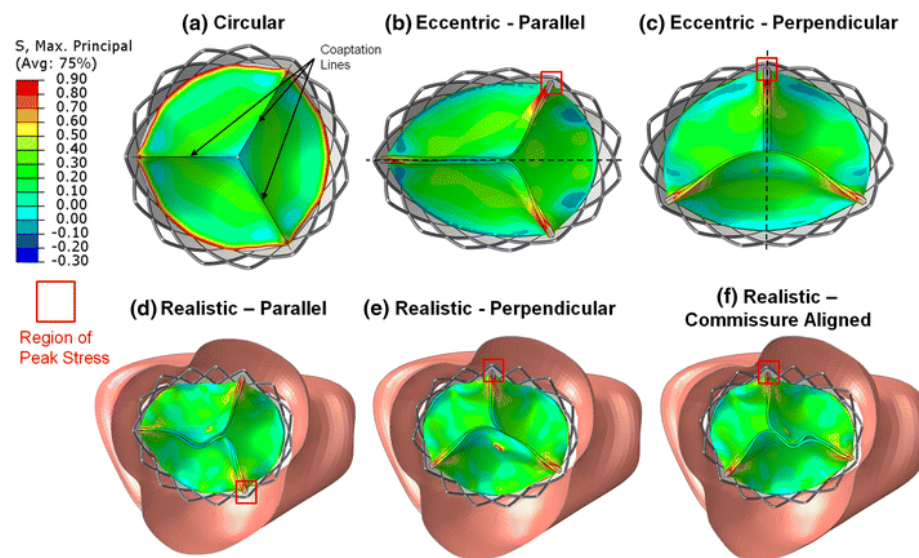


Figure 2.13: Image from Gunning *et al.* depicting the 99th percentile maximum principal stress in TAVI leaflets under idealized deployment conditions: (a) circular, (b) eccentric-parallel and (c) eccentric-perpendicular and under realistic deployment conditions in (d) realistic-parallel, (e) realistic-perpendicular and (f) realistic commissure aligned orientations. Where the red boxes indicate regions of peak stress [29].

Another study similarly used a simplified aortic root without the native leaflets or calcifications and investigated positioning of the Edwards SAPIEN valve [31]. The aortic root was assigned a uniform thickness of 1.3 mm and modelled as homogenous using an anisotropic material model. It was found that when the Edwards SAPIEN was positioned directly under the coronaries there was a 24.2% decrease in leaflet coaptation, 13.5% increase in the average leaflet stress with a 22.4% decrease in stress on the aortic root versus a 7 mm lower implantation position (Fig.2.14) [31].

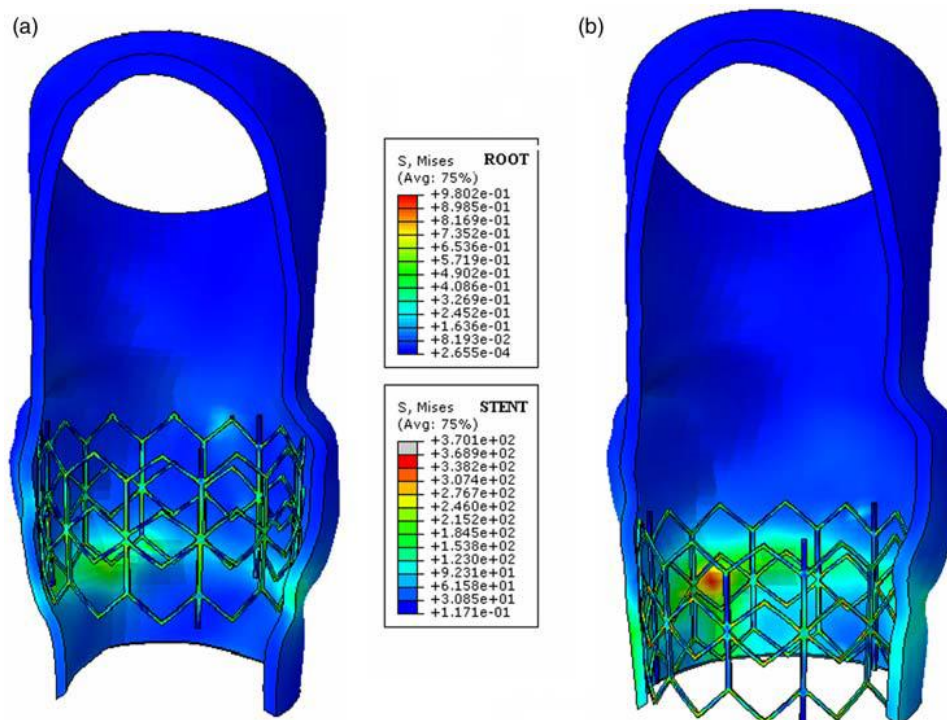


Figure 2.14: Simulation results from Auricchio *et al.*: the von Mises stresses on the aortic root wall and stent struts are represented (a) after distal positioning and (b) after proximal positioning [31].

Implantation depth was also investigated using the CoreValve, this model included the native leaflets and calcifications [30]. Simplified St. Venant-Kirchhoffs material properties were used to model the aortic root, native leaflets and calcifications. For the CoreValve it was predicted that, depending on the implantation depth, differences of up to 41.3% in the stent root contact area, 12.7% in the maximum von Mises stress, 63.4% in the paravalvular orifice area and 40.2% differences in leaflet coaptation were observed [30].

A study by Bianchi *et al.* examined the likelihood of migration of a balloon expandable Edwards SAPIEN valve at three different deployment positions (Fig

2.15). A patient-specific FE model of an isotropic hyperelastic aortic root with an assigned thickness of 1.56 mm was created. The leaflet thickness was varied dependent on leaflet radius (ie. thicker at the base) and the calcifications were modelled as linear elastic. Using the patient-specific model expansion of the stent was simulated at the position defined as distally (stent shifted 30% supra-annularly), proximally (stent shifted 30% sub-annularly) and midway (annularly), anchorage of the stent was based on the contact between the stent and native valve during deployment and recoil. It was found that when the stent was deployed proximally there was a higher risk of migration versus the valve stent being positioned distally or midway [171].

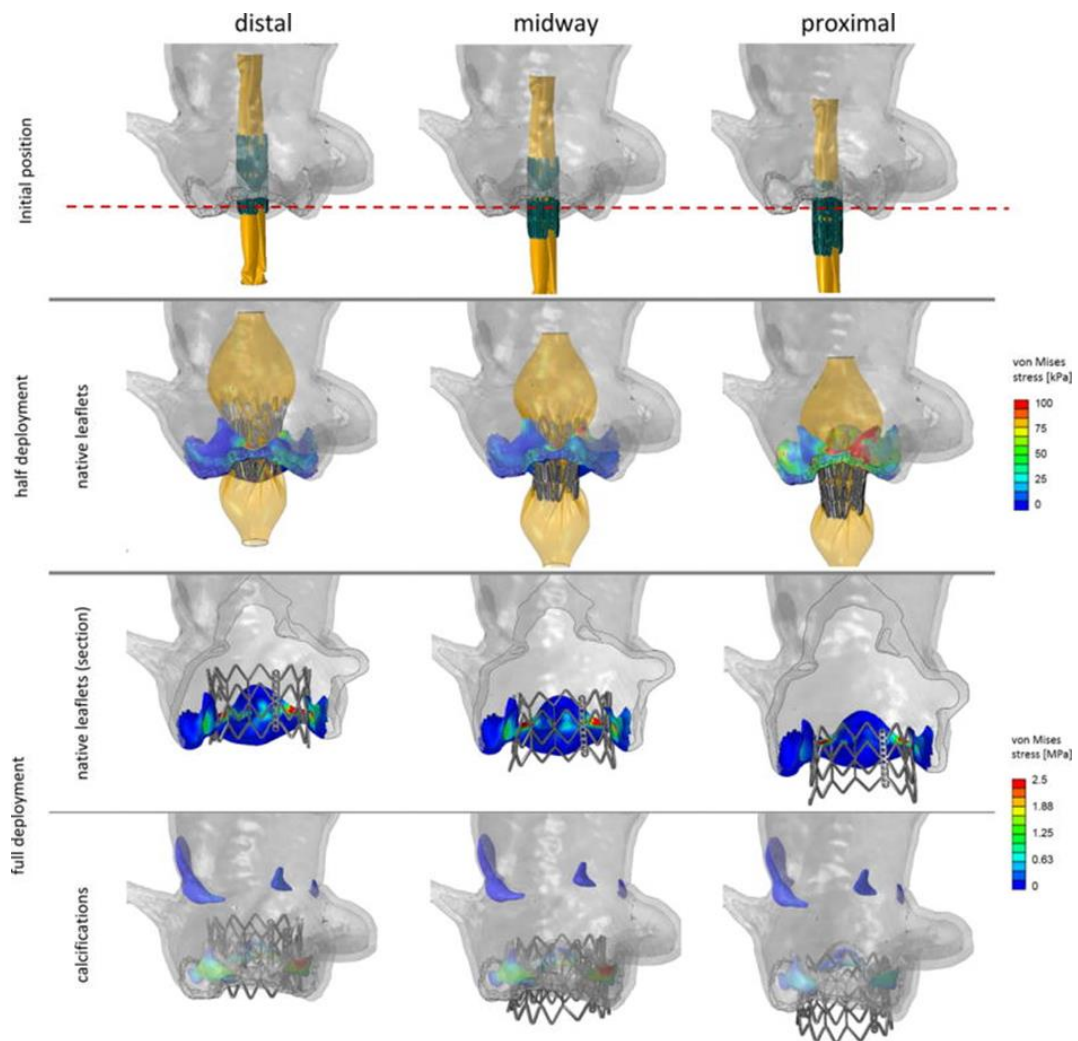


Figure 2.15: Various stages of the stent deployment for the three deployment locations. Von Mises contours are plotted on the native leaflets (second and third rows) and calcium deposits (fourth row) [171].

In a study to better understand the biomechanics of aortic root rupture, three patient-specific cases (one retrospective and two prospective) were modelled to investigate the potential for aortic root rupture [39]. This model included the aortic root, aortic leaflets, calcification, anterior mitral leaflet, and surrounding myocardium modelled with the anisotropic hyperelastic Holzapfel-Gasser-Ogden (HGO) model. The retrospective study simulated the aortic rupture in the same

position as seen in clinical observations. The prospective studies predicted results were in agreement with clinicians decisions and resulted in one cancelled procedure and one successful TAVI [39]. It was shown by Sturla *et al.* using FE methods that aortic valve calcification can lead to variation in three clinically relevant areas. Firstly, stent deformation known as “dog-boning”, whereby the stent exhibits larger expansion at distal portions, is dependent on specific calcification patterns; with dog-boning more evident in cases with more calcific leaflets. This can lead to localised gaps between the stent and tissue. Secondly, higher stress distribution on the calcium deposits which can lead to embolization and potential stroke. Thirdly, higher stress in the aortic valve and aortic root [172]. Two patients that underwent TAVI were examined by Morganti *et al.* who modelled the deployment of the Edwards SAPIEN TAV into both aortic roots. The roots were modelled including the native leaflets and calcifications. The root was modelled using the isotropic hyperelastic Yeoh model fitted to experimental human test data, the aortic wall and leaflets were assigned thicknesses of 2.5 mm and 0.5 mm respectively. The calcifications were modelled using linear elastic properties. This study was in agreement with previous studies showing stent eccentricity in a calcified aortic root with asymmetric coaptation and predicted PVL [173].

Russ *et al.* used FE virtual planning to acquire a patient-specific model of a TAVI patient using a calcified aortic root including the segmented calcifications from the patient-specific geometry showing the importance of the inclusion of the native leaflets and calcifications on the tissue-stent interaction [174]. Grbic *et al.* also used machine learning algorithms to automate the extraction of the aortic root, leaflets and calcification from CT images. This study demonstrated that stent

geometries could be predicted with minimal error when compared to post-TAVI CT images [175]. Finotello *et al.* examined different modelling techniques by varying mesh size and material data (Fig. 2.16) and compared the results of the models to post-op data of the final stent geometry to investigate the trade-off between computational complexity and clinical reliability [176].

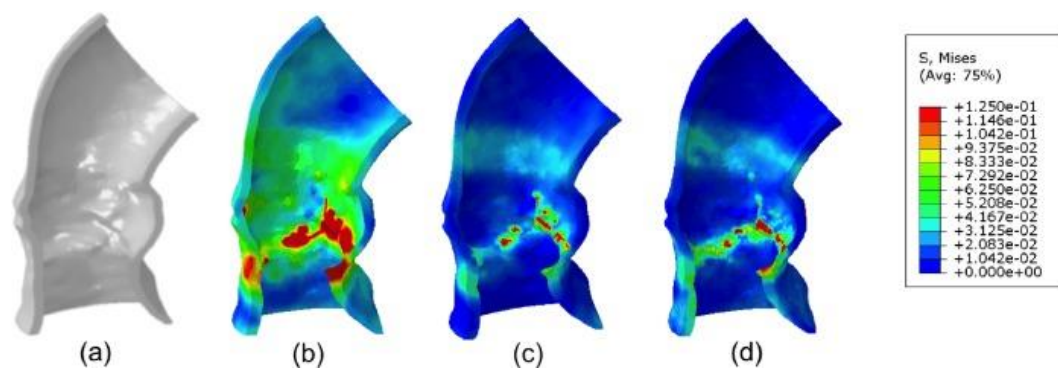


Figure 2.16: Contour plots depicting the von Mises stress distribution on the aortic root wall induced by stent expansion is in a : (a) rigid configuration; (b) an isotropic linear elastic; (c) a non-linear isotropic hyperelastic (d) an anisotropic Holzapfel–Gasser–Odgen (HGO) material model. Stress is expressed in MPa [176].

While the studies discussed in this section offer valuable insight into the biomechanics of TAVs, these studies have not examined injury in the vicinity of the bundle of His, the impact of calcification on securing the valve in place or investigated the post-deployment configuration of TAVs implanted in a bicuspid patient anatomy.

2.7 Summary

This chapter has provided an overview of the aortic valve, its anatomy and function. Further to this, the function and limitations of heart valve replacements, in particular of TAV devices, were summarised. The studies referenced in this chapter

discuss TAV performance and the complexity of the tissue-stent interaction, with a focus on the complications associated with TAVs. Even with the vast amount of knowledge of TAV devices, the role of calcification on the tissue-stent interaction and the levels of stress that are acceptable while avoiding permanent damage to the heart's conduction system are not fully understood.

To address the deficit in the knowledge the studies presented in the following chapters of this thesis aim to quantify the tissue-stent interaction for TAVs and investigate the impact of the stresses induced by a TAV on the heart's conduction system. Chapter 3 investigates the positioning of TAVs and its relationship to LBBB. Chapter 4 investigates the impact of calcification on the tissue-stent interaction. Chapter 5 combines knowledge gained from Chapters 3 and 4 to investigate the stress relating to LBBB using a computational approach. Finally, in Chapter 6, the developed modelling techniques are used to investigate a bicuspid patient anatomy and how such an anatomy affects valve sizing procedures.

Chapter 3: The Impact of Implantation Depth of the Lotus™ Valve on Mechanical Stress in Close Proximity to the Bundle of His

3.1 Introduction

As described in Chapter 2, AS is a degenerative disease of the aortic heart valve associated with the build-up of calcium deposits on the leaflets of the aortic valve. AS is most often treated using a SAVR, a procedure requiring invasive open heart surgery [177]. However, approximately 30% of patients are refused this surgery due to the fact that it is highly invasive and poses significant risk to elderly patients [178]. TAVI is a minimally invasive alternative to SAVR in the treatment of AS.

The aortic valve is located between the mitral valve and the ventricular septum [36]. The close proximity and the potential for interference with the structures of the native valve anatomy make positioning of TAVs crucial for valve performance and patient outcomes. Indeed, recent studies have shown that incorrect positioning of TAVs can cause adverse effects such as the migration of the heart valve into the left ventricle, mitral insufficiency due to the expansion of the aortic valve under TAV implantation, arrhythmias, PVL, prosthesis embolisation or aortic injury [19-21, 179]. An increase in the occurrence of conduction pathway disorders (LBBB) has also been observed when TAVI treated patients were compared to those with surgical valve replacements. Incidences of new-onset LBBB have been reported to be between 8 and 30% for balloon expandable valves

(438 patients from 5 studies) [47] and 25-85% (738 patients in 11 studies) for the self-expanding Medtronic CoreValve [47]. The impact of LBBB in patients with valvular disease has not been widely investigated however, it has been indicated that TAVI-induced LBBB is an independent indicator of mortality [49].

In the aortic valve complex, under the commissures of the native valve lie the interleaflet triangles. The triangle between the right- and non-coronary sinuses contains the bundle of His (Figure 3.1), which is part of the heart's conduction system and an extension of the AV node [32, 33]. It has been proposed that elevated tissue stresses can trigger an inflammatory response, particularly in this region of tissue in close proximity to the heart's conduction system and can lead to a risk of conduction interference [176, 180]. Indeed, the increase in the incidence of LBBB in the Medtronic CoreValve versus the Edwards SAPIEN has been attributed to the long skirt of the device which may directly interfere with the conduction pathway [64]. It has been confirmed that deeper (sub-annular) implantation depths lead to increased risk of conduction disorders [38]. However, the precise stresses induced by TAVs in the region of the interleaflet triangle where LBBB arises are unknown.

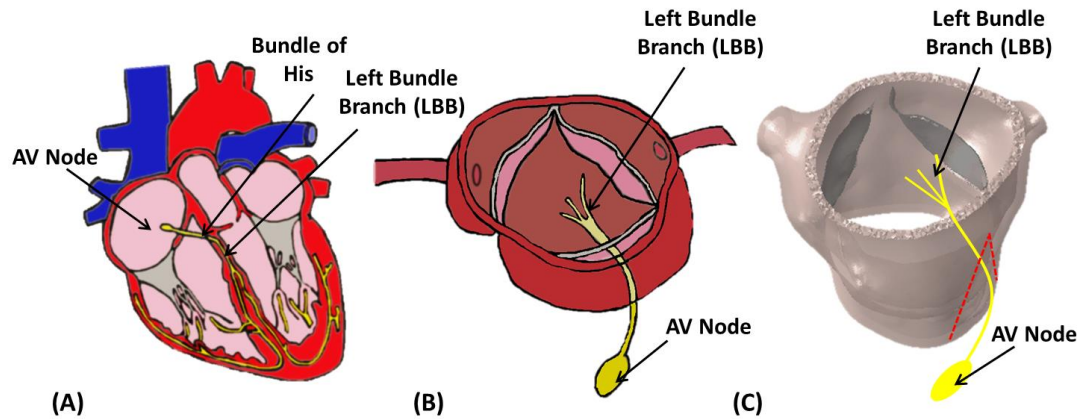


Figure 3.1: (a) Schematic of the heart's conduction system (b) schematic of the aortic valve and the region of the conduction system passing in close proximity to the aortic valve complex (c) the patient-specific model of aortic sinus with schematic representing the AV node and left bundle branch and the path where they pass in close proximity to the valve complex.

As mentioned in Chapter 2, FEA of realistic TAVI patient geometries has been applied to investigate tissue-stent interactions and to provide an enhanced understanding of specific procedural complications. Specifically, patient-specific modelling has previously been used to predict the biomechanical interaction between the TAV and the stenotic aortic root [40] and has successfully predicted aortic root rupture [39]. Furthermore, it has been used in investigating PVL and coronary occlusion [40, 41], asymmetric expansion and leaflet stresses [29, 42] and poor hemodynamic performance [43]. FE methods can provide an insight into the biomechanical interactions during TAVI deployment that cannot be assessed *in vivo*. Such methods have also been applied to investigate the role of positioning for first-generation TAVs. In a study where a FEA was used to implant an Edwards SAPIEN TAV in two different positions along the aortic root (relative to the coronary ostia) it was predicted that a higher implantation depth led to a 24%

decrease in leaflet coaptation area, a 13.5% increase in stress distribution on the leaflets and a 22% increase in the stress distribution on the aortic wall when compared with a lower implantation depth [31]. In a recent study, a Medtronic CoreValve was computationally implanted at different implantation depths and angles in a patient-specific aortic root. The results predicted that deviations in implantation depth can result in variances in the stent-root contact area (41.3%), maximum von Mises stress (12.7%), paravalvular orifice area (63.4%) and differences in leaflet coaptation (40.2%). All these factors can impact the post-operative device performance and durability [30]. Next generation repositionable valves, such as the Lotus valve, are currently under design and development. However, it remains that the relationship between the positioning of the mechanically expanded repositionable Lotus valve and stresses in the aortic root, in particular in the interleaflet triangle, has not been widely investigated.

The first hypothesis of this thesis (Hypothesis 1) that “*Supra-annular positioning reduces stress in the interleaflet triangle in which the conductance system (Bundle of His) resides*” is tested in this chapter. The objective of this research is to apply a patient-specific FE model to investigate the effects of TAV positioning on stress distribution in the aortic root and the valve stent eccentricity. A FE study was carried out to simulate the deployment of a Lotus valve into a patient-specific aortic root at three different implantation depths. The stent eccentricity and stress in the aortic root were compared, and an analysis of levels of stress arising in the vicinity of the bundle of His, as a function of implantation depth, was conducted.

3.2 Materials and Methods

In Chapters, 3, 5 and 6 of this thesis, simulations are described that required the solving of continuum mechanics problems using the commercial FE solver Abaqus (DS SIMULIA, USA). For a detailed outline of the constitutive formulations implemented in Abaqus which are used to describe the mechanical behaviour of the aortic root tissues, calcification and the nitinol stent material can be found in Appendix I of this thesis.

3.2.1 Aortic Root Model

In this study, a patient-specific aortic root geometry was reconstructed from MSCT images (Figure 3.2). These images were obtained from an 81-year-old female with severe AS and had a slice thickness of 0.750 mm, slice dimensions of 512 x 512 and pixel spacing of 0.5 mm. The MSCT scans were electrocardiography gated to examine the 35% systolic phase. This was done to inform decisions regarding specific patient sizing criteria because it represents the point of maximum valve opening. Mimics 14.1 Imaging Software (Materialise, Leuven, Belgium) was used to threshold the leaflets, calcifications and aortic root (aortic sinus and ascending aorta) from the images.

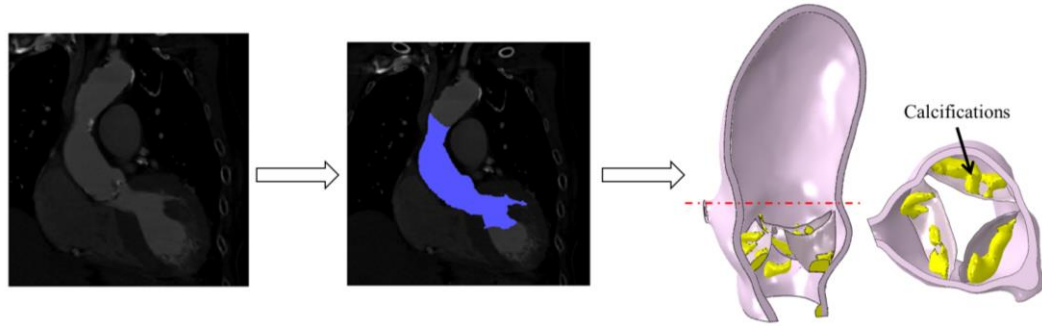


Figure 3.2: Creation of the patient-specific aortic root geometry from (a) the MSCT scan of the aortic root, (b) segmentation of the aortic root using Mimics 14.1 to threshold the MSCT scans and (c) the final aortic root mesh including native leaflets and calcifications.

Volume meshes of the aortic root and calcifications were generated using 3D continuum elements (4-noded tetrahedral elements with reduced integration (C3D4R)). The leaflets were meshed using shell elements with a thickness of 0.5 mm [31]. The geometries were then imported into Abaqus/Explicit 6.13 (SIMULIA, Providence, RI). An assembly was then generated matching the corresponding nodal positions of the intersecting surfaces.

3.2.2 *LotusTM Valve Model*

The Lotus valve stent geometry was created using SolidWorks (Figure 3.3). This was then imported into Abaqus 6.13 as a wire part and was meshed using 3-noded quadratic beam elements (B32). The overlap between the braids was modelled using spring connector elements with an assigned spring stiffness of 1 N/mm. The model of the valve stent was provided by Boston Scientific who performed validation and a mesh sensitivity study for the valve stent model and material parameters.

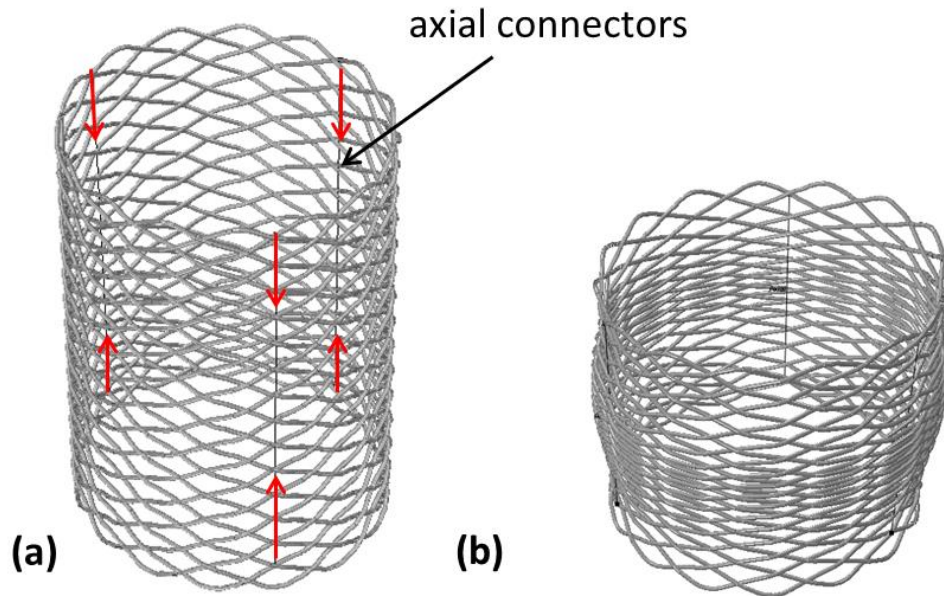


Figure 3.3: The Lotus™ valve stent geometry in (a) unlocked and (b) locked configuration.

3.2.3 Constitutive Models

The Lotus valve stent was modelled using a superelastic material model. An Abaqus 6.13 inbuilt user subroutine (VUMAT), based on the Auricchio and Taylor model, was used in assigning the superelastic properties [181, 182]. Using similar methods to those outlined by Tzamtzis *et al.* a numerical model was correlated to the experimental crush test of a nitinol Lotus valve stent [137].

The ascending aorta and the aortic sinus were modelled as isotropic hyperelastic materials. They were modelled using the first order Ogden model [183] fitted to uniaxial test data of human tissue [40, 184] (Figure 3.4), (Table 3.1). The first order Ogden model [183] strain energy can be defined by:

$$U = \frac{2\mu_i}{\alpha_i^2} \left(\lambda_1^{-\alpha_i} + \lambda_2^{-\alpha_i} + \lambda_3^{-\alpha_i} - 3 \right) + \frac{1}{D_i} (J^{el} - 1)^{2i}$$

where μ_i are α_i material parameters.

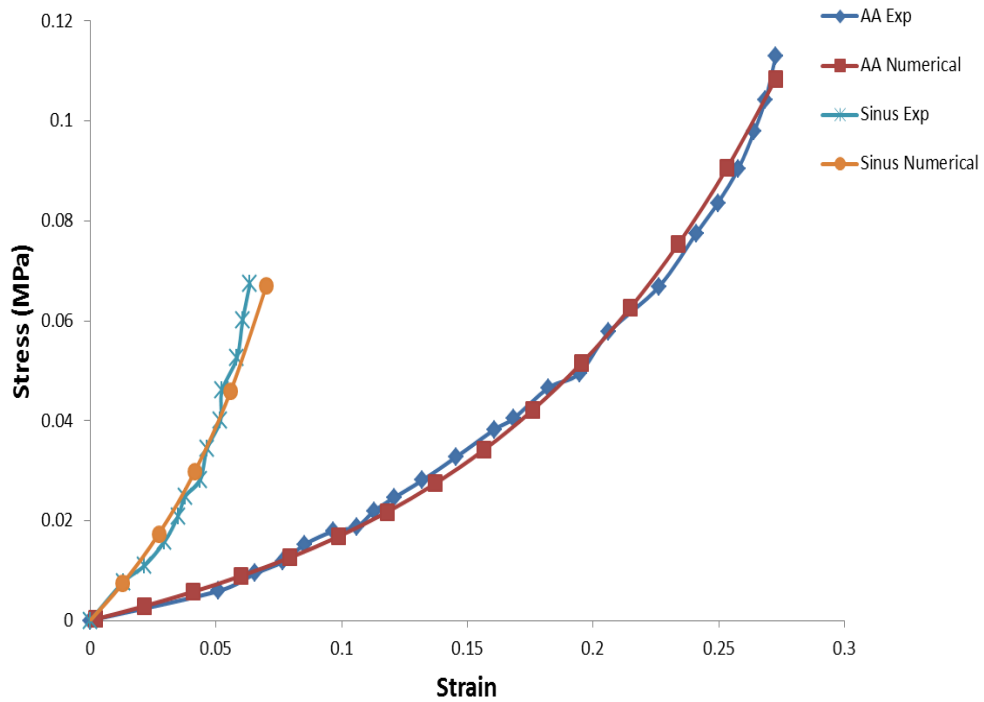


Figure 3.4: Experimental data versus model predictions for the stress-strain response of the human aortic sinus and ascending aorta.

Table 3.1: Material Parameters of human aortic sinus and ascending aorta.

	$\mu 1$	$\alpha 1$	D1
Ascending Aorta (AA)	0.0430	12.4814	0.4667
Sinus	0.1793	25.0000	0.1119

The calcifications were assumed to be isotropic and homogenous. The properties of atherosclerotic plaque were used due to the absence of aortic valvular calcification properties in the literature [185]. A third order Mooney-Rivlin

hyperelastic material model was used, which is defined using strain energy function, U :

$$U = C_{10}(I_3 - 3) + C_{01}(I_2 - 3) + C_{20}(I_1 - 3)^2 + C_{11}(I_1 - 3)(I_2 - 3) + C_{30}(I_1 - 3)^3$$

where I_1 and I_2 are first and second invariants of the Cauchy-Green tensor and C_{ij} are material constants. The material constants used were calibrated by Pericevic *et al.* [186] using data fitted to uniaxial data of atherosclerotic plaque by Loree *et al.* [185]. The following material constants were used in the simulations presented: $C_{10} = 0.495$ MPa; $C_{01} = 0.51$ MPa; $C_{11} = 1.19$ MPa; $C_{20} = 3.64$ MPa and $C_{30} = 4.73$ MPa [186, 187].

The aortic valve leaflets were modelled using a linear stress-strain relationship approximated from biaxial results of aortic valve leaflets tested in the circumferential direction with an elastic modulus of 1.6 MPa, a Poisson's ratio of 0.495 and a density of 1140 kg/m³ [40, 188].

3.2.4 Boundary Conditions

The crimping and deployment of the stent were modelled in Abaqus 6.13 (SIMULIA, Providence, RI) using a cylindrical part (crimper (Figure 3.4)), which was meshed using (SFM3D4R) 4-noded quadrilateral surface elements with reduced integration. A local cylindrical coordinate system was created to displace the crimper inward radially, see Figure 3.4. The crimper was constraint axially and tangentially to prevent sliding. Surface-to-surface hard normal and zero friction contact was assigned to the interaction between the crimper and the stent. The crimper was assigned as the master surface and the stent was assigned as the slave surface. The stent implantation depth was varied relative to the native aortic

annulus, which was defined as a virtual ring connecting the three points of the leaflets at the base of each leaflet attachment [189]. The stent was first positioned annularly with an equal distribution of the stent positioned above and below the annulus (Case 1). During stent deployment, a coefficient of friction of 0.1 and surface-to-surface hard normal contact was used between the TAV stent (master) and the aortic root (slave) [46]. A third loading step was applied to the stent to simulate the locking of the device, which is a feature of the repositionable mechanism in the Lotus valve (Figure 3.3 & 3.4). Three axial beam connector elements were placed to connect the locations of the buckles and the posts; an axial displacement was applied to join the buckles to the posts and lock the valve to a height of 19 mm, surface-to-surface hard normal and frictionless self-contact was applied to the braids of the stent. This approach was repeated for the 5mm supra-annular (Case 2) and sub-annular positions (Case 3). The top and bottom edges of the aortic root were constrained using non-displacement boundary conditions in the longitudinal and circumferential directions. A semi-automatic mass scaling strategy with a target time increment of $1e^{-6}$ was used. The kinetic energy of the simulations was monitored to ensure that the ratio of kinetic energy to internal energy remained less than 5%, thereby ensuring that inertial forces did not affect the solution.

3.2.5 Eccentricity

Eccentric valve geometries cause leaflet distortion, which can alter leaflet kinematics and fluid mechanics [29, 139, 144]. The eccentricity of the valve stent was measured at the inflow, midplane and outflow segments of the Lotus valve stent using the Eq. 3.1 [140].

$$e = 1 - \left(\frac{D_{min}}{D_{max}} \right) \quad (\text{Eq. 3.1})$$

where D_{max} and D_{min} are the major and minor axes of the ellipse respectively and zero is the optimal eccentricity. The D_{max} and D_{min} were measured by mapping an ellipse shape onto the stent cross-section. Eccentricities were measured at the inflow, middle and outflow segments of the stent. The inflow segment is where the leaflet attachment points reside and represent the highest area of leaflet distortion.

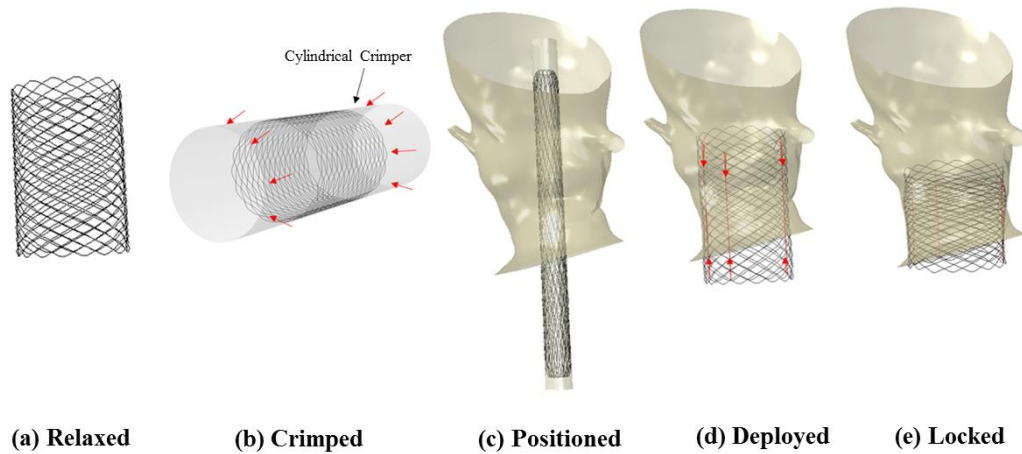


Figure 3.5: Crimping and deployment method for the valve stent. (a) The stent in its relaxed position. (b) The crimping of the stent using a cylindrical crimp that is reduced inward radially and using contact crimps the stent to a diameter of 18FR. (c) The stent in its crimped configuration positioned inside the aortic root. (d) The crimp is expanded allowing the self-expansion of the nitinol stent and deployment into the aortic root. (e) The connector elements are displaced inward to lock the stent to a height of 19 mm.

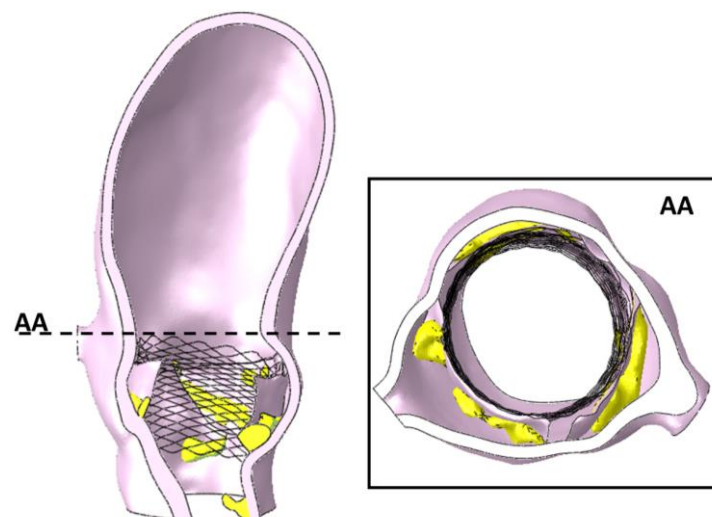


Figure 3.6: Locked Lotus™ valve post-deployment in the calcified aortic root geometry.

3.3 Results

3.3.1 Eccentricity

Figure 3.7 demonstrates images of the cross-sections from which the measurements were taken. Comparing the eccentricities at the inflow position, the location of the basal leaflet attachment, it was found that the annular position had the lowest eccentricity (0.012). The eccentricity increased to 0.018 at the 5 mm sub-annular position and 0.025 at 5 mm supra-annular (Figure 3.6). The average stent eccentricity at each of the three positions (average of inflow, middle and outflow) was found to be 0.019 for the sub-annular position, 0.012 for the annular position and 0.017 for the supra-annular position. Upon examining the average eccentricity for the three positions that the average stent eccentricity was 0.005 at the outflow position versus 0.026 at the midpoint of the stent and 0.018 at the inflow position.

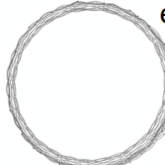
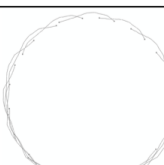
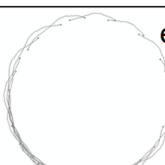
	5mm Sub	Annular	5mm Supra
Inflow	 e=0.018	 e=0.012	 e=0.025
Middle	 e=0.035	 e=0.019	 e=0.023
Outflow	 e=0.004	 e=0.031	 e=0.004

Figure 3.7: Section views of the stent eccentricity throughout the stent at the inflow, mid-plane and outflow portions of the stent for the different deployment conditions where e denotes stent eccentricity.

3.3.2 Aortic Root Peak Stress and Stress Distribution

The peak von Mises stresses in the aortic sinus following initial stent deployment were examined at the three different deployment positions. Table 3.2 shows the peak stress and 99th percentile stresses (σ_{99}) in the aortic sinus and the average stress in the sinus (σ_{avg}) and the average stress in the interleaflet triangle (σ_{avg_int}).

Table 3.2: Peak von Mises stress at different positions for the LotusTM valve stent.

(MPa)	Peak stress sinus	σ_{99} sinus	σ_{avg} sinus	σ_{avg_int}
5 mm supra-annular	1.141	0.131	0.024	0.025
Annular	1.035	0.148	0.027	0.030
5 mm sub-annular	0.892	0.126	0.027	0.031

The peak stress in the aortic sinus was found to be highest when the stent was positioned supra-annularly (1.141 MPa). The peak stress was lowest (0.892 MPa) when the stent was deployed 5 mm sub-annularly. A peak stress of 1.035 MPa was found when the stent was positioned at the 5 mm supra-annular position.

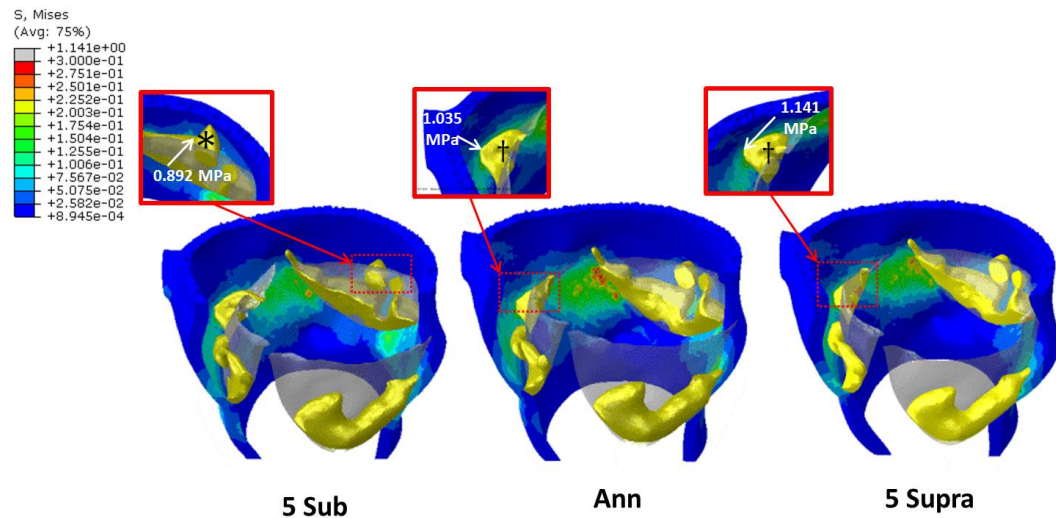


Figure 3.8: Contour plots of the peak von Mises stress and corresponding calcification. In the 5 mm sub-annular position, a peak stress of 0.892 MPa was caused by compression of the calcium deposit (indicated by *) located on the non-coronary. When the valve is implanted in the annular position, a higher peak stress was predicted (1.035 MPa) due to another piece of calcium on the right-coronary cusp (indicated by †). However, when the valve was implanted at the 5 mm supra-annular position, the stent applied a greater force to the same calcium deposit (†) leading to the highest peak stress (1.141 MPa) at the 5 mm annular position.

Figure 3.8 shows contour plots of the von Mises stress distribution throughout the aortic sinus. The contour plots show that the highest stress concentrations are located in the region where calcification is present. As the valve is implanted supra-annularly, the calcification on the right-coronary leaflet is further compressed against the wall of the aortic sinus leading to the maximum peak stress when the stent is implanted 5mm supra-annularly. Figure 3.9 shows the contour plots of the von Mises stress distribution throughout the aortic sinus, in

particular in the interleaflet triangle between the non-coronary and right-coronary sinus. It was found that as the valve is deployed at higher implantation depths the amount of stress in the interleaflet triangle reduces. The percentage volume plots in Figure 3.10 show the stress distribution throughout the interleaflet triangle for the three different positions following deployment of the Lotus valve stent. Comparing the volume of tissue above-average stress (0.025-0.031 MPa) it was found that the percentage volume of tissue under higher stress increases when the stent is implanted at the 5 mm sub-annular versus 5 mm supra-annular and annular positions.

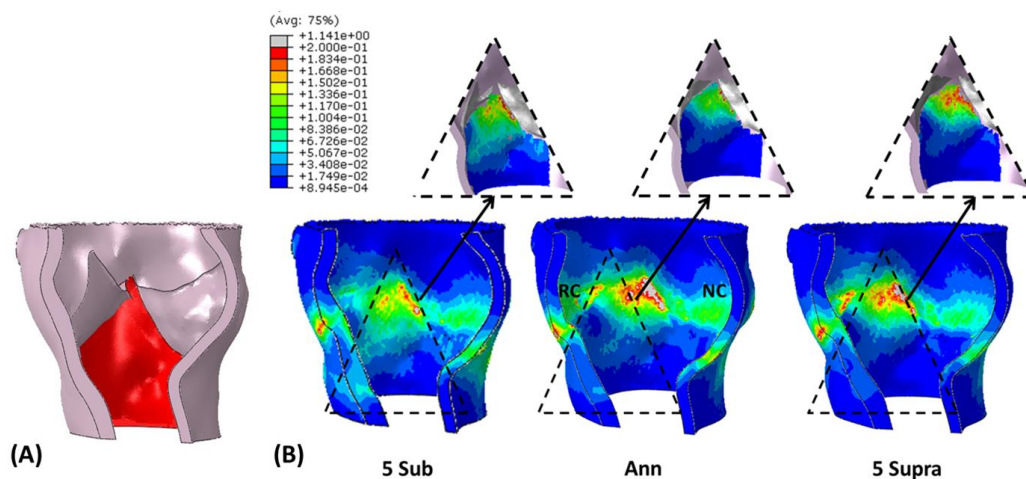


Figure 3.9: (A) The area in red defined as the interleaflet triangle between the non-coronary (NC) and right- coronary (RC) sinus (B) Contour plots of von Mises stress distribution throughout the aortic sinus and the interleaflet triangle between the non-coronary (NC) and right- coronary (RC) sinus following deployment of the LotusTM Valve stent at the different implantation positions.

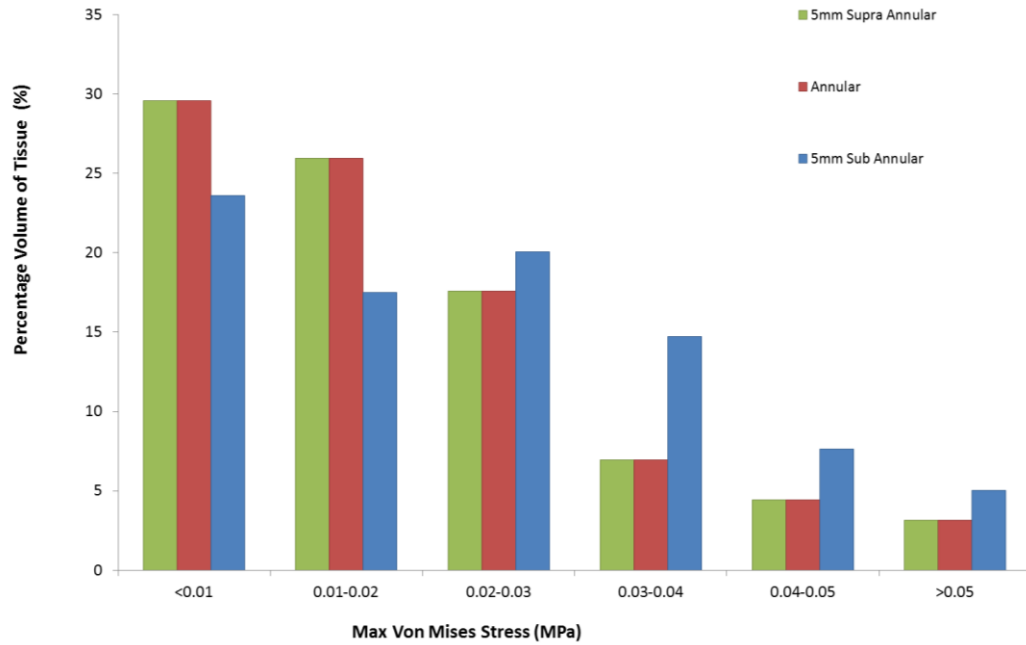


Figure 3.10: Percentage volume graph for the three different positions showing the stress distribution throughout the interleaflet triangle between the non-coronary and right- coronary sinus following deployment of the Lotus valve stent.

3.4 Discussion

In this study, FE methods were applied to examine how positioning of a Lotus valve stent determined stress distribution in a patient-specific artery, particularly focusing on the interleaflet triangle in which the bundle of His resides. The results of this study showed that TAV positioning had an influence on both the peak stresses in the aortic sinus and stent eccentricity. The results of this study also showed the potential for FE methods to predict levels of stress arising in the vicinity of the bundle of His, as a function of implantation depth. It was found that for the specific patient anatomy studied, the 5 mm sub-annular position showed the lowest peak stress of the three implantation positions; however, this position led to the highest stress concentrations in the interleaflet triangle between the non-coronary and right-coronary sinus suggesting the highest potential for conductance interferences. In contrast, the 5 mm supra-annular position predicted decreased stress in the interleaflet triangle reducing the risk of conductance interference, while this position had the highest peak arterial stress. These results provide pre-operative information that can inform clinical decision-making regarding TAVI positioning and may lead to further insight into the underlying mechanobiological mechanisms that may cause conductance abnormalities.

There are limitations to this study. Firstly, the assumption was made that the aortic root is an isotropic hyperelastic material, although the aortic root is known to be anisotropic. However, the constitutive laws used were fitted to the circumferential direction, the stiffest directions of the aortic root, and it is known that the aortic root responds to deployment of the stent predominantly in the circumferential direction. Therefore, the use of an isotropic model was considered to be appropriate for correctly capturing the stress in this model [29, 190]. Indeed,

a recent study suggests that more complex models (i.e. HGO) do not necessarily lead to more accurate results as constitutive models cannot be adopted to represent material data from a specific patient [176]. Moreover, due to limited knowledge of patient-specific aortic pressure, aortic wall pre-stress was neglected. These assumptions may lead to an increase in predictions of the deformations in the aortic sinus [30, 191]. It must also be noted that the supra-annular position would not be a target implantation position in a clinical case using the Lotus valve, as it might result in an insufficient seal in the annulus and may lead to increased PVL. However, due to the fact that this study did not model the paravalvular seal or examine PVL, this position was used to examine an extreme case of mal-positioning. Furthermore, the model did not specifically include the buckles and posts of the repositionable mechanism of the Lotus valve stent. However, the buckles and posts are located on the inner portion of the stent and thus do not directly affect stress in the aortic tissue. Finally, in this study only one patient-specific anatomy was examined, and as such the specific results regarding the relationship between implantation depth and aortic tissue stress cannot be assumed to represent the entire population. However, this is the first detailed analysis to provide an understanding of the impact of TAV positioning for stress elevation in the vicinity of the bundle of His.

The results of this study show that positioning of the stent is important for stent eccentricity with the eccentricity ranging between 0.004 and 0.035 based on variations in the position of the stent. Eccentricity is a metric commonly used to measure the level of stent distortion. Eccentricity should be taken into consideration in pre-operative planning, as eccentric stent geometries lead to leaflet distortion, altering leaflet kinematics and fluid mechanics [29, 139, 144]. However, in this

study, the eccentricities shown by the Lotus valve stent are low and the device seems to retain its circular geometry even in an eccentric aortic root. In a study investigating the positioning strategy of the CoreValve, it was found that the eccentricities ranged from 0.03 to 0.18 depending on implantation position [30]. The results of this study are in agreement with clinical results of the Lotus valve reporting average eccentricities of 0.06 ± 0.04 [140] suggest that the locking mechanism in the Lotus valve reduces stent eccentricity. Future investigation should be carried out into the potential of the locking mechanism in the Lotus valve to allow a self-expanding stent to keep a more rigid shape which may lead to the reduction in leaflet distortion while maintaining reduce volumes of PVL.

A previous study found that when the Edward SAPIEN valve was positioned at higher and lower implantation depths the maximum von Mises stresses in the aortic root wall were found to be 0.98 MPa and 0.76 MPa at the lower and higher implantation depths respectively [31]. Another study examining the implantation depth of the CoreValve found that the 99th percentile stresses (σ_{99}) in the aortic root ranged from 0.151 MPa to 0.173 MPa with a decrease in the σ_{99} in the aortic root at lower implantation depths [30]. The current study reported higher peak stress (0.892 - 1.141MPa) in the aortic sinus tissue compared to [31], but it must be noted that the model in this study included native leaflets and calcification, and as such an increase in peak stress would be expected. The current study reported 99th percentile stresses (0.126 – 0.148 MPa) in the same magnitude as [30]. It should be noted that the peak stresses predicted in the aortic root for all three positions are well below the ultimate tensile stress of the aortic sinus, which has been found to range from 2.3 to 3.1 MPa [39].

Examining the peak stress in the aortic root, it appears as though the predominant cause of the peak stress is the result of calcium being pushed against the wall of the aortic sinus (Figure 3.8). The peak stress in the 5 mm sub-annular position (0.892 MPa) was in the position of a calcium deposit (Figure 3.8) located on the non-coronary leaflet. When the valve was implanted in the annular position a higher peak stress was predicted (1.035 MPa) due to another piece of calcium on the right-coronary leaflet. However, when the valve was implanted at the 5 mm supra-annular position the stent applied a greater force to the same calcium deposit leading to the highest peak stress (1.141 MPa) at the 5 mm supra-annular position. These results would suggest that the peak stresses in the aortic sinus are dependent on the position of the valve relative to the location of calcium around the aortic root. It has previously been hypothesised that compression of calcification into the aortic root is the cause of aortic rupture in TAVI cases [133] and that calcium might be a useful predictor of aortic root rupture, and the results of this study corroborate this hypothesis.

During clinical practice, the depth of the prosthesis has been shown to be an independent predictor of persistent LBBB, with lower positioning of the valve being shown to increase the risk of conductance interference and the need for PPM in both self-expanding and balloon expandable valves [192, 193]. The results show here that, while peak stress was lowest in the sub-annular positioning, there was no considerable difference in the average stress (σ_{avg}) in the aortic sinus with a σ_{avg} of 0.027 MPa in the annular and 5 mm sub-annular positions and a σ_{avg} of 0.024 MPa in the 5mm supra-annular position (Table 3.2). For this reason, it was decided to further investigate stress in areas that have greater potential for conductance interference, particularly under the commissures of the right- and non-coronary

sinuses, the interleaflet triangle in close proximity to the bundle of His (Figure 3.9). Interestingly, examining Figure 3.8 it can be seen that the bands of higher stress move supra-annularly with higher implantation depth. Examining, the average stress in the interleaflet triangle ($\sigma_{\text{avg_int}}$) they were found to be 0.031 MPa sub-annularly, 0.03 MPa annularly and 0.025 MPa supra-annularly. The stress was further examined in this area using percentage volume plots examining the volume of tissue under different bands of stress in this area (Figure 3.10). It was predicted that when the valve is positioned supra- versus sub- annularly the percentage volume of tissue above the average stress considerably decreases in the interleaflet triangle. The results provide the first quantitative evidence in support of supra-annular positioning to reduce stress in the area where the conductance system is located. Thus, while peak stress is an indicator of aortic root rupture, it is not indicative of problems such as conductance interferences, which have been associated with damage high stress to the surrounding tissue. Further, investigations of stress in patients with and without conductance interference may lead to a greater insight into the thresholds of stress that may lead to conductance interference.

3.5 Conclusion

In this study, a FE model simulating the deployment of a Lotus valve stent into a calcified patient-specific aortic root geometry was created. This model was applied to investigate the effect of implantation depth on stress in the TAV and in the aortic root. Furthermore, the potential of the Lotus valve locking mechanism in reducing the eccentricity of the valve stent was examined. The results of this study predicted that the locking mechanism of the Lotus valve stent appears to work in reducing eccentricity maintaining circularity post-deployment. It was predicted that while calcification patterns specific to this patient lead to the highest peak stress in the supra-annular position, this position lead to the lowest stress in the interleaflet triangle in which the conductance system (Bundle of His) resides, which provides the first quantitative evidence in support of the supra-annular position as the most appropriate Lotus valve implantation position for stress reduction in the vicinity of the conductance system. These results show the potential for computational modelling techniques as a post-operative tool, providing clinicians with more informed procedural planning.

Chapter 4: An *In Vitro* Model Quantifying the Effect of Calcification on the Tissue–Stent Interaction in a Stenosed Aortic Root

4.1 Introduction

As mentioned in Chapter 2 TAVI is a minimally invasive alternative to surgical heart valves in the treatment of AS. Since the first implantation in 2002, TAVI procedures have become increasingly popular [15] in particular for patients that are too high risk for surgical heart valve replacements. TAVI has shown favourable hemodynamics and reduced hospitalization and death in such patients [110]. However, there are potential complications of TAVI implantation, including interference with the mitral valve, interference with the heart's conductance system, PVL, reduced device durability and dislodgement of the TAV into the left ventricle [19-21, 194]. The tissue-stent interaction is particularly important for the successful deployment and post-operative device performance for TAVs. It has previously been shown that excessive radial force can lead to aortic root rupture [39], whereas inadequate radial force can lead to problems such as migration of the stent into the left ventricle [45].

As previously mentioned in Section 2.5 of the thesis the biomechanical interaction between the aortic root and the valve stent has been widely investigated using a computational approach [29-31, 39-42, 45, 137, 155, 172, 173]. CFD has been applied to investigate stent migration forces and it has been reported that the antegrade force (0.602 N) is ten times smaller than the retrograde force (6.01N), and also that the

dynamic pressure gradient is the largest contributor to the migration force experienced by TAVs [45]. Similar axial force values (5.8–6.1 N) were predicted to occur under a static diastolic pressure on the leaflets of a 23 mm TAV, with eccentricities of 0.3, 0.5 and 0.68, using FEA [42]. Numerical analysis has been applied to investigate the force exerted by different TAVI designs on the annulus and it has been shown that the hoop forces of the 26 mm CoreValve vary from 2-7 N, for aortic annuli ranging from 20–23 mm and that the 26 mm Edwards SAPIEN has a hoop force of 12-14 N when deployed in a 22 mm aortic annulus of varying stiffness [137]. The tissue-stent interaction has been quantified experimentally *in vitro* using ovine and porcine aortic roots by measuring the radial expansion force of the stent, the associated annulus deformation, the axial stent pullout force and the coefficient of friction [46]. It was reported that the radial force increased by 30-40 % when crimped at body temperature versus room temperature, the coefficient of friction between the stent and aortic root was found to be 0.10 ± 0.01 and that a minimum dilation of the aortic root of 2.5 mm caused by a radial expansion force of 60 N was required to prevent the stent dislodging into the left ventricle [46]. However, these studies did not incorporate leaflet calcification or calcification of the stenotic aortic root and so the impact of calcification on the biomechanical interaction was not taken into account.

The degree of aortic calcification has clinically been shown to predict PVL, aortic regurgitation and procedural complications [195-197]. Recent computational studies have included calcification when investigating the tissue-stent interaction [30, 39, 40, 172-174]. A FE model of a patient-specific stenotic aortic valve was developed to investigate the biomechanical interaction between a TAVI stent and the tissue, and

it was reported that calcium deposits elevated stress during TAV stent deployment with peak stresses and strains observed in the calcified regions. These results suggest that calcification helps secure the stent in position [40]. Using a patient-specific FE modelling approach Russ *et al.* examined stent deformation when calcification was present versus excluded from the model. The results were then compared to post-operative data of Corevalve stent deformation. The model demonstrated the importance of calcification in the dynamics of stent expansion and the tissue interaction, particularly the quantitative prediction of tissue stress [174]. It has also been shown that stent deformation known as “dog-boning”, whereby the stent exhibits larger expansion at distal portions, is dependent on specific calcification patterns, and leads to localised gaps between the stent and tissue, and higher stress in the region of the calcifications [172]. These studies highlight the need to understand the role of calcification for the tissue-stent interaction of TAVs. However, there is a lack of experimental data to validate these models.

In this chapter, the hypothesis (hypothesis 2) that “*Calcification secures the TAV in place by increasing the friction in the interaction between the TAV stent and a stenosed aortic root*” is tested. The objective of this study is to develop a calcified *in vitro* model using artificially calcified porcine aortic roots to investigate the effect of leaflet calcification on the tissue-stent interaction and its role in securing the stent in the aortic root.

4.2 Materials and methods

4.2.1 Stent Radial Expansion Experiment

A 0.0225” nitinol wire was used to create a braided stent, with 4 axial and 11 circumferential cells, of 27 mm diameter and height 14 mm (Figure 4.1). The stent was made and annealed at 500°C for 30 minutes. It must be noted that this stent is not a Lotus Valve stent and has different properties to the mechanically expandable Lotus Valve. Based on a previously developed technique [46], a stent crimp experiment was performed on the nitinol braided stent. This was performed by wrapping a vinyl strap around the stent. The strap was mounted onto a uniaxial testing apparatus with one end clamped and fastened between two stainless steel plates, and a narrow slit allowed the strap to be pulled and clamped evenly at the opposite end (Figure 4.2). The fixture displacement was used to measure the stent diameter. The hoop force exerted from the strap was measured by a load cell that was attached to a uniaxial machine. The experiments were conducted at 37°C.



Figure 4.1: (a) Braiding of the stent on a mandrel (b) finished stent geometry.

The hoop force was then used to calculate the radial expansion force using the equation [3]:

$$F_{radial} = 2 \cdot \pi F_{hoop} \quad \text{Eq.4.1}$$

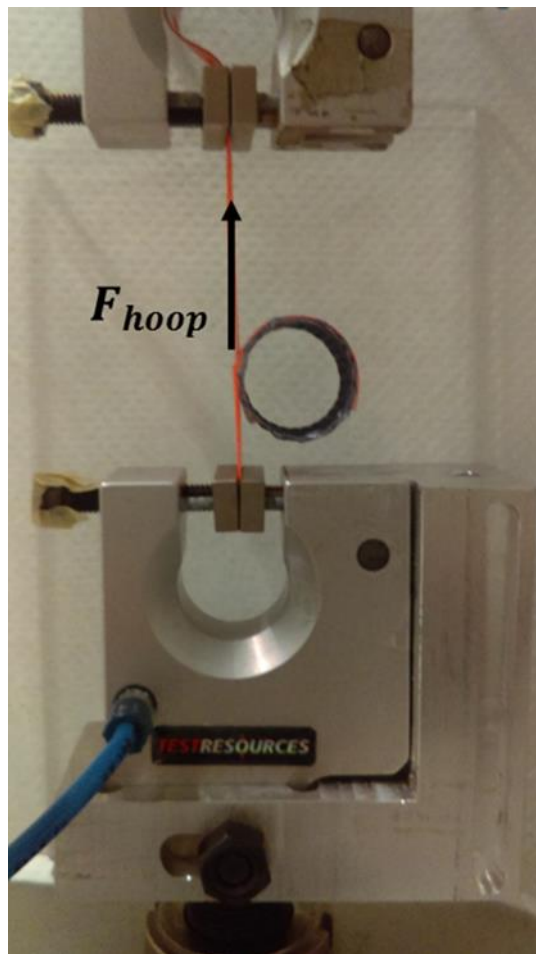


Figure 4.2: *Radial Force Test Set Up.*

4.2.2 Root – Stent Interaction Experiment

Artificial calcifications were created using methods adapted from Wendt *et al.* [198]. Commercially available reagents with similar properties to native calcifications were used to make a solution from bone glue (collagen) (Liberon Limited, UK) mixed with water (1:7) and then dissolved, 0.25 g hydroxyl-apatite (Fisher Scientific Company LLC, USA) and 1.75 g calcium carbonate (Fisher Scientific Company LLC, USA). The mixture was dried for 48 hours and then fragmented using a scissors, scalpel and by hand. The calcification was first shattered into different sized pieces, which were then weighed and based on the weight the calcification was further cut to the correct weight using a scalpel or scissors to create small equally sized pieces. Using micro-Computed Tomography (μ CT) (μ CT100, Scanco) evaluations were performed on the calcifications created in this study and they were found to have Hounsfield Units (HU) of 535+, which is within in the range of that of *in vivo* calcifications [199].

Porcine hearts were obtained fresh and stored in a -80° C freezer. Prior to carrying out the experiment, each heart was stored at room temperature for 20 minutes before being placed in a 37° C water bath until the heart had defrosted [46]. The annulus size of the heart was then measured using an aortic sizer (Medtronic PLC). Using the Agatston scoring method, it was determined that 300 mm^3 of calcification would represent a severe case of calcification. This 300 mm^3 of calcification was attached using cyanoacrylate glue to the leaflets of the aortic valve of porcine hearts with 19 mm diameter aortic annuli (n=4) (Figure 4.3). A control group of hearts with 19 mm diameter aortic annuli (n=3) were used without the addition of calcifications.

The hearts were then submerged in a 37°C phosphate buffer saline solution for the duration of the experiment.



Figure 4.3: (a) Uncalcified and (b) calcified porcine aortic valve.

For both the calcified and non-calcified groups the specimens were subjected to preconditioning using a valvuloplasty balloon (BARD Peripheral Vascular, Inc., Tempe, AZ) 1 mm larger than the initial diameter for 10 cycles. The stent was then implanted into the aortic root by hand by stretching the stent into a crimped position and then releasing once the valve was implanted so that an equal distribution of the stent was above and below the annulus. The stent was then post dilated using a 26 mm balloon to its original 27 mm diameter to ensure that the stent experienced recoiled and was under the same loading conditions as the radial force test [46], i.e. in compression. Evaluations were performed using μ CT (μ CT100, Scanco) at a resolution of 36.8 μ m. Dicom images were exported to Mimics 14.1 Imaging Software (Materialise, Leuven, Belgium) allowing for 3D reconstruction of the stent geometry. Using this reconstructed geometry the dimensions of the stent at the top, middle and

bottom were measured (Figure 4.4). The eccentricity of the valve stent was measured using the equation [140]:

$$e = 1 - \frac{D_{min}}{D_{max}} \quad \text{Eq.4.2}$$

where D_{max} and D_{min} are the major and minor axes of the ellipse respectively and zero is the optimal eccentricity. The radial force was calculated using the final diameter of the stent and the experimental data.

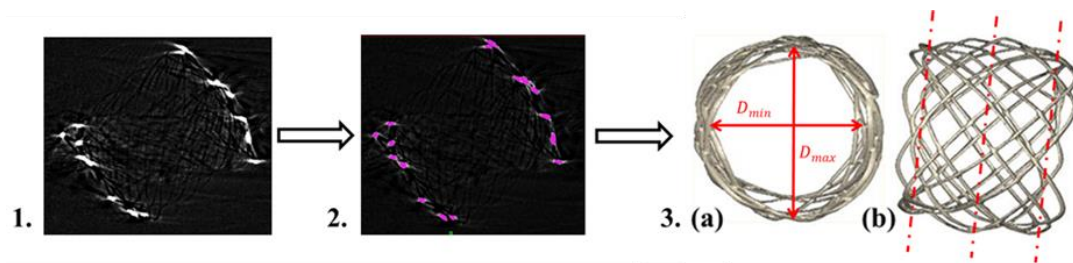


Figure 4.4: Creation of the stent geometry from (a) the MSCT scan of the stent, (b) depicts segmentation of the stent using Mimics 14.1 to threshold the MSCT scans, and (c) reconstruction of the stent post-deployment in the calcified porcine aortic root, measurements were taking of the maximum and minimum diameters at the top, middle and bottom of the stent.

The pullout force of the stent was measured. This was done by dissecting off the apex of the heart and attaching stiff strings to the end of the stent and to a uniaxial test machine. A constant speed of 20 mm min^{-1} was applied to pull the stent in the direction of the apex (Figure 4.5). The pullout force required to pull out the stent was then measured. Using Amontons Coulombs friction law [46, 200], the pullout force ($F_{pullout}$) can be defined by:

$$F_{pullout} = \mu F_{radial} \quad \text{Eq. 4.3}$$

where μ is the coefficient of friction between the stent and the aortic root and F_{radial} is the radial force exerted by the stent on the aortic root. Using the equation for the *in vivo* pull out force [46]:

$$F_{invivo} = \Delta P_{stent} \pi \left(\frac{d}{2} \right)_{stent}^2 \quad \text{Eq. 4.4}$$

it can be determined whether the stent would migrate into the left ventricle at physiological pressure if the stents $F_{pullout}$ is less than the F_{invivo} [46].

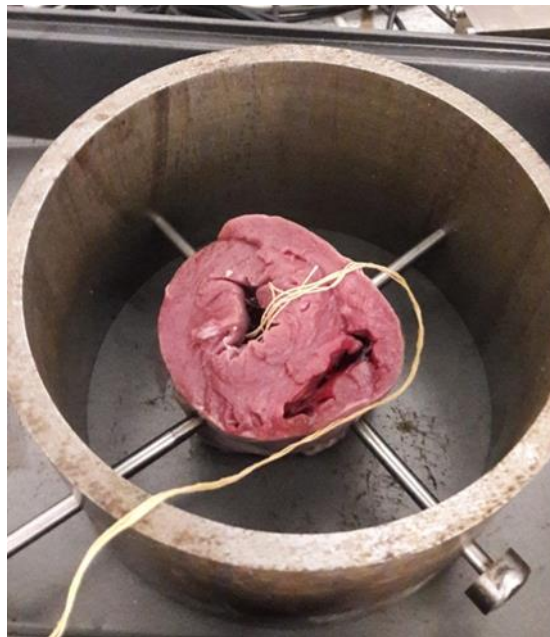


Figure 4.5: Porcine heart with apex dissected and pinned in place prior to the pullout test.

4.2.3 Statistical Analysis

Data were analysed using (GraphPad Prism, GraphPad Software, La Jolla California USA). Two-tailed Student's t-tests were used to determine statistical differences between the non-calcified and calcified groups for eccentricity, radial force, pull-out force and coefficient of friction. Statistical significance was defined as $p \leq 0.05$.

4.3 Results

4.3.1 Radial Force

The radial force test was performed at 37°C, the radial force test data illustrated in Figure 4.6 shows the radial force versus diameter for the given braided stent geometry. It was found that crimping the stent from a diameter of 27 mm to a diameter of 20 mm led to an approximate increase of 55 N in the radial force exerted by the stent.

The maximum diameters measured from the stent when deployed into the non-calcified porcine aortic roots were found to be in the range of 23.38 ± 1.11 mm, with minimum diameters equal to 22.82 ± 1.37 mm. This can be compared to maximum and minimum diameters of 24.39 ± 0.91 mm and 23.11 ± 1.20 mm respectively measured from the stent when it was deployed in the calcified porcine aortic roots. This gave average diameters of 23.10 ± 1.05 mm (non-calcified group) and 23.75 ± 1.24 mm (calcified group). There was no significant difference found in the diameter of the stents between the two groups ($p=0.51$).

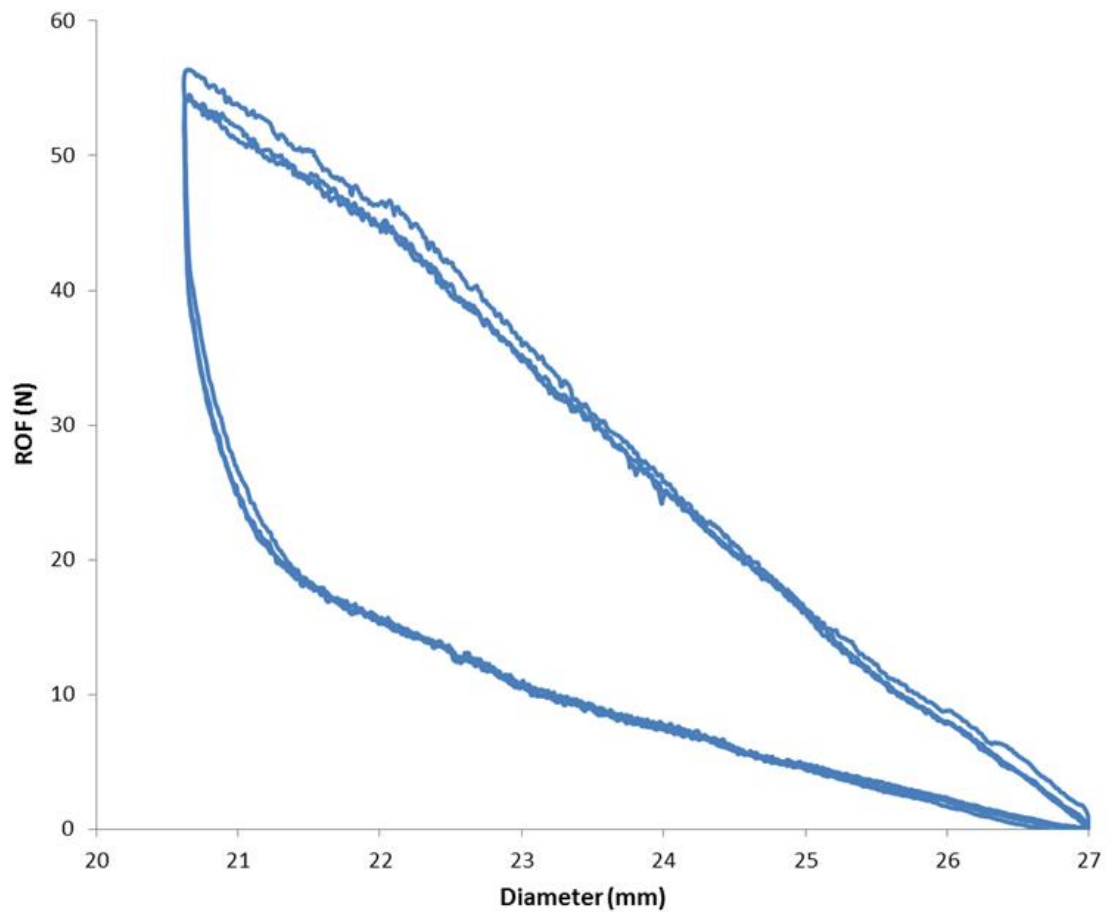


Figure 4.6: Radial outward force (N) versus diameter (mm) for the stent.

The radial force data was extrapolated from Figure 4.6, based on the average diameter of the stent. It was found that the radial force exerted on the aortic root ranged from 19.31–38.79 N in the non-calcified hearts versus 13.20–38.36 N for the calcified hearts. No statistical difference was found in the radial force of both groups with the radial force averaging 32.71 ± 11.62 N for the non-calcified and 26.85 ± 11.08 N for the calcified group ($p=0.53$).

4.3.2 Stent Eccentricity

Stent eccentricity was measured using Eq. 4.2 from the maximum and minimum diameters of the stent. It was found that the eccentricity of the stent ranged from 0.01-

0.037 in the non-calcified roots. This compared to eccentricities of 0.034-0.067 for the calcified roots. There was found to be a significant difference ($p=0.049$) in the eccentricities between the two groups, whereby the eccentricity in the stent when calcification was present (0.053 ± 0.015) was significantly greater than that without calcification (0.024 ± 0.014).

4.3.3 Pullout Test and Friction Coefficient

The average stent pullout force was 2.84 ± 1.55 N for the non-calcified roots, which compared to a stent pullout force of 8.58 ± 3.68 N for the calcified roots. There was a significant increase in the force required to dislodge the stent in the calcified group when compared to the non-calcified group ($p=0.045$). The coefficient of friction was calculated using Eq. 4.3 and found to be 0.09 ± 0.05 (non-calcified) and 0.36 ± 0.12 (calcified). The presence of calcification led to a significant increase in the coefficient of friction between the stent and the aortic root ($p=0.018$).

The predicted *in vivo* pullout force was calculated using Eq. 4.4, this represents the maximum force predicted to be acting on the valve stent *in vivo*. A physiological pressure gradient of 100 mmHg was used to represent a patient with stage 2 hypertension and thus represent a ‘worst case scenario’ criteria [46] and the maximum diameter of the stent were used in calculating the max force acting on the stent *in vivo*. It was found that $F_{in vivo}$ was calculated as 5.72 N for the non-calcified root whereas this was 6.23 N for the calcified aortic root.

4.4 Discussion

This study developed an *in vitro* experimental model to represent a calcified aortic root and applied this model to determine the pullout and radial expansion forces of a TAV stent, and the coefficient of friction between the stent and aortic root. It was found that, in the presence of calcification, the coefficient of friction was significantly increased (0.36 ± 0.12) compared to that of non-calcified valves (0.09 ± 0.05). This increase in friction leads to an increase in the pullout force required to dislodge the stent. While it has been previously proposed that calcification helps to secure the TAV stent in position [15], this study provides the first quantitative experimental data to provide evidence in support of this role of calcification in the tissue-stent interaction. Furthermore, it has been reported that the range of stent eccentricities increased (0.03-0.07) in calcified roots, compared to that of non-calcified roots (0.01-0.04). Moreover, it has been reported that in the presence of calcification the pullout force required to dislodge the stent was higher than the predicted *in vivo* force, which implies that the stent would be unlikely to migrate into the left ventricle *in vivo*.

It must be taken into account that both calcifications and arterial stiffness have an impact on the tissue-stent interaction [137, 174]. In this study only the effect of calcification has been examined; however, stiffening of the tissue due to age was not included in the scope of this study. It must also be noted that calcification can cause tissue degradation and disrupt the structural integrity of the tissue matrix in the surrounding regions. However, tissue alteration due to calcification and disease progression was not included in this study. Nevertheless, the focus of this study is to examine the impact of calcification on the tissue stent interaction. Therefore, the tests

are carried out only changing the attachment of calcification to the valve. Throughout this study the authors refer to the coefficient of friction as the ratio between the pullout and the radial force, this relationship was previously defined in the study of Mummert *et al.* [46]. However, it must be noted that in the presence of calcification this relationship is somewhat simplified as any “hooking” of calcification between the stent cells is also included in this interaction. Nevertheless, this is the first study to approximate the impact of calcification on the coefficient of friction and demonstrate the role of calcification in securing the valve in place. It was also assumed that the glue does not interact with the stent but only serves to hold the calcification in place on the tissue. The lack of material properties available in literature restricts comparison of the *in vitro* experimental calcification model to properties of physiological calcification. However, by μ CT analysis, the density of the artificial calcification was within in the range of Hounsfield units of aortic calcification and as such was considered appropriate for the purposes of this study. Furthermore, there was some variation in the shape and size of calcifications applied to the leaflets and only one volume of calcification was tested in this study. However, these were evenly distributed across the leaflets and the total volume of calcification was kept constant. It must also be considered that this is a static analysis, which did not account for the dynamic motion of the aortic root, and tissue remodelling or growth was not considered. As the radial expansion force was determined experimentally it was assumed that the tissue responses were passive material properties [46]. Further to this, it must be noted that the radial force can only be approximated, particularly in eccentric deployment conditions. For this reason, the minimum and maximum

diameter along three different sections of the stent were taken with the goal of getting an approximation of the average radial force acting across the stent as a whole. It must be noted that a similar method was used in determining the force exerted by the stent in the previous quantification of the tissue stent interaction [46] and radial force testing is an ISO standard test that is required to be carried out on all vascular stents and does not take into account eccentricity. Human tissue was not used in this study due to limited availability and porcine hearts may not be representative of human tissue. It must be noted that a commercial stent was not used in this study. Moreover, in this study, the stent was used as a gauge to measure radial force, following a previous approach [46] and it must be noted, that once the valve stent is fully expanded, there will be no further increase in diameter or associated radial force. However, in this study the stent was not fully expanded in any of the cases and the radial forces recorded across both groups (29.36 ± 10.78 N) were within the range predicted by computational modelling of the commercial self-expanding CoreValve stent (12.6-44 N in aortic annuli ranging from 20–23 mm)[137].

It was found that the average stent diameter did not significantly differ between the two groups, which suggests that the stent diameter may be more strongly influenced by the geometry of the aortic root. However, there was a significant increase in eccentricity in the calcified group. Interestingly, clinically it has been shown that valves may exhibit higher eccentricities in higher calcified roots [141, 201].

The results of the study found that the coefficient of friction in a non-calcified root to be 0.09 ± 0.05 , with stent eccentricities ranging from 0.01-0.04 N. This is in agreement with previously reported findings of a coefficient of friction of 0.1 ± 0.01 and eccentricities of (0-0.03) in a study examining the tissue-stent interaction in a non-calcified root [46]. It has been reported for the first time that in the presence of calcification the coefficient of friction significantly increases ($p=0.02$), while, also verifying that calcification significantly increases the stent eccentricity ($p=0.049$). The increase in friction (0.36 ± 0.12) due to the presence of calcification led to a significant increase in the pullout force ($p=0.045$), which suggest that the stent was more secure in the presence of calcification. Comparing the pullout force to the predicted *in vivo* pullout force it was found that an average pullout force of 2.84 N was required to dislodge the stent in the non-calcified root where the maximum force acting to dislodge the stent *in vivo* was predicted as 5.72 N suggesting the stent would dislodge under *in vivo* conditions. This compares to an average pullout force of 8.59 N for the calcified root where the max force acting on the stent *in vivo* was calculated as 6.23 N. This suggests that the stent would not dislodge *in vivo* in the presence of calcification. Both $F_{in vivo}$ forces are in close agreement with the range of axial forces previously predicted computationally to act on the TAV *in vivo* (5.8–6.1 N) [42]. The results of this study suggest that the stent is more secure within the aortic root in the presence of calcification. These results are in agreement with a study by Cribier *et al.*, which reported that TAV stents deployed in non-calcified roots are associated with early migration and it was proposed that this migration arose due to the lack of calcification securing the valve in place [15]. An increase in pullout force can be

explained by an increase in the radial force and/or an increase in the coefficient of friction (Eq. 4.3). As there was no statistical difference in the radial force of both groups, it is proposed that the valve stent is secured in place due to the increase in friction between the stent and the aortic root. Although there was a change in eccentricity, there was no significant difference in the average diameter between the calcified and non-calcified cases. Thus, it is deduced that the diameter of the stent is predominantly affected by the diameter of the aortic root and the amount of aortic root recoil. This lack of change in average diameter would explain the fact that no significant increase is observed in the radial force between the two groups. However, it must be noted that *in vivo* the stiffening of the tissue in the aortic root due to age may lead to a lower degree of recoil of the aortic tissue, smaller stent diameters and an increased radial force compared to that of healthy tissue. The results reported here provided an important insight into the role of the friction provided by calcification nodules for preventing stent migration.

It has previously been shown that the presence of calcification can lead to aortic root rupture, and there is at higher risk in patients with more highly calcified roots [141, 201]. However, the role of calcification in securing the stent in place, particularly in patients with higher levels of calcification must be considered. The results of this study show that the ability of calcification to anchor the stent allows for a lower radial force required to secure the stent in place, which can thereby reduce the risk of rupture. This should be further considered with regard to patient-specific sizing and stent design. Further to this, the impact of a higher coefficient of friction in FE modelling

and its impact on the biomechanical response is something that should be further investigated.

In conclusion, this study outlines the development of the first *in vitro* model of aortic calcification and has shown that calcification significantly impacts the friction between the aortic tissue and TAV stent, the force required to dislodge the stent and stent eccentricity. This study demonstrates for the first time the impact of calcification on the friction between the aortic tissue and TAV stent, which shows that calcification, secures the stent in place in the aortic root. The impact of calcification should be given further consideration in TAVI procedures, as although higher levels of calcification increase the likelihood of aortic root rupture whereas there is a lesser need for higher radial forces to secure the stent in place. The impact of calcification and the degree of calcification of a given patient is something that should be further considered in device selection and design. Further to this, the coefficient of friction should be carefully considered in future biomechanical models of deployment of the TAV into an aortic root including the native calcified leaflets.

Chapter 5: The Relationship between Lotus Valve Stent Orientation and New On-Set Left Bundle Block Branch

5.1 Introduction

Although TAVI has shown success rates ranging from 74% - 100% [202, 203], there are still many complications associated with the procedure. One such complication is conduction disorders, whereby, during TAVI implantation interference with the heart's conduction system occurs leading to, in some cases, the need for PPM. The need for PPM can vary between 5.7%-39% depending on the type of valve used [48]. The conduction system, specifically the bundle of His, is in close proximity with the aortic valve complex at the interleaflet triangle between the right- and non-coronary sinuses [32, 33]. This location has been shown to be highly susceptible to direct trauma, compression and ischemia during TAV deployment [204, 205]. It has been proposed that elevated tissue stresses can trigger an inflammatory response, particularly in this region close to the heart's conduction system and can lead to a risk of conduction interference [176, 180].

In a study investigating the predictors of the requirement for PPM with the self-expanding CoreValve prosthesis, it was found that LBBB was the most common conduction disorder, with an incidence of 50.3% at discharge [48]. Incidences of new-onset LBBB have been reported to be between 8-30% for balloon expandable valves and 25-85% for the self-expanding CoreValve [47]. During clinical practice,

the depth of the prosthesis has been shown to be an independent predictor of persistent LBBB, with lower positioning of the valve predicted to increase the risk of conductance interference and the need for PPM in both self-expanding and balloon expandable valves [192, 193]. For this reason, it has been proposed that the long skirt of the CoreValve directly interferes with the conductance pathway and thus leads to the increased incidence of LBBB when compared to the Edwards SAPIEN [64]. TAVI-induced LBBB is an independent indicator of mortality with all-cause mortality shown to be 37.8% in patients with new LBBB post-TAVI versus 24.0% in patients without LBBB [49]. However, there is limited knowledge regarding the precise cause of post-TAVI conductance interference and the stresses that may be related to it [204].

Patient-specific FE models of the aortic root have been used to investigate the underlying biomechanical changes arising after TAV implantation and how these are associated with a wide range of procedural complications such as aortic root rupture, PVL, coronary occlusion, asymmetric expansion, leaflet stresses and poor hemodynamic performance [29, 39-43]. Such models can predict levels of stress and examine tissue interactions that cannot be assessed *in vivo*. A recent study investigated the role of contact pressure on the membranous septum in the development of new conduction abnormalities after TAVI using a computational approach. TAV deployment was simulated for 112 patients who had undergone TAVI with the CoreValve/Evolut R (55% of patients had developed LBBB or AV block during the TAVI procedure). Preoperative MSCT scans were segmented for each patient and deployment of the CoreValve/Evolut R was simulated. The results of this study predicted that maximum contact pressure greater than 0.39 MPa and contact pressure index greater than 14% are predictors of conductance abnormalities [44]. This study

also investigated the impact of rotating the stent 6° and 12° and reported that these rotations had no significant difference in terms of contact pressure and contact pressure index. However, this study did not investigate the Lotus valve, which differs in design from the CoreValve and the Evolut R due to the presence of stiff valve locking posts. Indeed, 55.2% of Lotus valve patients experience new onset-LBBB [51], but whether this relates to elevated tissue stresses in the tissue closest to the heart's conductance system is not yet known. It is likely that rotation of these posts can influence stress distribution in the vicinity of the bundle of His and reduce the incidence of conductance abnormalities, but this has never been investigated.

Chapter 3 of this thesis provided the first quantitative evidence in support of supra-annular positioning for stress reduction in the vicinity of the conductance system. However, this study was performed in the absence of any clinical patient data post-TAVI procedure. Furthermore, the modelling approach assumed that the coefficient of friction was 0.1, based on previously published studies [46], and did not account for the change in tissue-stent interaction in the presence of leaflet calcification, which Chapter 4 elucidated. In this chapter, the results and modelling techniques developed in Chapter 3 are expanded upon and combined with the insight gained on the impact of calcification on the tissue-stent interaction in Chapter 4 to create a modelling technique to more precisely represent clinical conditions.

In this chapter, the objective is to test hypothesis 3 that “*Orientation of the Lotus valve impacts the stress in the vicinity of the bundle of His and can induce conductance interference*” is tested. The objective of this research is to apply a patient-specific FE modelling technique to compare the biomechanical interaction in two patients; one who demonstrated post-TAVI new-onset LBBB and one who

demonstrated no symptoms of conductance issues after TAVI deployment of a Lotus valve. The levels of stress in the interleaflet triangle where the bundle of His resides are compared in the two patients. Finally, different rotational deployment positions of the Lotus valve stent were examined to investigate the impact of stent orientation on stress distribution in the vicinity of the bundle of His.

5.2 Materials and Methods

5.2.1 Aortic Root Model

Two patient-specific aortic root geometries of an 88-year old female patient who experienced new-onset LBBB post-TAVI and an 81-year old female patient who showed no symptoms of new-onset LBBB were reconstructed from MSCT images with slice thickness of 0.750 mm, slice dimensions of 512 x 512 and pixel spacing of 0.5 mm.

Mimics 14.1 Imaging Software (Materialise, Leuven, Belgium) was used to threshold the leaflets, calcifications, and aortic root (aortic sinus and ascending aorta) from the images. 3 Matic (Materialise, Leuven, Belgium) and TetGen (WIAS, Berlin, Germany) were used to generate volume meshes of the aortic root and calcifications using 3D continuum elements (4-noded tetrahedral elements with reduced integration (C3D4R)). The leaflets were meshed using shell elements with a thickness of 0.5 mm [31]. The geometries were then imported into Abaqus Explicit 6.13 (SIMULIA, Providence, RI). An assembly was then generated matching the corresponding nodal positions of the intersecting surfaces.

5.2.2 LotusTM Valve Model

The Lotus valve stent model used in this chapter is the same stent model that was previously described in Chapter 3 of this thesis. Briefly, the stent geometry was

imported into Abaqus 6.13 as a wire part and meshed using 3-noded quadratic beam elements (B32). The overlap between the braids was modelled using spring connector elements.

5.2.3 *Constitutive Models*

The constitutive models for the Lotus valve stent, the ascending aorta and the aortic sinus are as described in Section 3.2.3 of the thesis and are summarised here briefly.

The Lotus valve stent was modelled using a superelastic material model. An Abaqus 6.13 inbuilt user subroutine (VUMAT), based on the Auricchio and Taylor model, was used in assigning the superelastic properties [181, 182] Using similar methods to those outlined by Tzamtzis *et al.* a numerical model was correlated to the experimental crush test of a nitinol Lotus valve stent [137].

The ascending aorta and the aortic sinus were modelled as isotropic hyperelastic material using the same methods as Chapter 3 using the first order Ogden model fitted to uniaxial test data of human tissue [40, 184]. An isotropic hyperelastic material model was used by fitting the first order Ogden model as in Chapter 3. The aortic valve leaflets were modelled as linear elastic with Young's modulus of 1.6 MPa, a Poisson's ratio of 0.495 and a density of 1140 kg/m³ [40, 194]. The calcification was modelled as a linear elastic material with Young's modulus 10 MPa, Poisson's ratio of 0.35 and a density of 2000 kg/m³ [30, 176].

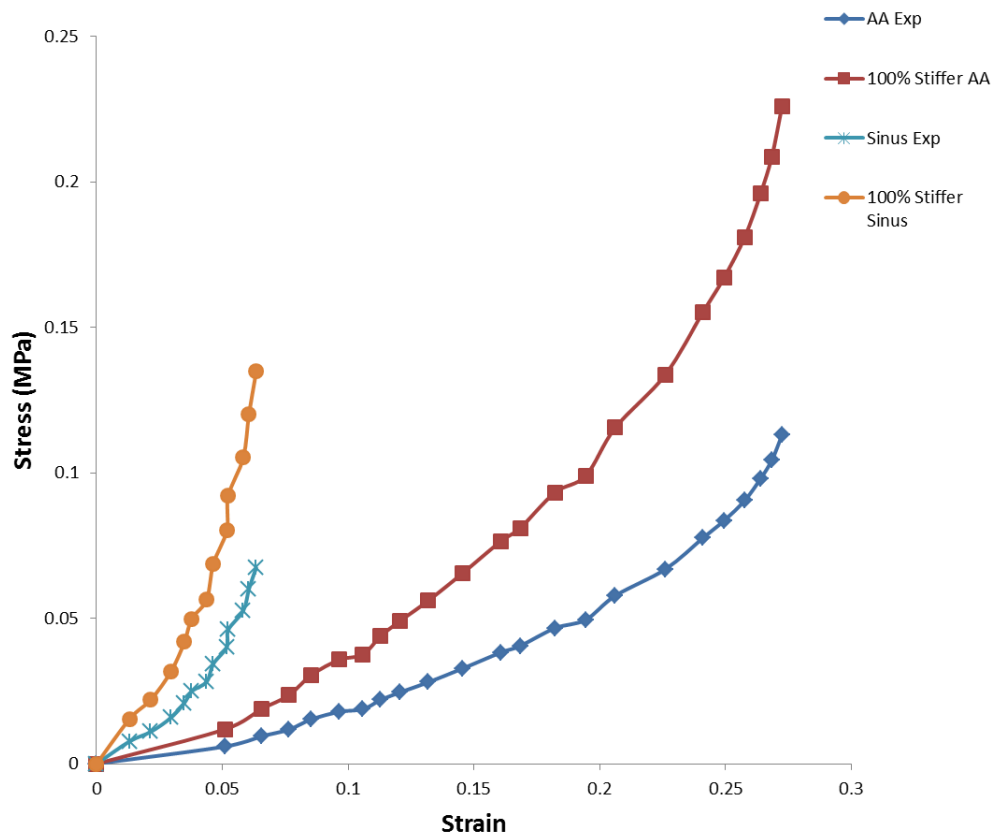


Figure 5.1: Experimental data versus 100% increase in stiffness for the stress-strain response of the human aortic sinus and ascending aorta.

5.2.4 Boundary and Loading Conditions

The crimping and deployment of the stent were modelled in Abaqus Explicit 6.13 (SIMULIA, Providence, RI). The crimping of the stent was performed using the same methods outlined in Section 3.2.4 of this thesis. Briefly, a cylindrical part (crimper) was displaced inward radially and zero friction contact was assigned to the interaction between the crimper and the stent. However, in this study, instead of deploying the stent using an uncrimping step, the model was modified to include unsheathing of the valve stent to allow for a more realistic model of deployment (Fig 5.2). The angle and position of the crimper were measured from angiograms of each patient's case and were mimicked in the model to ensure the conditions were as closely representative of

the surgical technique as possible. The stent was deployed into the aortic root by simulating unsheathing of the valve by applying an axial displacement to the crimp. The crimper was restrained radially and tangentially to prevent sliding and a zero-friction interaction between the stent and crimper was maintained. During stent deployment, a coefficient of friction of 0.36 was used between the TAV stent (master) and the calcified leaflets (slave), based on the results of Chapter 4, and the interaction between the stent and the aortic sinus was modelled using a coefficient of friction of 0.1 [46]. A third loading step was applied to the stent to simulate locking of the device using six connector elements, wherein three connectors represented the posts of the Lotus valve stent and three connectors represented the string ties. The posts and ties were displaced inward to ensure the valve was locked to a height of 19 mm.

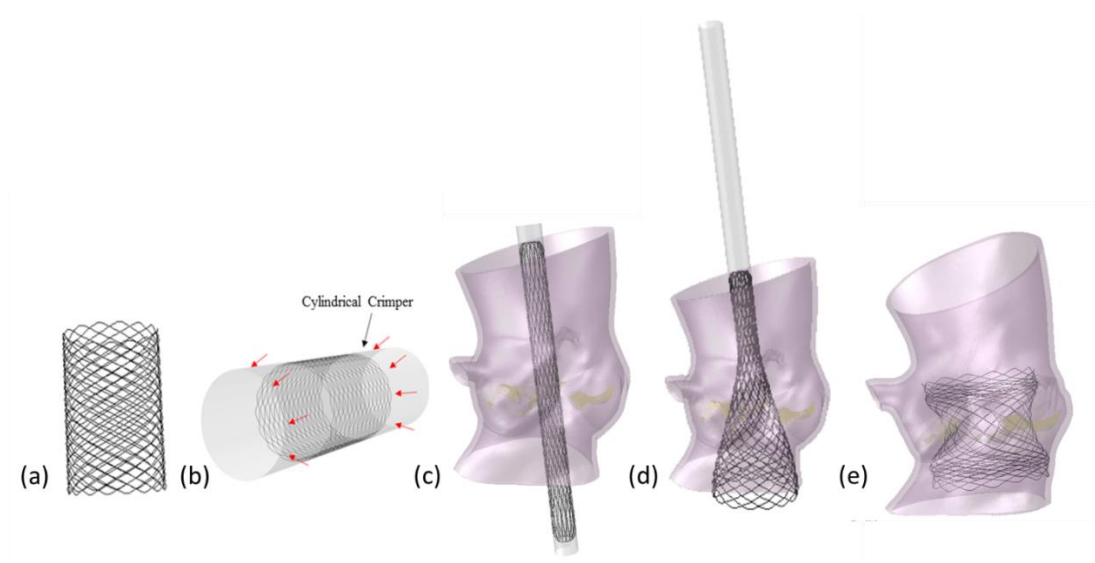


Figure 5.2: Schematic depicting the stent (a) in a relaxed configuration (b) prior to crimping (c) in a crimp configuration in the aortic root (d) unsheathing into the aortic root and (e) in a locked configuration.

Both stents were deployed in the aortic root positioned to closely replicate the real-life case. Then the stents were rotated by angles of 40° and 80° (Figure 5.3). The top and bottom edges of the aortic root were constrained using non-displacement boundary conditions in the longitudinal and circumferential directions. The kinetic energy of the simulations was monitored to ensure that the ratio of kinetic energy to internal energy remained less than 5%.

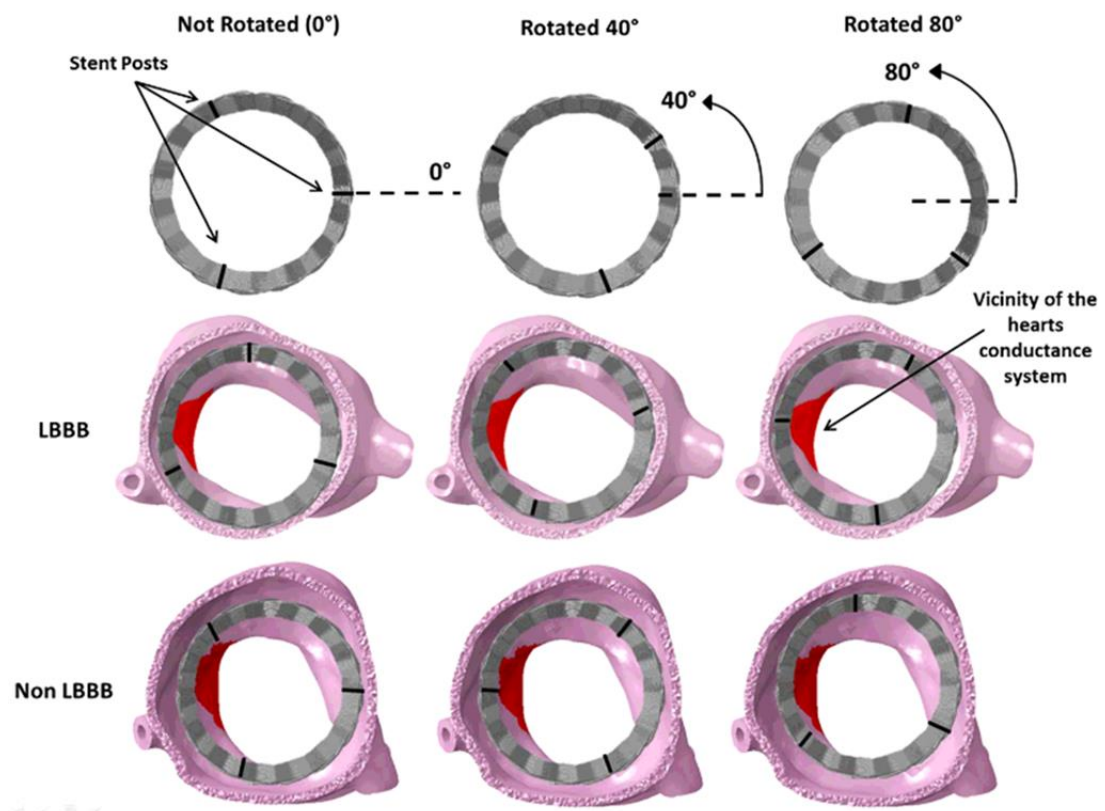


Figure 5.3: Schematic of the stent at different orientations (0° , 40° , 80°), and their initial deployment positions in the LBBB and Non-LBBB patients. The valve posts are highlighted in black and the interleaflet triangle in close proximity to the heart's conduction system is highlighted in red.

5.3 Results

5.3.1 Model validation

Quantitative comparisons of the deployment geometry were compared to real life patient angiograms of the Non-LBBB patient to validate the modelling techniques used. The geometry of TAVI *in vivo* was obtained from 2D angiograms allowing only one plane for comparison. This was accounted for by matching the plane at which the dimensions were measured in the model to plane of the angiogram, which can be clearly defined to ensure that the same dimensions were being measured from both stents allowing for a reliable comparison. Measurements of the diameter were taken at 3 planes along the stent, which were found to be most distinctive in representing the geometry. These measurements, see Figure 5.5 and Table 5.1, show the correlation between the predicted geometry and the patient real-life case deployment results, with percentage errors averaging <4%. Figure 5.5 demonstrates the ability of the model to accurately represent the bunching of the Lotus Valves braided stent, the image shows that the model accurately represents the Lotus valves “hourglass” waist. The inflow segment of the stent is most significant in terms of eccentricity as this is where the leaflet attachment points reside and represent the highest area of leaflet distortion.

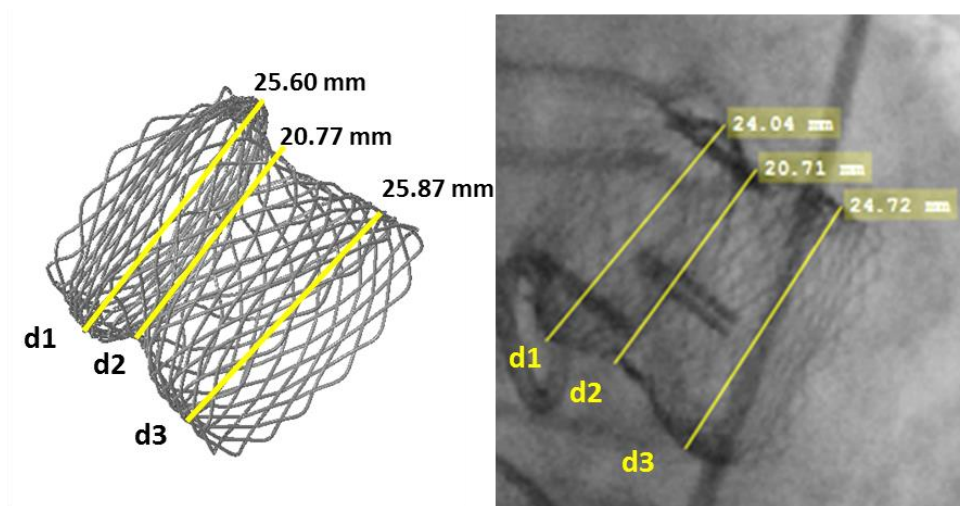


Figure 5.4: Comparison of the model stent geometry with that of post-deployment angiogram from the clinical case. d1, d2, and d3 are the diameters at plane 1, 2 and 3 respectively.

Table 5.1: Comparison of model stent dimensions with that of post-deployment angiogram from the real-life case.

	Model	Angio	Percentage
	Dimensions (mm)	Dimensions (mm)	Difference (%)
Diameter at Plane			
1 (d1)	25.60	24.04	6.09
Diameter at Plane			
2 (d2)	20.77	20.71	0.29
Diameter at Plane			
3 (d3)	25.87	24.72	4.46

5.3.2 Stress in the Interleaflet Triangle

The von Mises stress and the maximum contact pressure at the final deployment configuration were examined in the interleaflet triangle. Table 5.2 shows the comparison of the maximum, average, 99th and 90th percentile in the interleaflet triangles of both patients. It was found that both the maximum contact pressure and the von Mises stresses were higher in the patient with new on-set LBBB (Table 5.2).

Table 5.2: A comparison of von Mises stress (VMS) and contact pressure, in MPa, in the interleaflet triangle at final deployment.

	Non-LBBB	LBBB
Max VMS	0.324	0.463
Average VMS	0.048	0.050
99th Percentile VMS	0.182	0.190
90th Percentile VMS	0.097	0.103
Max Contact Pressure	0.375	0.598

5.3.4 The Impact of Stent Rotation

The impact of stent rotation on the maximum von Mises stress and contact pressure was then investigated. Table 5.3 shows the maximum von Mises stress and the maximum contact pressure for the 3 different stent orientations (0°, 40°, 80°) for the Non-LBBB patient. As the stent is positioned at the different 40° orientations a change in the maximum von Mises stress and contact pressure is observed with the highest contact pressure and von Mises stress observed when the stent is rotated 80°.

Table 5.3: A comparison of maximum von Mises stress and contact pressure in the interleaflet triangle where the bundle of His resides for the patient with no new-onset LBBB for different rotations of the stent (0°, 40°, 80°).

		Maximum	Maximum Von	Maximum
		Principal Stress	Mises Stress	Contact
Degrees of Rotation (°)		(MPa)	(MPa)	Pressure (MPa)
Non-LBBB	0	0.349	0.324	0.375
	40	0.425	0.388	0.413
	80	0.835	0.495	0.439

In Table 5.4 the results similarly demonstrate that stent rotation impacts the maximum von Mises stress and contact pressure. It can be seen that when rotated 40° there is a considerable drop in the peak von Mises stress compared to the other two implantation orientations.

Table 5.4: A comparison of maximum von Mises stress and contact pressure in the interleaflet triangle where the bundle of His resides for the patient with new-onset LBBB for different rotations of the stent (0°, 40°, 80°).

		Maximum Principal Stress (MPa)	Maximum Von Mises Stress (MPa)	Maximum Contact Pressure (MPa)
LBBB	0	1.831	0.463	0.598
	40	0.490	0.115	0.413
	80	1.434	0.468	0.676

The impact of stent rotation on the stress distribution in the interleaflet triangle between the non-coronary and right-coronary sinus was also investigated. Figure 5.6 and Figure 5.7 show contour plots of von Mises stress for each of the three stent orientations for the Non-LBBB and LBBB patient respectively. It can be seen that rotation of the valve stent leads to variations in the stress distribution in the interleaflet triangle.

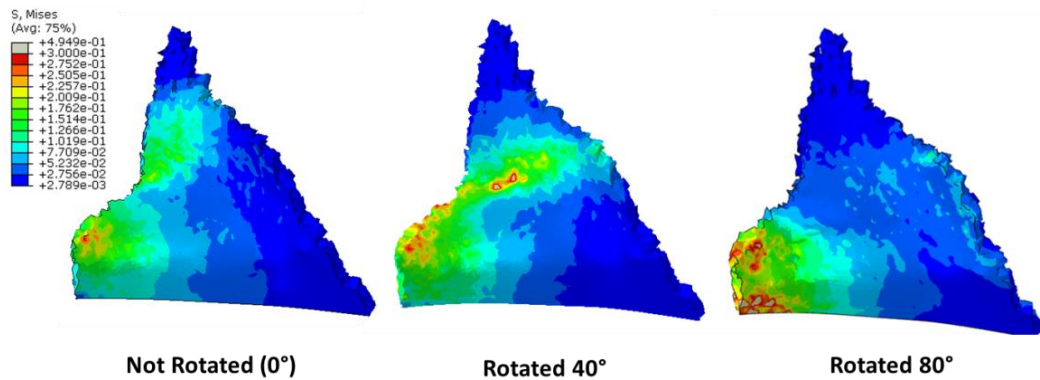


Figure 5.5: Contour plots of the von Mises stress (MPa) in the interleaflet triangle in the Non-LBBB patients at different stent rotations.

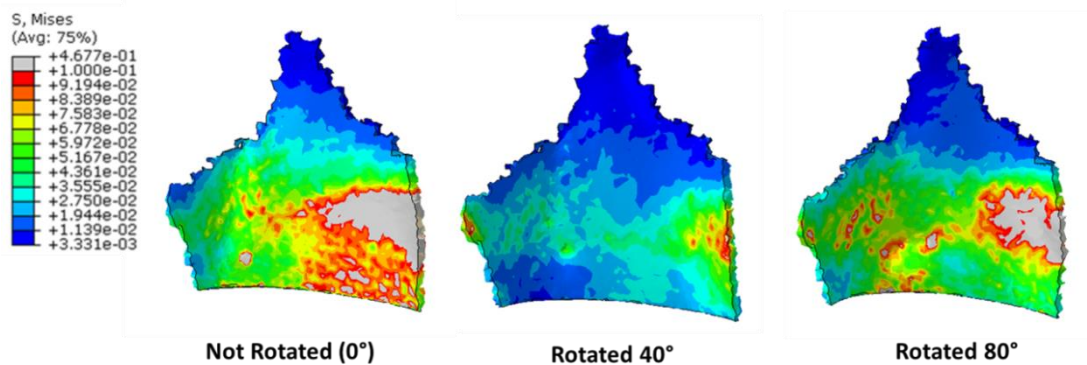


Figure 5.6: Contour plots of the von Mises stress (MPa) in the interleaflet triangle in the LBBB patients at different stent rotations.

5.4 Discussion

In this study, a computational model was developed to simulate deployment of a Lotus transcatheter aortic heart valve into patient-specific aortic roots with known clinical outcomes of new on-set and no new on-set LBBB. These models were applied to investigate the levels of tissue stress in the region of the bundle of His to gain an insight into the role of stress in post-TAVI conductance interference. This model was also applied to investigate the impact of the orientation of the Lotus valve on stress

distribution in the vicinity of the bundle of His. The results of this study have predicted that the patient with new on-set LBBB experienced higher von Mises stress and contact pressure, thus providing further evidence in support of the widely accepted hypothesis that stress elevation in the vicinity of the bundle of His is associated with conductance interference. Furthermore, it has been shown that rotation of the Lotus valve can lead to variations in the stress distribution in the aortic root and that these changes in stress distribution have the potential to lead to conductance abnormalities. These results highlight the benefit of using computational modelling as a pre-operative tool that can inform clinical decision-making regarding TAV positioning with the potential to reduce procedural complications such as conductance abnormalities.

There are a number of limitations to this study, which must be taken into account. Firstly, the assumption that the aortic root is an isotropic hyperelastic material may be considered a limitation due to the fact that the aortic root is known to be anisotropic. However, this model was deemed appropriate in capturing stress as previously discussed in further detail in Chapter 3. Secondly, patient-specific material data for each patient was not available and so the predictions may not be fully representative of the stresses experienced by each patient. Thirdly, the exact location of the bundle of His cannot be determined for each patient and thus the levels of stress in this region may not directly represent what is experienced by the conductance system. Furthermore, it must be noted that this study does not take into account any device repositioning that may have been conducted by the surgeon during the procedure, examining only the final deployment configuration. However, it has previously been hypothesised that the final implantation position is the most determining factor in inducing conductance abnormalities [44]. It must also be noted

that although using reduced integration lowers the computational cost of forming an element, a reduction in the number of integration points may lead to a less stiff element or hour glass mode where the stiffness matrix becomes zero [206]. Based on the patient angiograms no repositioning was carried out in either patient case; however, it must be noted that angiograms are not taken throughout the entire procedure and as the authors can only base this assumption on the angiograms the possibility of repositioning must still be considered. The models in this study examine static only initial deployment conditions, an analysis of stress throughout the cardiac cycle may give greater insight into the stresses leading to conductance abnormalities. Finally, in this study only one patient-specific anatomy was examined to represent each case and as such the specific results regarding the relationship between aortic tissue stress and occurrence of LBBB cannot be assumed to represent the entire population. However, these results are in agreement with the findings of Rocatello *et al.*, a study that examined 112 patients, whereby a maximum contact pressure greater than 0.39 MPa leads to conductance interference [44].

This is the first study to examine the impact of the Lotus valve stent orientation on stress distribution in the vicinity of the bundle of His in patients with and without new-onset conductance interference. The maximum contact pressure is greater than 0.39 MPa for the patient with new-onset LBBB (0.598 MPa) and less than 0.39 MPa for the patient with no new on-set conductance interference (0.375 MPa). Based on the results of the study by Rocatello *et al.*, a maximum contact pressure of 0.39 MPa distinguishes patients with and without new on-set conductance interference. Although the threshold of 0.39 MPa was based on a different valve type and using a different modelling approach, it is interesting that the results of both patient cases in

this study are in agreement with the findings of Rocatello *et al.* [44]. In this study, a 60% increase in the maximum contact pressure occurred in the LBBB case when compared to the Non-LBBB case. It must also be noted that the maximum, the average, the 99th and the 90th percentile von Mises stresses were higher in the patient with new-onset LBBB. Von Mises stress should also be considered as a predictor of new-onset conduction interference in future studies investigating stress relating to conduction abnormalities.

The results presented in this study demonstrate that the orientation of the valve stent can lead to an increase in the maximum contact pressure, maximum von Mises stress and a change in the stress distribution in the tissue in closest proximity to the heart's conduction system. For the Non-LBBB patient, when the valve was deployed at 40° or 80° orientations maximum contact pressures of 0.413 MPa and 0.439 MPa were predicted at each orientation respectively. This suggests that conduction interference may have occurred (contact pressure >0.39 MPa [44]) given a different orientation of the Lotus valve stent. For the patient who experienced LBBB, the values of maximum contact pressure at the 40° and 80° orientations indicate that conduction interference would have occurred at all stent rotations. However, the decrease in maximum von Mises stress at the 40° orientation must be noted. As previously mentioned further research into the relationship between von Mises stress and conduction abnormalities is required.

It must be noted the results do not suggest that the increase in stress is due to the posts themselves contacting the tissue. The Lotus valve posts are located on the inner portion of the stent and, in these models, are located above the region of interest. However, it appears the posts provide greater structural integrity to the regions of the

braid in proximity to the posts, creating greater rigidity and therefore increased stress in the surrounding tissue. These results suggest that positioning the posts in a manner which evades alignment with the interleaflet triangle where the bundle of His resides may reduce stress in this region. However, it must be noted that the optimal location of the valve posts could be dependent on patient-specific factors such as the shape of the annulus, level of calcification and calcification distribution, all of which may impact the degree of braid distortion and the impact stent rotation has on stress distribution.

5.5 Conclusion

In this chapter, a detailed computational analysis comparing patients with and without new on-set LBBB has been performed; providing evidence in support of the hypothesis that stress elevation in the vicinity of the bundle of His is associated with conductance interference. Furthermore, it has been found that the orientation of the Lotus valve can lead to variations in the stress distribution in the aortic root; specifically, that these stress distributions have the potential to induce new on-set LBBB. This study highlights the potential of computational modelling as a pre-operative tool to inform clinician's decision making regarding the optimal valve orientation with the potential to avoid conductance abnormalities associated with TAVI.

Chapter 6: A Patient-Specific Model of Transcatheter Valve Replacement in a Bicuspid Heart Valve.

6.1 Introduction

Bicuspid Aortic Valves (BAVs) are a common congenital cardiac malformation of the aortic valve, where two cusps of the valve have become fused together due to a rheumatic or inflammatory process [52, 53]. BAVs are the most common congenital valve abnormality and have been found to occur in 0.5-2% of patients [207-210]. Studies have suggested that >20% of patients requiring TAVI procedures are BAV patients [211, 212]. A BAV is comprised of two, often unequally sized, leaflets instead of the normal tri-leaflet aortic valve. Figure 6.1 shows a schematic of the different anatomic classifications of BAVs. It has been estimated that 90% of BAVs are Type I where the left and right leaflets are fused together [213].

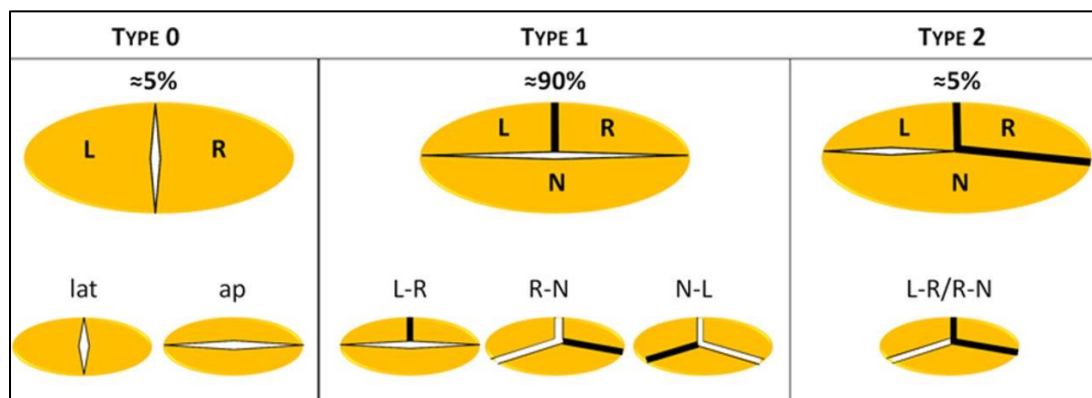


Figure 6.1: Schematic of the anatomical classification of BAVs where the prominent black line represents the fusion of the leaflets L, left coronary sinus; lat, lateral; N, noncoronary sinus; and R, right coronary sinus [213].

The TAVI trials that have established TAVI as the standard treatment in inoperable patients excluded BAV patients [58, 110, 111, 214, 215]. Further to this, the treatment of BAV was contraindicated for earlier generation valves due to concerns regarding the elliptical anatomy of BAVs leading to valve malfunction and valve positioning [216-218]. This is due to the abnormal valve geometry of BAVs commonly associated with eccentricity and factors such as asymmetrical valve calcification, difference in leaflet sizes and concomitant aortopathy [55, 141, 219-221]. Reports have associated BAVs with malfunction, malpositioning, incomplete sealing, severe PVL and aortic regurgitation [217, 218, 222-224]. However, due to increased experience and advances in technology the off-label treatment of BAV patients using TAVI is increasing [54]. Despite the higher rates of PVL and lower device success in earlier generation valves new generation valves have shown improved outcomes in the treatment of BAV patients with less PVL [225, 226]. In recent years, it has been shown that when comparing BAV patients to patients with a tricuspid aortic valves no significant difference was observed in 30-day mortality, mean peak gradients, PVL, need for pacemaker implantation and life-threatening bleeding [213, 216]. However, it has been argued that none of the reported BAV cohorts have adequate sample sizes and there is a need to broaden the group to be examined in future studies [55]. Furthermore, the appropriate sizing of TAVI for treatment of BAV patients has not been determined. PVL has been particularly problematic in relation to BAV patients, a common complication which has been shown to reduce with oversizing [20, 138, 158, 159]. It has previously been shown that using the SAPIEN 3 over the SAPIEN XT reduces the need for oversizing due to the sealing skirt. However, high percentages (2.3%) of annulus rupture occurred using

the SAPIEN 3. Recent expert analysis has proposed that the simple application of traditional annulus measurement and device sizing are not necessarily appropriate in treating BAV stenosis [58]. Furthermore, there is a concern relating to underexpansion of valves in BAV cases leading to structural failure of the valve with limited data existing on long-term durability in BAV cases [58]. It was highlighted by O’Sullivan and Windecker that BAV studies are limited in their absence of multi-detector CT post-TAVI, which did not allow for the opportunity to assess and learn from the post-deployment configuration of the bioprosthetic devices implanted [213]. Due to limited proof of efficacy, additional research is needed to investigate the efficacy of TAVI in the treatment of BAV stenosis [54, 55]. As TAVI progresses to treat lower-risk patients, the treatment of BAV stenosis using TAVI is becoming one of the most topical yet promising ventures in the field of cardiovascular intervention. This is heightened by the fact that BAVs are more prevalent in younger patient cohorts [55, 227] and bicuspid AS typically presents itself a decade or earlier than that of tri-leaflet patients [228].

The Lotus valve has shown good clinical outcomes in BAV patients, showing good fixation, circularity and good hemodynamics, without significant paravalvular regurgitation [59]. However, this clinical study only examined three patients and the author’s highlighted the uncertainty in the potential of improved outcomes given the use of a different valve size [59]. TAV sizing for BAV patients is currently based on those used for tricuspid aortic valves using perimeter-derived and area-derived diameters measured from MSCT scans. However, certain patients can fall into the criteria for more than one valve size (Table 6.1).

Table 6.1: Sizing chart for transcatheter valves [57].

	Portico	Lotus	Acurate	Engager
Valve sizes, mm	23/25	23/25/27	23/25/27	23/26
Aortic annulus dimension, mm	19–21 (23) 21–23 (25)	20–23 (23) 23–25 (25) 25–27 (27)	20–23 (23) 23–25 (25) 25–27 (27)	21–27
Sheath size, Fr	18	18/20	18	30
Leaflet tissue	Bovine	Bovine	Porcine	Bovine
Repositionable	Partial	Complete	Partial	Partial

In this chapter, a BAV patient is examined, which fits the criteria between a 25 mm and 27 mm Lotus valve. The objective is to apply a patient-specific FE model to examine a case of over- and undersizing in the same patient anatomy to directly examine the impact of sizing while mitigating any variation due to differing patient anatomies. This is carried out by investigating a case of BAV stenosis treated with a 25 mm Lotus valve and comparing the biomechanical interaction and the post-deployment configuration of a 27 mm Lotus valve in the same patient to investigate the impact of different sizing criteria in a BAV patient.

6.2 Materials and Methods

6.2.1 Aortic Root Model

A patient-specific model of a stenosed BAV (Type I) was reconstructed from MSCT images with slice thickness of 0.625 mm, slice dimensions of 512 x 512 and pixel spacing of 0.664 mm. Mimics 14.1 Imaging Software (Materialise, Leuven, Belgium) was used to threshold the leaflets, calcifications, and aortic root. 3 Matic (Materialise, Leuven, Belgium) and TetGen (WIAS, Berlin, Germany) were used to generate volume meshes of the aortic root and calcifications and leaflets similar to the methods of Section 5.2.1. The geometries were then imported into Abaqus Explicit 6.13

(SIMULIA, Providence, RI). An assembly was then generated matching the corresponding nodal positions of the intersecting surfaces.

6.2.2 LotusTM Valve Model

Two different sizes of Lotus valve stent geometry; 25 mm and 27 mm were created. The stent geometry was imported into Abaqus 6.13 as a wire part and meshed using 3-noded quadratic beam elements (B32). The overlap between the braids was modelled using spring connector elements.

6.2.3 Constitutive Models

The Lotus valve stent was modelled using a superelastic material inbuilt user subroutine (VUMAT), correlated to the experimental crush test of a nitinol Lotus valve stent as described in Section 3.2.3.

The ascending aorta and the aortic sinus were modelled as isotropic hyperelastic materials. They were model using the first order Ogden model [189] fitted to uniaxial test data of human tissue [40, 190]. The aortic valve leaflets were modelled using a linear elastic model with Young's modulus of 1.6 MPa, a Poisson's ratio of 0.495 and a density of 1140 kg/m³ [40, 194]. Similarly, to Chapter 5, the calcification was modelled as a linear elastic material with Young's modulus 10 MPa, Poisson's ratio 0.35 and a density of 2000 kg/m³ [30, 176].

6.2.4 Boundary and Loading Conditions

The crimping and deployment of the two valve sizes (25 mm and 27 mm) into the BAV geometry was modelled in Abaqus Explicit 6.13 (SIMULIA, Providence, RI). The same methods outlined in Section 5.2.4 were implemented whereby the stents were crimped inward radially using zero friction contact. The stents were then unsheathed into the aortic root by applying an axial displacement to the crimper.

During stent deployment, a coefficient of friction of 0.36 was used between the TAV stent and the calcifications (based on the results of Chapter 4), and the interaction between the stent and the aortic sinus was modelled using a coefficient of friction of 0.1 [46]. A third loading step was applied to the stent to simulate locking of the device using six connector elements, wherein three connectors represented the Lotus valve stent post and three connectors represented the string ties. The posts and ties were displaced inward to ensure the valve was locked to a height of 19 mm.

6.3 Results

The results of the 25 mm model were compared to real life patient angiograms of the 25 mm BAV patient case.

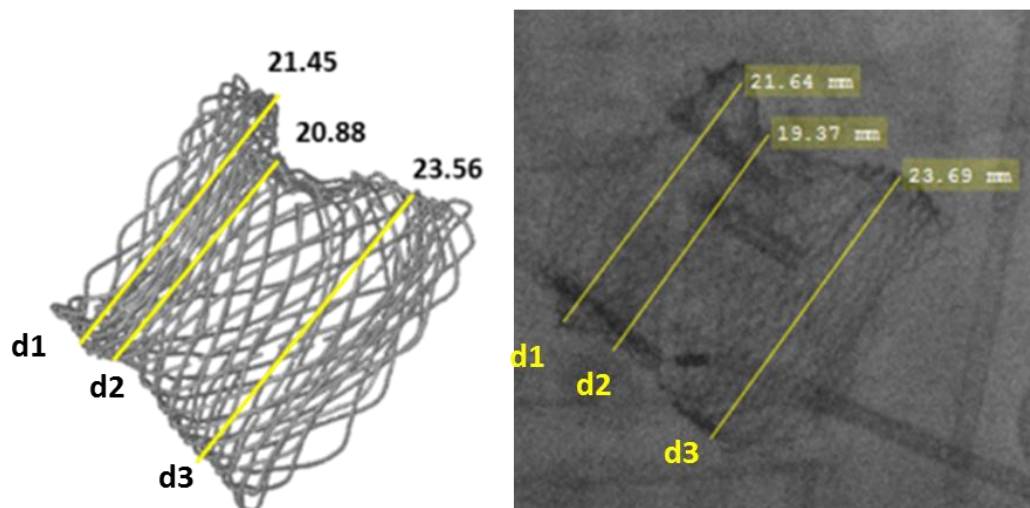


Figure 6.2: Comparison of model stent geometry with that of post-deployment angiogram from the real-life case. d1, d2, and d3 are the diameters at plane 1, 2 and 3 respectively.

Figure 6.2 shows the model predictions compared to angiogram images of the stent post-deployment. Measurements of the diameter were taken at 3 planes along the stent,

which can be seen in Table 6.2, show the correlation between the model geometry and the real-life case, with percentage errors averaging $<3\%$ in the stent dimensions. Figure 6.2 demonstrates the ability of the model to accurately predict the final deployment geometry of the Lotus valve stent with an almost identical representation of the reduction of the stent's waist.

Table 6.2: Comparison of model stent dimensions with that of post-deployment angiogram from the real-life case.

	Model Dimensions (mm)	Angio Dimensions (mm)	Percentage Difference (%)
Diameter at Plane 1 (d1)	21.45	21.36	0.42
Diameter at Plane 2 (d2)	20.88	19.37	7.23
Diameter at Plane 3 (d3)	23.56	23.69	0.55

6.3.1 Eccentricity

Stent eccentricity was firstly examined as elliptical deployment geometries are a complication associated with BAV patients [141] and are associated with leaflet distortion. Leaflet distortion can alter leaflet kinematics and fluid mechanics and ultimately lead to accelerated fatigue of the valve leaflets [29, 139, 144, 161]. This is of particular concern with BAV patients due to the limited data existing on long-term

durability in BAV cases and the younger patient cohorts associated with BAVs [58]. Eccentricities were measured at the inflow segment of the stent, as this is where the leaflet attachment points reside and represent the highest area of leaflet distortion. The eccentricity of the valve stent was measured using equation 6.1 [140].

$$e = 1 - \left(\frac{D_{min}}{D_{max}} \right) \quad (\text{Eq 6.1})$$

where D_{max} and D_{min} are the major and minor axes of the ellipse respectively and zero is the optimal eccentricity.

The stent eccentricities for all cases can be found in Table 6.3. At the basal leaflet attachments, the eccentricity in the 25 mm valve was predicted to be 0.152, whereas an eccentricity of 0.195 was predicted for the 27 mm case.

6.3.2 Stress

The 99th percentile (σ^{99}) and the average (σ_{avg}) von Mises stress in the aortic sinus were examined for both valve sizes (Table 6.3). It was predicted that the 27 mm valve had the higher σ^{99} (0.536 MPa) and σ_{avg} (0.118 MPa) when compared to the 25 mm valve case where σ^{99} and σ_{avg} were predicted as 0.118 MPa and 0.017 MPa respectively. Contour plots of the stress in the tissue can be seen in Figure 6.3 where the 27 mm valve shows higher percentage volume of tissue at higher von Mises stress in comparison to the 25 mm case. The maximum and 99th percentile stress in the interleaflet triangle were also compared for both valve sizes with the 25 mm valve showing lower stress (0.172, 0.083 MPa) when compared to the 27 mm valve (1.283, 0.359 MPa).

Table 6.3: Table of results comparing eccentricity and von Mises stress between the four cases.

Valve Size	Eccentricity	σ^{99} (MPa)	σ_{avg} (MPa)	σ_{int} (MPa)	σ^{99}_{int} (MPa)
25 mm	0.152	0.118	0.017	0.172	0.083
27 mm	0.195	0.536	0.062	1.283	0.359

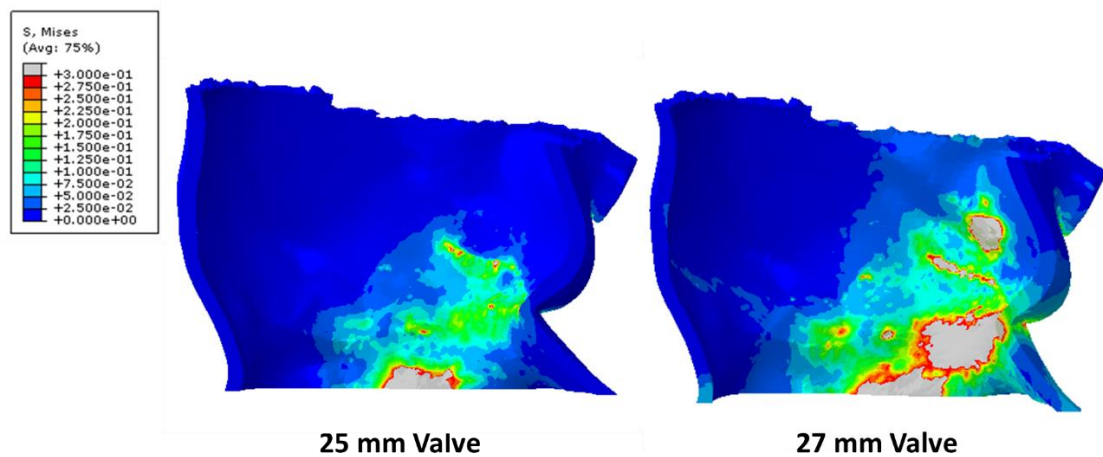


Figure 6.3: Contour plots von Mises stress in the aortic sinus (MPa) post of deployment the 25 mm and 27 mm valve.

6.3.3 Paravalvular Leakage

Using similar methods implemented by Wang *et al.* to qualitatively examine PVL [40]

Figure 6.4 demonstrates the areas with potential for PVL for both valve sizes. There

does not appear to be a considerable difference in the regions with potential for PVL reported in both valve cases.

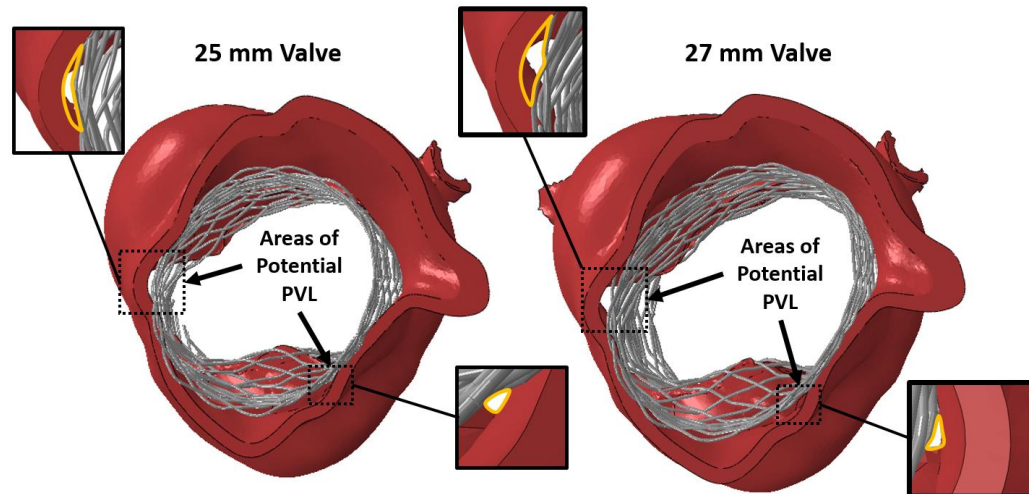


Figure 6.4: Schematic of the valve stent and aortic root with potential for paravalvular leakage.

6.4 Discussion

In this study, patient-specific modelling was used to investigate a patient-specific case of a BAV patient treated with the Lotus valve. The results of this model have shown near perfect correlation to images of the real-life patient case post-TAVI. This model has been used to investigate TAV sizing for BAV patients using the Lotus valve by comparing the two different valve sizes (25 mm and 27 mm) in the same patient anatomy in terms of stent eccentricity and tissue stress. These results suggest that the 25 mm valve was correctly sized for this patient by both lowering eccentricity and tissue stress when compared to the oversized 27 mm valve. The results also suggest that the treatment of BAV patients is reasonable using the Lotus valve in terms of eccentricity. The eccentricities reported for the Lotus valve post-deployment in the

BAV patient in this study are comparable to those reported in the treatment of tricuspid aortic valve stenosis using other valve types.

Many of the assumptions that are related to the modelling techniques that have been previously mentioned in Chapter 5 also apply to this study, namely; the uses of isotropic material properties over anisotropic properties, aortic pressure and pre-stress, and that the model examines static only initial deployment conditions. It must also be noted that PVL is examined qualitatively in this study. PVL cannot be assessed quantitatively in the absence of CFD analysis and furthermore, PVL of the Lotus valve is dependent on the paravalvular seal which has been shown to significantly reduce volumes of PVL [229]. In the absence of modelling the paravalvular seal, an accurate representation of the volumes of PVL cannot be quantified. However, it is reasonable to assume the paravalvular seal would have a similar impact in reducing PVL for both valve sizes. In this study, the assessment of PVL was used solely as a comparative measure between the two valves using similar methods to those previously used by Wang *et al.* in assessing the potential for PVL [40]. Finally, in this study only one patient-specific anatomy was examined, and as such the specific results regarding the relationship between valve sizing, eccentricity and aortic tissue stress cannot be assumed to represent the entire population. However, this is the first detailed analysis to provide an understanding of the impact of different TAV sizing in BAV patients.

It was predicted in this study that the stent was more eccentric in the 27 mm case with an eccentricity of 0.195 at the basal plane. This compared to an eccentricity of 0.152 in the 25 mm case. Clinically it has been found that bicuspid patient anatomies have been shown to lead to more eccentric stent geometries [141, 217]. The eccentricity of the native aortic root for the BAV patient in this study is 0.143. The

eccentricities observed in this patient are higher than what has previously been reported for the Lotus valve in tricuspid aortic valve patients. Its unique locking mechanism and rigid locked stent leads to desirable eccentricities with average eccentricities of 0.06 ± 0.04 reported clinically for tricuspid aortic valve patients [140]. However, it must be noted that levels of eccentricity of 0.18 and 0.25 have been computationally predicted for the CoreValve and the Edwards SAPIEN Valve in clinical cases of tricuspid aortic valve patients [30, 173]. These results indicate that rigid locked stent of the Lotus valve is suitable in the treatment of eccentric bicuspid anatomies due to its ability to retain a circular configuration.

It has previously been predicted using a combination of FEA and CFD analysis that valve eccentricities greater than 0.134 lead to backflow leakage, whereas an eccentricity of 0.267 was predicted to increase the peak leaflet stress by 143% [42]. Although the eccentricity of 0.152 reported for the 25 mm valve and 0.195 reported for the 27 mm valve are acceptable in terms of what has been reported clinically, backflow would be expected for both valve sizes. This should be considered carefully in relation to the treatment of BAV patients, particularly as TAVI move into the treatment of younger patient cohorts. Nevertheless, the 25 mm valve showed preferable eccentricity over the 27 mm valve and comparable eccentricities to those previously reported in clinical cases of tricuspid aortic valve patients treated with TAVs.

The levels of von Mises stress were compared for both valve sizes the 25 mm case shows lower stress in the sinus when compared to the 27 mm valve case. Although the σ^{99} is below the ultimate tensile stress of the aortic sinus (2.3 to 3.1 MPa) [39], it must be noted that an increase in stress can lead to tissue damage and should

be avoided. The values of maximum and 99th percentile peak stress in the interleaflet triangle were 0.172 MPa and 0.083 MPa for the 25 mm valve and 1.283 MPa and 0.359 MPa for the 27 mm valve. In Chapter 5 of this thesis, the patient with conductance interference showed maximum and 99th percentile von Mises stress of 0.463 MPa and 0.190 MPa in the interleaflet triangle. These results suggest higher potential for conductance abnormalities if this patient was to receive a 27 mm valve.

The results of this study suggest that the 25 mm valve was more suitable in terms of reduction of stress in the tissue and reduced eccentricity. Current guidelines for TAVI suggest upsizing the device relative to the native annulus to reduce volumes of PVL [138, 158, 159]. However, Figure 6.4 shows cross sections of the stent that indicate that for this patient case oversizing does not appear to considerably reduce the potential for PVL. Therefore, on the basis of the results of this study, the 25 mm valve size was deemed most appropriate for the treatment of this BAV patient.

6.5 Conclusion

In this study, FE models were developed simulating the deployment of a 25 mm and a 27 mm Lotus valve stent into the patient-specific aortic root geometry of a clinical BAV case to investigate the efficacy of the Lotus valve in the treatment of BAV stenosis and to examine oversizing in a BAV patient case. The results of this study predicted that the eccentricity for this patient was lower than what has previously been reported computationally for the other valve types in the treatment of tricuspid aortic valve patients. These results suggest that the Lotus valve is suitable in treating BAV patients in terms of reducing eccentricities. Furthermore, it was shown the valve sizing used in this patient was the most suitable in terms of eccentricity and stress reduction without providing a substantial reduction in PVL. These results indicate that the

treatment of BAV patients is reasonable using the Lotus valve and that the sizing algorithms used for tricuspid aortic valve patients have shown the best outcomes for this patient case. This suggests that traditional annulus measurement and device sizing is suitable in the case of the Lotus valve.

Chapter 7: Discussion and Conclusion

7.1 Introduction

This chapter summarises the main findings of this thesis drawing together the knowledge gained from the combination of experimental and computational approaches performed during the duration of the candidates PhD studies. These studies have provided an advanced understanding into the tissue-stent interaction between a TAV stent and a stenosed aortic root, and an understanding of the forces required to maintain a secure valve, whilst also reducing the damage to the surrounding anatomy leading to patient complications. The relationship between the individual chapters of this thesis and their context in respect of published literature can be found in a graphical representation in Figure 7.1 of the thesis and is discussed in detail in Section 7.3. The key findings of the thesis are discussed in relation to the context of other relevant studies and the implications of the thesis for the future design and information regarding patient-specific device selection is examined. Finally, recommendations for future work and perspectives in the TAVI field are discussed.

7.2 Main Findings of the Thesis

The research conducted in this thesis implemented patient-specific computational models to provide an advanced understanding of the interaction of the Lotus valve with the native anatomy, specifically focusing on (1) the levels of stress leading to conductance interference, (2) the forces needed to secure the valve in place and (3) the sizing of bicuspid patient geometries.

This thesis combined computational and experimental modelling to investigate the impact of the tissue-stent interaction in securing the valve in place while examining the impact of stent deployment on tissue damage in the aortic root. A computational approach was employed to examine the response of the aortic sinus tissue at different positions and orientations to investigate different patient-specific procedural complications, while an experimental model was used to examine the role of calcification in anchoring the valve in the aortic root. The key contributions of each of the hypothesis are summarised below.

7.2.1 Hypothesis 1: Supra-annular positioning reduces stress in the interleaflet triangle in which the conductance system (Bundle of His) resides

Chapter 3 of this thesis examines the impact of the positioning of the Lotus valve. The Lotus valve has a repositionable locking mechanism that makes it unique when compared to first generation self-expanding and balloon expandable TAVs. However, the Lotus valve has been associated with an increase in the number of patients presenting with new-onset LBBB (55.2%) when compared to the Edwards SAPIEN (13%) and the CoreValve (38.8%) [51]. Using a FE approach, a model of the Lotus valve braided stent and its unique locking mechanism was created, and implantation of the stent into a patient-specific aortic root at three different implantation depths was simulated. The results of this model demonstrated that examining the peak stresses; although important in cases of aortic root rupture, do not give insight into the stresses leading to more common procedural complications such as conductance interference. This study examined levels of stress in the interleaflet triangle where the bundle of His resides to provide insight into the potential causes of conductance interference. The results of this study suggest that higher implantation positions reduce stress in the interleaflet triangle and thus may have the potential to lower incidences of

conductance interference. This provides the first quantitative evidence in support of supra-annular positioning, which is in agreement with clinical observations whereby supra-annular positioning shows less incidence of conductance interference [36-38]. Further to this, evidence in support of hypothesis 1 of this thesis “*Supra-annular positioning reduces stress in the interleaflet triangle in which the conductance system (Bundle of His) resides*” has been provided. The results of this chapter indicate that investigating the levels of stress in the vicinity of the conductance system may give a greater explanation into the mechanisms causing conductance interference. Furthermore, this chapter provides an understanding of appropriate valve positioning, with respect to tissue stresses, which could allow clinicians to make more informed decisions regarding patient-specific positioning and allowing for greater insight into device design.

7.2.2 Hypothesis 2: Calcification secures the TAV in place by increasing the friction in the interaction between the TAV stent and a stenosed aortic root

In Chapter 4 of this thesis, the impact of calcification on the stent-tissue interaction was investigated. This was investigated using an *in vitro* experimental approach to compare the pullout force and coefficient of friction for calcified and non-calcified aortic roots. This research built upon a previous study that investigated the tissue-stent interaction without the presence of calcification [46]. It was found that the presence of calcification leads to an increase in the coefficient of friction between the native valve tissue and the stent from 0.1 to 0.36, thereby playing a role in securing the valve in place. This research provides a novel method for investigating the impact of calcification on TAVI in an *in vitro* setting as well as providing quantitative evidence in support of hypothesis 2 of this thesis “*Calcification secures the TAV in place by*

increasing the friction in the interaction between the TAV stent and a stenosed aortic root”.

The results of this study are important in device selection as current valves in the market have one valve size covering a range of aortic root sizes spanning up to 3 mm (eg. CoreValve 26 mm treats annulus dimensions ranging 20 -23 mm [230]). Chapter 3 of this thesis and previous studies predict that calcification leads to maximum peak stress and higher potential for aortic root rupture [39, 231]. The results of Chapter 4 suggest that as the valve stent is more secure in more calcified roots clinicians may slightly undersize the stent, which could potentially lead to lower stresses in the native valve complex whilst also maintaining a secure valve due to the high levels of calcification.

Further to this, this study examines the impact of calcification on the friction coefficient between the TAV stent and the stenotic aortic root. Previous to this, the only study to investigate friction in the aortic root excluded calcification and found it to be 0.1 [46] and this value has been used in computational modelling studies [29, 39, 40, 173, 231] to model the tissue-stent interaction. This coefficient of friction of 0.1 in these models may lead to an underestimation of the levels of stress the stent exerts on the aortic root. The findings of this PhD thesis should be carefully considered in future studies modelling the impact of the stent and aortic root. This can also be considered in cases of stents deployed peripherally around the body in areas where the plaque is heavily calcified.

7.2.3 Hypothesis 3: Orientation of the Lotus valve impacts the stress in the vicinity of the bundle of His and can induce conductance interference

In Chapter 5 of this thesis, a FE approach was implemented to examine two patient-specific cases; one in which a patient developed new on-set LBBB and one where a patient developed no new-onset conductance abnormalities. In this chapter, knowledge gained in Chapter 3 and 4 of this thesis was combined to create an advanced computational model that can accurately predict the final deployment geometry of the Lotus valve demonstrating highly accurate representations of the stent in its final deployment configuration. This research allows the complication of conductance interference to be examined by comparing two different patient cases and examining the levels of stress in the tissue, something that cannot be done clinically. Furthermore, this chapter examines for the first-time orientation of the Lotus valve in relation to conductance abnormalities. The results presented in this chapter demonstrate that orientation of the valve stent has the potential to induce conductance interference.

New on-set conductance interference is a relatively misunderstood complication of TAVI and the exact cause is still unknown. In Chapter 5 of the thesis, higher stress was predicted in the interleaflet triangle where the bundle of His resides in the patient that experienced new on-set LBBB when compared to a patient with no new-onset conductance interference. This is in agreement with the widely accepted hypothesis that injury in this area leads to conductance abnormalities. The results of this chapter were also in agreement with a previous study stating that a maximum contact pressure greater than 0.39 MPa is a predictor of conductance abnormalities [44]. Further to this, it was also demonstrated that von Mises stress may also be a predictor of conductance abnormalities.

Finally, it was predicted that when the valve stent was rotated in a patient who presented no new on-set LBBB the maximum contact pressure increased from 0.375 MPa (<0.39 MPa) to 0.598 MPa (>0.39 MPa). These results indicate that conductance abnormalities would occur if the valve had been orientated differently, thereby corroborating hypothesis 3 of this thesis “*Orientation of the Lotus valve impacts the stress in the vicinity of the bundle of His and can induce conductance interference*”. This chapter uses computational modelling and applies it to a relatively unexplored problem to provide insight into the mechanisms behind conductance interferences and provides a platform to motivate further studies in this area.

7.2.4 Hypothesis 4: Bicuspid patients with stenosed aortic valves can be effectively treated using the LotusTM Valves in terms of stent eccentricity and tissue stress using traditional device sizing.

In Chapter 6 the efficacy of TAVI to treat BAV patients was investigated using a computational approach with a focus on whether the sizing algorithms tailored towards tricuspid patients were suitable in the treatment of BAV patients. This chapter combines knowledge gained in Chapter 3 and 4 of this thesis and provides further validation of the modelling approach developed in Chapter 5, to investigate the controversial issue regarding BAV patient sizing. To the author's knowledge, this is the first study examining TAV sizing in BAV patients with the use of FEA allowing comparison of the effect of different valve sizes in the same patient anatomy. As previously mentioned in Chapter 6 of this thesis, the efficacy of TAVI in treating BAV patient is still an area of controversy. In this study, the post-deployment results of two-valve sizes were compared in the same BAV patient anatomy in terms of eccentric deployment geometry and tissue stress. The results of the study show that after initial deployment a BAV patient demonstrates good outcomes in terms of stent eccentricity

and levels of tissue stress with sizing algorithms designed for tricuspid patients, therefore, providing evidence in support of hypothesis 4 of this thesis “*Bicuspid patients with stenosed aortic valves can be effectively treated using the LotusTM Valves in terms of stent eccentricity and tissue stress using traditional device sizing*”. The results of this chapter provide great insight into some of the concerns associated with BAV patients and can give clinicians greater confidence in the sizing algorithms that are currently in place.

7.3 Implications of this Thesis in the field of Transcatheter Valves

In this section, the findings of hypothesis 1-4 are further considered in the context of the current understanding of the relationship between the TAV stent and the stenotic aortic root into which it is deployed. The studies in this thesis have focused on examining the tissue-stent interaction and its impact in the context of specific complications of TAVI.

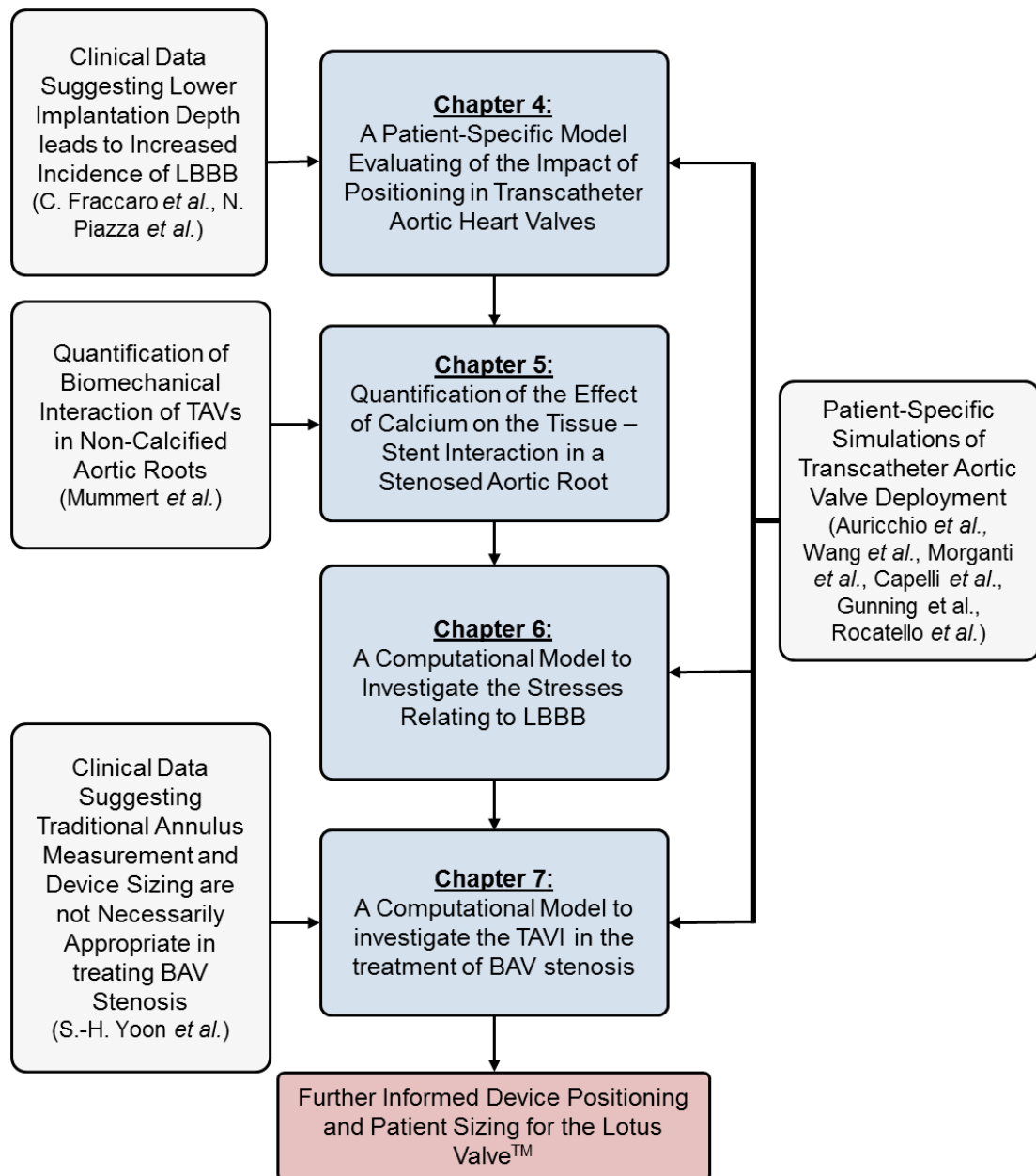


Figure 7.1: Graphical representation of the work conducted as part of this PhD Thesis in the context of previous studies.

Although patient-specific modelling has before focused on complications such as aortic root rupture [39], PVL and coronary occlusion [40, 41], asymmetric expansion and leaflet stresses [29, 42] and poor hemodynamic performance [43], it has never been used to examine the Lotus valve, and the impact of its unique locking

mechanism, in particular in relation to conductance interference or bicuspid patient sizing.

Implications for the Lotus Valve

One of the major outcomes of this thesis is a computational framework that has investigated three patient-specific cases and predicted comparable results to their angiogram data. The Lotus valves complex locking mechanism leads to uneven braid distribution and irregular stent geometries, which makes modelling the valve successfully relatively complex. In this thesis, a computational framework has been provided that accurately models the irregular braid distribution in line with what has been seen in real life cases. This will enable Boston Scientific to address patient-specific concerns post-operatively using the framework developed throughout this thesis. Further to this, the results of this thesis have already examined particular complications of interest with regards to the Lotus valve. In Chapter 3, the first quantitative evidence in support of positioning the valve at higher implantation depths was provided. Further to this, in Chapter 5 the potential mechanisms behind conductance interference with relation to stress were examined and it was reported that higher stress in the interleaflet triangle between the right and non-coronary sinus is associated with conductance interference. Moreover, rotation of the Lotus valve posts can directly influence stress in this region. Finally, Chapter 6 addresses concerns with the use of the Lotus valve in the treatment of BAV patients. This provides Boston Scientific with essential data on the impact of over and under-sizing in a borderline patient case using the same patient anatomy. This allows for greater confidence and more informed decisions on the sizing of their valve for BAV patients.

Implications for the Tissue-Stent Interaction

Although the motivation of the studies of this thesis was driven by complications associated with the Lotus valve, the results of this thesis provide knowledge that can be applied across the field regardless of valve type. Primarily, the most impactful outcome of this thesis is the impact of calcification in securing the valve in place. One of the major limitations of TAVI, when compared to surgical valves, is the fact that unlike surgical valve TAVs are not sutured into place. This means that there is a huge reliance on the tissue-stent interaction when it comes to ensuring that the stent is secure enough to withstand the forces acting to dislodge the stent *in vivo*. This heavily influences the design of TAVI valves. Although the results of this thesis examined a generic braided stent geometry, the *in vitro* model detailed in Chapter 4 of this thesis can be applied to any stent geometry, to examine how the device-specific tissue-stent interaction is altered in the presence of calcification.

Implications for Conductance Interference

Conductance interference is one of few TAVI complications that is not fully understood. All TAVI valves on the market have reported a percentage of patients who develop conductance disturbances as a result of a TAVI procedure [51]. The levels of tissue stress relating to conductance interference have never been examined computationally using the Lotus valve. The results of Chapter 3 and 5 of this thesis, demonstrate the potential for computational modelling to play a role in further understanding the levels of stress that are acceptable to secure the valve in place while preventing damage to the conductance system. The advantages of using FE models to inform pre-procedural planning and reduce complications while improving patient

outcomes is also highlighted in Chapters 3 and 5 of this thesis. With conductance abnormalities, such as new on-set LBBB, being linked to increased mortality rates [49] it is an area that requires further research and understanding. Further to this, a greater understanding of the mechanisms behind TAVI leading to conductance interference may lead to a greater understanding of other conductance related diseases and the potential to develop new solutions. The results of this thesis do not stand alone in solving the relationship between stress and conductance interference, however, they provide further insight into the threshold levels for stress that lead to such complications.

Implications for Bicuspid Aortic Valves

Finally, although this study focuses on the efficacy of the treatment of BAV with focus on the Lotus valve the results of Chapter 6 of this thesis emphasise the importance of using computational modelling to inform device selection and patient sizing. The results of Chapter 6 investigate two valves in the same patient, something that cannot be assessed *in vivo*. Computational modelling can be used as a preclinical tool for BAV patients as valve sizing in BAV patients remains a topic of controversy. Furthermore, Chapter 6 demonstrated that in the case of the given patient, oversizing would have led to excessive tissue damage and an increase in stent eccentricity with no indication of reduced PVL, suggesting that current sizing for BAV patients is suitable in relation to the Lotus valve.

The studies outlined in this thesis have added to the literature by providing a more in-depth knowledge of the impact of implantation depth on the levels of stress in the conductance system, the impact of calcification on the TAV-tissue interaction,

providing further evidence in support of the widely accepted hypothesis that stress in the interleaflet triangle leads to conductance interference and finally examining the efficacy of TAVI to treat BAV patients. Combined, these studies provide further insight into areas of the tissue-stent relationship that have not yet been investigated. The results of this thesis will greater inform decisions regarding valve positioning, device selection criteria and device design as is discussed in the following section of this thesis.

Implications for Valve Design and Positioning

This thesis focuses primarily on the Lotus valve with the results directly informing the positioning to reduce the high incidences of conductance interference associated with the valve. In Chapter 3, evidence is provided suggesting that higher implantation depths will reduce conductance interference. Furthermore, in Chapter 5 evidence is provided that the orientation of the Lotus valve can reduce incidences of stress relating to conductance interference in the interleaflet triangle between the right and non-coronary sinus.

It must be noted that although these studies were conducted on the Lotus valve the results have a wider implication on the design of TAVs. For example, the impact of implantation depth has previously been associated with conductance disturbances [129, 130] and on the basis of the results of Chapter 3 it would suggest that the design of lower profile valves may be less likely to cause higher levels of stress in the region of the conductance system while ensuring that there is no coronary occlusion. These results also suggested that in patients with short LVOTs and/or higher coronary ostia, the TAV should be positioned higher regardless of valve type or a lower profile valves

should be used. It may also influence the area where valves direct their radial force or position their leaflets relative to the height of the valve.

Further to this, the evidence suggesting that positioning the posts of the Lotus valve closer to the region where the bundle of His resides may increase conductance disturbances has not been reported clinically or investigated previously. Alongside informing positioning of the Lotus valve, it may influence future generations of TAVs as this research suggests that structures similar in nature to the Lotus valve posts may cause similar complications. Similar structures may be best avoided in valve design or designed in a manner to ensure easy repositioning by the clinician to a position that would decrease conductance interference or other complications.

7.4 Future Recommendations

7.4.1 Further Investigation of the Mechanism behind Conductance Disturbances

In Chapter 3 and 5 of this study, evidence is provided suggesting that examining the stresses in the interleaflet triangle between the right and non-coronary sinus could lead to greater insight into what threshold of stress is acceptable while preventing conductance interference. It must be noted that computational modelling has is limited when relating stress to conductance interference in the absence of material properties relating to each specific patient and that the exact location of the bundle of His cannot be known. Although the results of these studies answer and raise some interesting questions they do not definitively answer the threshold levels of stress that should be avoided to reduce conductance disturbance.

It is the author's opinion that in order to gain further understanding of these stress levels it would require one of, or a combination of two, methods. Firstly, a

computational multiscale modelling approach, which could relate tissue stress to the stress experienced at a cellular level. This could then be fed into experimental studies at the cellular level, for example using devices such as Flexcell (Flexcell®, Burlington, NC, USA) or MCFX (CellScale, Ontario, CA) to understand at what stress level myocardial or pacemaker cells begin to stop electrical signalling and what levels of stress necrosis would occur. These results could then be examined to see if they correlate to the stresses observed in a case of LBBB versus no new-onset conduction abnormalities.

The other method would involve an animal model where the conduction system could be monitored alongside a live angiogram throughout the duration of the procedure so that the exact point at which the interference occurred versus the positions of the device could be correlated. Further to this, the animal heart geometry could be reconstructed using *in vivo* micro-CT and this could be modelled computationally. Post-operatively the animal could be monitored before sacrifice, providing data on cases in which conduction interference resolves itself after a period of time. Additionally, the exact location of the bundle of His could be found using histological and immunofluorescent staining, while tissue testing would further inform the variation in the mechanical properties from animal to animal, potentially providing more accurate predictions. Finally, histology could be performed on the heart tissue in the interleaflet triangle after the heart is explanted allowing for the amount of tissue damaged to be quantified. Any valve receiving regulatory approval must undergo animal trials, so these methods could be investigated alongside on-going trials.

7.4.2 Further Consideration for Calcification Severity and Patterns

In Chapter 4 of this thesis, the impact of calcification on the tissue-stent interaction is outlined and it was found that, for the given braided stent geometry, calcification significantly increased the forces required to dislodge the stent. This should be considered in the case of each individual TAV design. In the context of this thesis, the impact of calcification was demonstrated and presented using the *in vitro* model. This model can provide an important insight into device design; however, it should be considered for each individual TAV device as the tissue-stent interaction will differ with varying stent designs. Furthermore, it should be examined for a variety of different calcification severities and different specific calcification patterns to give a full context of the behaviour of each individual device.

7.5 Conclusion

In conclusion, this thesis has presented a combination of experimental and computational methods performed throughout the duration of the author's PhD studies to investigate the tissue-stent interaction with a focus on specific procedural complications of the Lotus valve. Computational models were developed to investigate the impact of stent implantation depth and orientation on stress related to conductance interference and investigate valve sizing in a stenosed bicuspid aortic valve. Experimental methods were developed to inform the impact of calcification in securing the valve in the aortic root and used to inform the computational modelling approach that has been developed throughout this thesis. The results of these studies inform device positioning and patient sizing for the Lotus valve and provide a greater knowledge for the development of next-generation TAV devices.

References

- [1] N. M. Rajamannan *et al.*, "Calcific aortic valve disease: not simply a degenerative process: A review and agenda for research from the National Heart and Lung and Blood Institute Aortic Stenosis Working Group. Executive summary: Calcific aortic valve disease-2011 update," (in eng), *Circulation*, vol. 124, no. 16, pp. 1783-91, Oct 18 2011.
- [2] K. Maganti, V. H. Rigolin, M. E. Sarano, and R. O. Bonow, "Valvular Heart Disease: Diagnosis and Management," *Mayo Clinic Proceedings*, vol. 85, no. 5, pp. 483-500, 2010.
- [3] C. E. Kurtz and C. M. Otto, "Aortic stenosis: clinical aspects of diagnosis and management, with 10 illustrative case reports from a 25-year experience," (in eng), *Medicine (Baltimore)*, vol. 89, no. 6, pp. 349-79, Nov 2010.
- [4] R. Schueler, C. Hammerstingl, J. M. Sinning, G. Nickenig, and H. Omran, "Prognosis of octogenarians with severe aortic valve stenosis at high risk for cardiovascular surgery," (in eng), *Heart*, vol. 96, no. 22, pp. 1831-6, Nov 2010.
- [5] S. Frank, A. Johnson, and J. Ross, Jr., "Natural history of valvular aortic stenosis," (in eng), *Br Heart J*, vol. 35, no. 1, pp. 41-6, Jan 1973.
- [6] J. Ross, Jr. and E. Braunwald, "Aortic stenosis," (in eng), *Circulation*, vol. 38, no. 1 Suppl, pp. 61-7, Jul 1968.
- [7] D. R. Holmes *et al.*, "2012 ACCF/AATS/SCAI/STS Expert Consensus Document on Transcatheter Aortic Valve Replacement," *Journal of the American College of Cardiology*, 10.1016/j.jacc.2012.01.001 vol. 59, no. 13, p. 1200, 2012.
- [8] R. O. Bonow *et al.*, "ACC/AHA 2006 Guidelines for the Management of Patients With Valvular Heart Disease," *Circulation*, 10.1161/CIRCULATIONAHA.106.176857 vol. 114, no. 5, p. e84, 2006.
- [9] M. Padala *et al.*, "An Engineering Review of Transcatheter Aortic Valve Technologies," (in English), *Cardiovasc Eng Tech*, vol. 1, no. 1, pp. 77-87, 2010/03/01 2010.
- [10] H. Mohammadi and K. Mequanint, "Prosthetic aortic heart valves: Modeling and design," *Medical Engineering & Physics*, vol. 33, no. 2, pp. 131-147, 3// 2011.
- [11] G. S. Bhuvaneshwar, C. V. Muraleedharan, A. V. Ramani, and M. S. Valiathan, "Evaluation of materials for artificial heart valves," (in English), *Bull. Mater. Sci.*, vol. 14, no. 6, pp. 1363-1374, 1991/12/01 1991.

- [12] P. Pibarot and J. G. Dumesnil, "Prosthetic heart valves: selection of the optimal prosthesis and long-term management," (in eng), *Circulation*, vol. 119, no. 7, pp. 1034-48, Feb 24 2009.
- [13] P. A. Ribeiro *et al.*, "Antiplatelet drugs and the incidence of thromboembolic complications of the St. Jude Medical aortic prosthesis in patients with rheumatic heart disease," (in eng), *The Journal of thoracic and cardiovascular surgery*, vol. 91, no. 1, pp. 92-8, Jan 1986.
- [14] B. Iung *et al.*, "Decision-making in elderly patients with severe aortic stenosis: why are so many denied surgery?," (in eng), *Eur Heart J*, vol. 26, no. 24, pp. 2714-20, Dec 2005.
- [15] A. Cribier *et al.*, "Percutaneous Transcatheter Implantation of an Aortic Valve Prosthesis for Calcific Aortic Stenosis," *First Human Case Description*, vol. 106, no. 24, pp. 3006-3008, 2002.
- [16] A. Cribier, "Development of transcatheter aortic valve implantation (TAVI): a 20-year odyssey," (in eng), *Arch Cardiovasc Dis*, vol. 105, no. 3, pp. 146-52, Mar 2012.
- [17] E. M. Wiegerinck, F. Van Kesteren, M. S. Van Mourik, M. M. Vis, and J. Baan, Jr., "An up-to-date overview of the most recent transcatheter implantable aortic valve prostheses," (in eng), *Expert Rev Med Devices*, vol. 13, no. 1, pp. 31-45, 2016.
- [18] A. Cribier *et al.*, "Percutaneous transcatheter implantation of an aortic valve prosthesis for calcific aortic stenosis: first human case description," (in eng), *Circulation*, vol. 106, no. 24, pp. 3006-8, Dec 10 2002.
- [19] J.-B. Masson *et al.*, "Transcatheter Aortic Valve Implantation Review of the Nature, Management, and Avoidance of Procedural Complications," *JACC: Cardiovascular Interventions*, vol. 2, no. 9, pp. 811-820, 2009.
- [20] P. Généreux *et al.*, "Paravalvular Leak After Transcatheter Aortic Valve Replacement The New Achilles' Heel? A Comprehensive Review of the Literature," *Journal of the American College of Cardiology*, vol. 61, no. 11, pp. 1125-1136, 2013.
- [21] P. C. Block, "Leaks and the "great ship" TAVI," (in eng), *Catheter Cardiovasc Interv*, vol. 75, no. 6, pp. 873-4, May 1 2010.
- [22] M. B. Leon, H. Gada, and G. P. Fontana, "Challenges and future opportunities for transcatheter aortic valve therapy," (in eng), *Prog Cardiovasc Dis*, vol. 56, no. 6, pp. 635-45, May-Jun 2014.
- [23] A. L. Bartorelli, D. Andreini, E. Sisillo, G. Tamborini, M. Fusari, and P. Biglioli, "Left main coronary artery occlusion after percutaneous aortic valve implantation," (in eng), *Ann Thorac Surg*, vol. 89, no. 3, pp. 953-5, Mar 2010.

- [24] K. Hayashida, E. Bouvier, and T. Lefèvre, "Successful Management of Annulus Rupture in Transcatheter Aortic Valve Implantation," *JACC: Cardiovascular Interventions*, vol. 6, no. 1, pp. 90-91, 2013.
- [25] K. Okuyama, H. Jilaihawi, and R. R. Makkar, "Leaflet length and left main coronary artery occlusion following transcatheter aortic valve replacement," (in eng), *Catheter Cardiovasc Interv*, vol. 82, no. 5, pp. E754-9, Nov 1 2013.
- [26] N. Saikrishnan, S. Gupta, and A. Yoganathan, "Hemodynamics of the Boston Scientific Lotus™ Valve: An In Vitro Study," (in English), *Cardiovasc Eng Tech*, vol. 4, no. 4, pp. 427-439, 2013/12/01 2013.
- [27] N. Piazza *et al.*, "First-in-human experience with the Medtronic CoreValve Evolut R," (in eng), *EuroIntervention*, vol. 9, no. 11, pp. 1260-3, Mar 20 2014.
- [28] J. Schofer *et al.*, "Prospective Multicenter Evaluation of the Direct Flow Medical Transcatheter Aortic Valve," *Journal of the American College of Cardiology*, vol. 63, no. 8, pp. 763-768, 2014.
- [29] P. S. Gunning, T. J. Vaughan, and L. M. McNamara, "Simulation of self expanding transcatheter aortic valve in a realistic aortic root: implications of deployment geometry on leaflet deformation," (in eng), *Ann Biomed Eng*, vol. 42, no. 9, pp. 1989-2001, Sep 2014.
- [30] S. Morganti, N. Brambilla, A. S. Petronio, A. Reali, F. Bedogni, and F. Auricchio, "Prediction of patient-specific post-operative outcomes of TAVI procedure: The impact of the positioning strategy on valve performance," *Journal of Biomechanics*, 2016.
- [31] F. Auricchio, M. Conti, S. Morganti, and A. Reali, "Simulation of transcatheter aortic valve implantation: a patient-specific finite element approach," *Computer Methods in Biomechanics and Biomedical Engineering*, vol. 17, no. 12, pp. 1347-1357, 2014/09/10 2014.
- [32] E. I. Charitos and H.-H. Sievers, "Anatomy of the aortic root: implications for valve-sparing surgery," *Annals of Cardiothoracic Surgery*, vol. 2, no. 1, pp. 53-56, 2013.
- [33] M. Misfeld and H.-H. Sievers, "Heart valve macro- and microstructure," *Philosophical Transactions of the Royal Society B: Biological Sciences*, vol. 362, no. 1484, pp. 1421-1436, 06/20 2007.
- [34] R. H. Anderson, J. Yanni, M. R. Boyett, N. J. Chandler, and H. Dobrzynski, "The anatomy of the cardiac conduction system," (in eng), *Clin Anat*, vol. 22, no. 1, pp. 99-113, Jan 2009.
- [35] T. Ioan, S. Horatiu, T. Brindusa, T. Cristina Maria, I. Mihaela, and S. Razvan Constantin, "Anatomy and Function of Normal Aortic Valvular Complex," 2013.

- [36] N. Piazza, P. de Jaegere, C. Schultz, A. E. Becker, P. W. Serruys, and R. H. Anderson, "Anatomy of the aortic valvar complex and its implications for transcatheter implantation of the aortic valve," (in eng), *Circulation. Cardiovascular interventions*, vol. 1, no. 1, pp. 74-81, Aug 2008.
- [37] N. Piazza *et al.*, "Early and persistent intraventricular conduction abnormalities and requirements for pacemaking after percutaneous replacement of the aortic valve," (in eng), *JACC. Cardiovascular interventions*, vol. 1, no. 3, pp. 310-6, Jun 2008.
- [38] C. Fraccaro *et al.*, "Incidence, Predictors, and Outcome of Conduction Disorders After Transcatheter Self-Expandable Aortic Valve Implantation," *The American Journal of Cardiology*, vol. 107, no. 5, pp. 747-754, 3/1/ 2011.
- [39] Q. Wang, S. Kodali, C. Primiano, and W. Sun, "Simulations of transcatheter aortic valve implantation: implications for aortic root rupture," (in eng), *Biomech Model Mechanobiol*, vol. 14, no. 1, pp. 29-38, Jan 2015.
- [40] Q. Wang, E. Sirois, and W. Sun, "Patient-specific modeling of biomechanical interaction in transcatheter aortic valve deployment," (in eng), *Journal of biomechanics*, vol. 45, no. 11, pp. 1965-71, Jul 26 2012.
- [41] C. Capelli *et al.*, "Patient-specific simulations of transcatheter aortic valve stent implantation," (in eng), *Medical & biological engineering & computing*, vol. 50, no. 2, pp. 183-92, Feb 2012.
- [42] W. Sun, K. Li, and E. Sirois, "Simulated elliptical bioprosthetic valve deformation: Implications for asymmetric transcatheter valve deployment," *Journal of Biomechanics*, vol. 43, no. 16, pp. 3085-3090, 12/1/ 2010.
- [43] E. Sirois, Q. Wang, and W. Sun, "Fluid Simulation of a Transcatheter Aortic Valve Deployment into a Patient-Specific Aortic Root," (in English), *Cardiovasc Eng Tech*, vol. 2, no. 3, pp. 186-195, 2011/09/01 2011.
- [44] G. Rocatello *et al.*, "Patient-Specific Computer Simulation to Elucidate the Role of Contact Pressure in the Development of New Conduction Abnormalities After Catheter-Based Implantation of a Self-Expanding Aortic Valve," (in eng), *Circ Cardiovasc Interv*, vol. 11, no. 2, p. e005344, Feb 2018.
- [45] H. A. Dwyer, P. B. Matthews, A. Azadani, L. Ge, T. S. Guy, and E. E. Tseng, "Migration forces of transcatheter aortic valves in patients with noncalcific aortic insufficiency," (in eng), *J Thorac Cardiovasc Surg*, vol. 138, no. 5, pp. 1227-33, Nov 2009.

- [46] J. Mummert, E. Sirois, and W. Sun, "Quantification of Biomechanical Interaction of Transcatheter Aortic Valve Stent Deployed in Porcine and Ovine Hearts," *Ann Biomed Eng*, vol. 41, no. 3, pp. 577-86, Mar 2013.
- [47] A. Colombo and A. Latib, "Left Bundle Branch Block After Transcatheter Aortic Valve Implantation Inconsequential or a Clinically Important Endpoint?**, " *Journal of the American College of Cardiology*, vol. 60, no. 18, pp. 1753-1755, 2012.
- [48] V. Calvi *et al.*, "Incidence rate and predictors of permanent pacemaker implantation after transcatheter aortic valve implantation with self-expanding CoreValve prosthesis," (in Eng), *J Interv Card Electrophysiol*, vol. 34, no. 2, pp. 189-95, Aug 2012.
- [49] P. Houthuizen *et al.*, "Left bundle-branch block induced by transcatheter aortic valve implantation increases risk of death," (in eng), *Circulation*, vol. 126, no. 6, pp. 720-8, Aug 7 2012.
- [50] R.-J. Nuis *et al.*, "Timing and potential mechanisms of new conduction abnormalities during the implantation of the Medtronic CoreValve System in patients with aortic stenosis," *European Heart Journal*, vol. 32, no. 16, pp. 2067-2074, 2011.
- [51] K. Wilczek, R. Reguła, K. Bujak, P. Chodór, M. Długaszek, and M. Gaşior, "Conduction disturbances after transcatheter aortic valve implantation procedures – predictors and management," in *Postepy Kardiol Interwencyjnej*, vol. 12no. 3), 2016, pp. 203-11.
- [52] J. I. Hoffman and S. Kaplan, "The incidence of congenital heart disease," (in eng), *J Am Coll Cardiol*, vol. 39, no. 12, pp. 1890-900, Jun 19 2002.
- [53] C. Ward, "Clinical significance of the bicuspid aortic valve," *Heart*, 10.1136/heart.83.1.81 vol. 83, no. 1, p. 81, 2000.
- [54] R. S. Hira *et al.*, "Trends and Outcomes of Off-label Use of Transcatheter Aortic Valve Replacement: Insights From the NCDR STS/ACC TVT Registry," (in eng), *JAMA Cardiol*, vol. 2, no. 8, pp. 846-854, Aug 1 2017.
- [55] Z.-G. Zhao, H. Jilaihawi, Y. Feng, and M. Chen, "Transcatheter aortic valve implantation in bicuspid anatomy," *Nat Rev Cardiol*, Perspectives vol. 12, no. 2, pp. 123-128, 02//print 2015.
- [56] M. B. Leon *et al.*, "Transcatheter Aortic-Valve Implantation for Aortic Stenosis in Patients Who Cannot Undergo Surgery," *New England Journal of Medicine*, vol. 363, no. 17, pp. 1597-1607, 2010/10/21 2010.
- [57] J. Jose, G. Richardt, and M. Abdel Wahab, "Balloon- Or Self-Expandable TAVI: Clinical Equipoise?," *Interventional Cardiology Review*, vol. 10, pp. 103-108, 2015.
- [58] S.-H. Yoon, R. R. Makkar, and FACC, "TAVR for Severe Bicuspid Aortic Valve Stenosis," *Journal of American College of Cardiology*, 2018.

- [59] A. W. Chan, D. Wong, and J. Charania, "Transcatheter Aortic Valve Replacement in Bicuspid Aortic Stenosis Using Lotus Valve System," (in eng), *Catheter Cardiovasc Interv*, vol. 90, no. 1, pp. 157-163, Jul 2017.
- [60] K. B. Chandran, Rittgers, S. E., & Yoganathan, A. P., *Biofluid mechanics: The human circulation*. Boca Raton, FL: CRC/Taylor & Francis, 2007.
- [61] D. J. Schneck and J. D. Bronzino, D. J. Schneck, Ed. *Biomechanics: principles and applications*. Boca Raton, FL: CRC Press, 2002.
- [62] M. J. Thubrikar, *The Aortic Valve*. Taylor & Francis, 1989.
- [63] S. Y. Ho, "Structure and anatomy of the aortic root," (in eng), *European journal of echocardiography : the journal of the Working Group on Echocardiography of the European Society of Cardiology*, vol. 10, no. 1, pp. i3-10, Jan 2009.
- [64] M. Z. Khawaja *et al.*, "Permanent Pacemaker Insertion After CoreValve Transcatheter Aortic Valve Implantation," *Circulation*, 10.1161/CIRCULATIONAHA.109.927152 vol. 123, no. 9, p. 951, 2011.
- [65] B. J. Bellhouse and F. H. Bellhouse, "Mechanism of closure of the aortic valve," (in eng), *Nature*, vol. 217, no. 5123, pp. 86-7, Jan 6 1968.
- [66] C. Schmidtke *et al.*, "First clinical results with the new sinus prosthesis used for valve-sparing aortic root replacement," (in eng), *European journal of cardio-thoracic surgery : official journal of the European Association for Cardio-thoracic Surgery*, vol. 43, no. 3, pp. 585-90, Mar 2013.
- [67] J. A. Stella and M. S. Sacks, "On the Biaxial Mechanical Properties of the Layers of the Aortic Valve Leaflet," *Journal of Biomechanical Engineering*, vol. 129, no. 5, pp. 757-766, 2007.
- [68] I. Vesely and R. Noseworthy, "Micromechanics of the fibrosa and the ventricularis in aortic valve leaflets," (in eng), *J Biomech*, vol. 25, no. 1, pp. 101-13, Jan 1992.
- [69] M. S. Sacks, W. David Merryman, and D. E. Schmidt, "On the biomechanics of heart valve function," *Journal of Biomechanics*, vol. 42, no. 12, pp. 1804-1824, 8/25/ 2009.
- [70] N. M. Rajamannan *et al.*, "Calcific Aortic Valve Disease: Not Simply a Degenerative Process," *Circulation*, 10.1161/CIRCULATIONAHA.110.006767 vol. 124, no. 16, p. 1783, 2011.
- [71] F. J. Schoen and R. J. Levy, "Tissue heart valves: Current challenges and future research perspectives," *Journal of Biomedical Materials Research*, vol. 47, no. 4, pp. 439-465, 1999.
- [72] N. Saikrishnan, C.-H. Yap, N. C. Milligan, N. V. Vasilyev, and A. P. Yoganathan, "In Vitro Characterization of Bicuspid Aortic Valve Hemodynamics Using Particle Image Velocimetry," *Annals of Biomedical Engineering*, journal article vol. 40, no. 8, pp. 1760-1775, 2012.

- [73] M. S. Sacks and A. P. Yoganathan, "Heart valve function: a biomechanical perspective," (in eng), *Philosophical transactions of the Royal Society of London. Series B, Biological sciences*, vol. 362, no. 1484, pp. 1369-91, Aug 29 2007.
- [74] A. P. Yoganathan, Z. He, and S. Casey Jones, "Fluid mechanics of heart valves," (in eng), *Annual review of biomedical engineering*, vol. 6, pp. 331-62, 2004.
- [75] S. Chandra, N. M. Rajamannan, and P. Sucusky, "Computational assessment of bicuspid aortic valve wall-shear stress: implications for calcific aortic valve disease," (in eng), *Biomech Model Mechanobiol*, vol. 11, no. 7, pp. 1085-96, Sep 2012.
- [76] G. Pisani *et al.*, "Role of the sinuses of Valsalva on the opening of the aortic valve," (in eng), *J Thorac Cardiovasc Surg*, vol. 145, no. 4, pp. 999-1003, Apr 2013.
- [77] C. H. Yap, H. S. Kim, K. Balachandran, M. Weiler, R. Haj-Ali, and A. P. Yoganathan, "Dynamic deformation characteristics of porcine aortic valve leaflet under normal and hypertensive conditions," (in eng), *Am J Physiol Heart Circ Physiol*, vol. 298, no. 2, pp. H395-405, Feb 2010.
- [78] K. Balachandran, P. Sucusky, and A. P. Yoganathan, "Hemodynamics and mechanobiology of aortic valve inflammation and calcification," (in eng), *Int J Inflam*, vol. 2011, p. 263870, 2011.
- [79] M. Thubrikar, L. P. Bosher, and S. P. Nolan, "The mechanism of opening of the aortic valve," (in eng), *J Thorac Cardiovasc Surg*, vol. 77, no. 6, pp. 863-70, Jun 1979.
- [80] M. Weiler, C. H. Yap, K. Balachandran, M. Padala, and A. P. Yoganathan, "Regional analysis of dynamic deformation characteristics of native aortic valve leaflets," (in eng), *J Biomech*, vol. 44, no. 8, pp. 1459-65, May 17 2011.
- [81] R. L. Osnabrugge *et al.*, "Aortic stenosis in the elderly: disease prevalence and number of candidates for transcatheter aortic valve replacement: a meta-analysis and modeling study," (in eng), *J Am Coll Cardiol*, vol. 62, no. 11, pp. 1002-12, Sep 10 2013.
- [82] N. Saikrishnan, G. Kumar, F. J. Sawaya, S. Lerakis, and A. P. Yoganathan, "Accurate assessment of aortic stenosis: a review of diagnostic modalities and hemodynamics," (in eng), *Circulation*, vol. 129, no. 2, pp. 244-53, Jan 14 2014.
- [83] B. A. Carabello, "Clinical practice. Aortic stenosis," (in eng), *The New England journal of medicine*, vol. 346, no. 9, pp. 677-82, Feb 28 2002.
- [84] B. A. Carabello and W. J. Paulus, "Aortic stenosis," (in eng), *Lancet (London, England)*, vol. 373, no. 9667, pp. 956-66, Mar 14 2009.

- [85] V. T. Nkomo, J. M. Gardin, T. N. Skelton, J. S. Gottdiener, C. G. Scott, and M. Enriquez-Sarano, "Burden of valvular heart diseases: a population-based study," *The Lancet*, vol. 368, no. 9540, pp. 1005-1011, //.
- [86] M. R. Dweck, N. A. Boon, and D. E. Newby, "Calcific aortic stenosis: a disease of the valve and the myocardium," (in eng), *Journal of the American College of Cardiology*, vol. 60, no. 19, pp. 1854-63, Nov 6 2012.
- [87] N. M. Rajamannan *et al.*, "Human aortic valve calcification is associated with an osteoblast phenotype," (in eng), *Circulation*, vol. 107, no. 17, pp. 2181-4, May 6 2003.
- [88] K. D. O'Brien, D. D. Reichenbach, S. M. Marcovina, J. Kuusisto, C. E. Alpers, and C. M. Otto, "Apolipoproteins B, (a), and E accumulate in the morphologically early lesion of 'degenerative' valvular aortic stenosis," (in eng), *Arteriosclerosis, thrombosis, and vascular biology*, vol. 16, no. 4, pp. 523-32, Apr 1996.
- [89] R. O. Bonow *et al.*, "2008 Focused update incorporated into the ACC/AHA 2006 guidelines for the management of patients with valvular heart disease: a report of the American College of Cardiology/American Heart Association Task Force on Practice Guidelines (Writing Committee to Revise the 1998 Guidelines for the Management of Patients With Valvular Heart Disease): endorsed by the Society of Cardiovascular Anesthesiologists, Society for Cardiovascular Angiography and Interventions, and Society of Thoracic Surgeons," (in eng), *Circulation*, vol. 118, no. 15, pp. e523-661, Oct 7 2008.
- [90] C. A. Hufnagel, W. P. Harvey, P. J. Rabil, and D. T. Mc, "Surgical correction of aortic insufficiency," (in eng), *Surgery*, vol. 35, no. 5, pp. 673-83, May 1954.
- [91] J. M. Campbell, "An artificial aortic valve; preliminary report," (in eng), *The Journal of thoracic surgery*, vol. 19, no. 2, pp. 312-8, Feb 1950.
- [92] W. Y. Lim, G. Lloyd, and S. Bhattacharyya, "Mechanical and surgical bioprosthetic valve thrombosis," *Heart*, 10.1136/heartjnl-2017-311856 vol. 103, no. 24, p. 1934, 2017.
- [93] C. W. Akins, "Mechanical cardiac valvular prostheses," *The Annals of Thoracic Surgery*, vol. 52, no. 1, pp. 161-172, 7// 1991.
- [94] K. E. Hammermeister, G. K. Sethi, W. G. Henderson, C. Oprian, T. Kim, and S. Rahimtoola, "A Comparison of Outcomes in Men 11 Years after Heart-Valve Replacement with a Mechanical Valve or Bioprosthesis," *New England Journal of Medicine*, vol. 328, no. 18, pp. 1289-1296, 1993/05/06 1993.
- [95] A. Yoganathan, P., "Cardiac Valve Prostheses," 1995.
- [96] P. Johansen, "Mechanical heart valve cavitation," (in eng), *Expert review of medical devices*, vol. 1, no. 1, pp. 95-104, Sep 2004.

- [97] F. Nistal *et al.*, "In vivo experimental assessment of polytetrafluoroethylene trileaflet heart valve prosthesis," (in eng), *The Journal of thoracic and cardiovascular surgery*, vol. 99, no. 6, pp. 1074-81, Jun 1990.
- [98] S. H. Daebritz *et al.*, "Introduction of a flexible polymeric heart valve prosthesis with special design for aortic position," (in eng), *European journal of cardio-thoracic surgery : official journal of the European Association for Cardio-thoracic Surgery*, vol. 25, no. 6, pp. 946-52, Jun 2004.
- [99] L. P. Dasi, H. A. Simon, P. Sucusky, and A. P. Yoganathan, "FLUID MECHANICS OF ARTIFICIAL HEART VALVES," *Clinical and experimental pharmacology & physiology*, vol. 36, no. 2, pp. 225-237, 2009.
- [100] A. Carpentier, G. Lemaigre, L. Robert, S. Carpentier, and C. Dubost, "Biological factors affecting long-term results of valvular heterografts," (in eng), *J Thorac Cardiovasc Surg*, vol. 58, no. 4, pp. 467-83, Oct 1969.
- [101] J. Ennker, A. Albert, and I. C. Ennker, "Stentless aortic valves. Current aspects," *HSR Proceedings in Intensive Care & Cardiovascular Anesthesia*, vol. 4, no. 2, pp. 77-82, 2012.
- [102] A. Kulik *et al.*, "Mechanical versus bioprosthetic valve replacement in middle-aged patients," (in eng), *Eur J Cardiothorac Surg*, vol. 30, no. 3, pp. 485-91, Sep 2006.
- [103] Z. A. Khan, J. Aji, A. Soomro, S. Malik, W. Saeed, and M. R. Sardar, "When we should say no to TAVR—Defining the line between utility and futility," *Cardiovascular Revascularization Medicine*, vol. 17, no. 6, pp. 424-427, 9// 2016.
- [104] J. Carroll *et al.*, "Relationship between procedure volume and outcome for transcatheter aortic valve replacement in U.S," *Clinical practice: insights from the STS/ACC TVT registry, ACC Sci Sess (2016)*, 2016.
- [105] B. Ramlawi, J. E. Anaya-Ayala, and M. J. Reardon, "Transcatheter Aortic Valve Replacement (TAVR): Access Planning and Strategies," *Methodist DeBakey Cardiovascular Journal*, vol. 8, no. 2, pp. 22-25, Apr-Jun 2012.
- [106] J. Sinning *et al.*, "Next-generation transcatheter heart valves improve clinical outcomes in patients undergoing TAVI," *EuroIntervention*, 2016.
- [107] J.-M. Sinning *et al.*, "TCTAP A-161 Comparison of Next Generation Transcatheter Heart Valves: Angiographic, Echocardiographic and Hemodynamic Evaluation of an Extended All-comers Study Cohort Using the Dimensionless Aortic Regurgitation Index," *Journal of the American College of Cardiology*, 10.1016/j.jacc.2017.03.208 vol. 69, no. 16 Supplement, p. S85, 2017.

- [108] J.-M. Paradis, M. Del Trigo, R. Puri, and J. Rodés-Cabau, "Transcatheter Valve-in-Valve and Valve-in-Ring for Treating Aortic and Mitral Surgical Prosthetic Dysfunction," *Journal of the American College of Cardiology*, 10.1016/j.jacc.2015.09.015 vol. 66, no. 18, p. 2019, 2015.
- [109] L. Nombela-Franco *et al.*, "Predictive factors, efficacy, and safety of balloon post-dilation after transcatheter aortic valve implantation with a balloon-expandable valve," (in eng), *JACC Cardiovasc Interv*, vol. 5, no. 5, pp. 499-512, May 2012.
- [110] M. B. Leon *et al.*, "Transcatheter Aortic-Valve Implantation for Aortic Stenosis in Patients Who Cannot Undergo Surgery," *New England Journal of Medicine*, vol. 363, no. 17, pp. 1597-1607, 2010.
- [111] C. R. Smith *et al.*, "Transcatheter versus Surgical Aortic-Valve Replacement in High-Risk Patients," *New England Journal of Medicine*, vol. 364, no. 23, pp. 2187-2198, 2011/06/09 2011.
- [112] E. Van Belle, "Perivalvular aortic regurgitation: the main determinant of 1-year mortality after a successful TAVI procedure—insights from the FRANCE 2 Registry.," in *EuroPCR*, Paris, France, 2012.
- [113] S. Lerakis, S. S. Hayek, and P. S. Douglas, "Paravalvular Aortic Leak After Transcatheter Aortic Valve Replacement," *Circulation*, 10.1161/CIRCULATIONAHA.112.142000 vol. 127, no. 3, p. 397, 2013.
- [114] S. K. Kodali *et al.*, "Two-Year Outcomes after Transcatheter or Surgical Aortic-Valve Replacement," *New England Journal of Medicine*, vol. 366, no. 18, pp. 1686-1695, 2012.
- [115] A. Unbehaun *et al.*, "Transapical Aortic Valve Implantation: Incidence and Predictors of Paravalvular Leakage and Transvalvular Regurgitation in a Series of 358 Patients," *Journal of the American College of Cardiology*, vol. 59, no. 3, pp. 211-221, 1/17/ 2012.
- [116] M. Gotzmann *et al.*, "Long-term outcome of patients with moderate and severe prosthetic aortic valve regurgitation after transcatheter aortic valve implantation," (in eng), *Am J Cardiol*, vol. 110, no. 10, pp. 1500-6, Nov 15 2012.
- [117] J. M. Sinning *et al.*, "Aortic regurgitation index defines severity of peri-prosthetic regurgitation and predicts outcome in patients after transcatheter aortic valve implantation," (in eng), *J Am Coll Cardiol*, vol. 59, no. 13, pp. 1134-41, Mar 27 2012.
- [118] C. Tamburino *et al.*, "<div xmlns=<http://www.w3.org/1999/xhtml>" xmlns:hwp=<http://schema.highwire.org/Journal>">Incidence and Predictors of Early and Late Mortality After Transcatheter Aortic Valve Implantation in 663 Patients With Severe Aortic Stenosis<span hwp:id="article-title-30"

- class="sub-article-title">Clinical Perspective</div>," *Circulation*, vol. 123, no. 3, pp. 299-308, 2011.
- [119] M. Abdel-Wahab *et al.*, "Aortic regurgitation after transcatheter aortic valve implantation: incidence and early outcome. Results from the German transcatheter aortic valve interventions registry," (in eng), *Heart*, vol. 97, no. 11, pp. 899-906, Jun 2011.
- [120] K. Hayashida *et al.*, "Sex-related differences in clinical presentation and outcome of transcatheter aortic valve implantation for severe aortic stenosis," (in eng), *J Am Coll Cardiol*, vol. 59, no. 6, pp. 566-71, Feb 7 2012.
- [121] N. E. Moat *et al.*, "Long-term outcomes after transcatheter aortic valve implantation in high-risk patients with severe aortic stenosis: the U.K. TAVI (United Kingdom Transcatheter Aortic Valve Implantation) Registry," (in eng), *J Am Coll Cardiol*, vol. 58, no. 20, pp. 2130-8, Nov 8 2011.
- [122] B. E. Stähli, W. Maier, R. Corti, T. F. Lüscher, R. Jenni, and F. C. Tanner, "Aortic regurgitation after transcatheter aortic valve implantation: mechanisms and implications," *Cardiovascular Diagnosis and Therapy*, vol. 3, no. 1, pp. 15-22, 2013.
- [123] T. A. Fairbairn *et al.*, "Diffusion-weighted MRI determined cerebral embolic infarction following transcatheter aortic valve implantation: assessment of predictive risk factors and the relationship to subsequent health status," (in eng), *Heart*, vol. 98, no. 1, pp. 18-23, Jan 2012.
- [124] P. Kahlert *et al.*, "Silent and apparent cerebral ischemia after percutaneous transfemoral aortic valve implantation: a diffusion-weighted magnetic resonance imaging study," (in eng), *Circulation*, vol. 121, no. 7, pp. 870-8, Feb 23 2010.
- [125] J. Rodes-Cabau *et al.*, "Cerebral embolism following transcatheter aortic valve implantation: comparison of transfemoral and transapical approaches," (in eng), *J Am Coll Cardiol*, vol. 57, no. 1, pp. 18-28, Jan 4 2011.
- [126] H. Eggebrecht, A. Schermund, T. Voigtlander, P. Kahlert, R. Erbel, and R. H. Mehta, "Risk of stroke after transcatheter aortic valve implantation (TAVI): a meta-analysis of 10,037 published patients," (in eng), *EuroIntervention*, vol. 8, no. 1, pp. 129-38, May 15 2012.
- [127] L. Nombela-Franco *et al.*, "Timing, predictive factors, and prognostic value of cerebrovascular events in a large cohort of patients undergoing transcatheter aortic valve implantation," (in eng), *Circulation*, vol. 126, no. 25, pp. 3041-53, Dec 18 2012.

- [128] L. Rivard *et al.*, "Electrocardiographic and electrophysiological predictors of atrioventricular block after transcatheter aortic valve replacement," *Heart Rhythm*, vol. 12, no. 2, pp. 321-329, 2// 2015.
- [129] J. Baan Jr *et al.*, "Factors associated with cardiac conduction disorders and permanent pacemaker implantation after percutaneous aortic valve implantation with the CoreValve prosthesis," *American Heart Journal*, vol. 159, no. 3, pp. 497-503, 3// 2010.
- [130] L. Roten *et al.*, "Incidence and Predictors of Atrioventricular Conduction Impairment After Transcatheter Aortic Valve Implantation," *The American Journal of Cardiology*, vol. 106, no. 10, pp. 1473-1480, 11/15/ 2010.
- [131] H. B. Ribeiro *et al.*, "Predictive Factors, Management, and Clinical Outcomes of Coronary Obstruction Following Transcatheter Aortic Valve Implantation Insights From a Large Multicenter Registry," *Journal of the American College of Cardiology*, vol. 62, no. 17, pp. 1552-1562, 2013.
- [132] H. B. Ribeiro *et al.*, "Coronary Obstruction Following Transcatheter Aortic Valve Implantation: A Systematic Review," *JACC: Cardiovascular Interventions*, vol. 6, no. 5, pp. 452-461, 5// 2013.
- [133] K. Hayashida *et al.*, "Potential mechanism of annulus rupture during transcatheter aortic valve implantation," (in eng), *Catheter Cardiovasc Interv*, vol. 82, no. 5, pp. E742-6, Nov 1 2013.
- [134] M. Pasic *et al.*, "Rupture of the device landing zone during transcatheter aortic valve implantation: a life-threatening but treatable complication," (in eng), *Circ Cardiovasc Interv*, vol. 5, no. 3, pp. 424-32, Jun 2012.
- [135] M. Barbanti *et al.*, "Anatomical and procedural features associated with aortic root rupture during balloon-expandable transcatheter aortic valve replacement," (in eng), *Circulation*, vol. 128, no. 3, pp. 244-53, Jul 16 2013.
- [136] E. E. Tseng, A. Wisneski, A. N. Azadani, and L. Ge, "Engineering perspective on transcatheter aortic valve implantation," *Interventional Cardiology*, vol. 5, no. 1, pp. 53-70, 2013.
- [137] S. Tzamtzis, J. Viquerat, J. Yap, M. J. Mullen, and G. Burriesci, "Numerical analysis of the radial force produced by the Medtronic-CoreValve and Edwards-SAPIEN after transcatheter aortic valve implantation (TAVI)," *Medical Engineering & Physics*, vol. 35, no. 1, pp. 125-130, 1// 2013.
- [138] C. J. Schultz *et al.*, "Geometry and Degree of Apposition of the CoreValve ReValving System With Multislice Computed Tomography After Implantation in Patients With Aortic Stenosis," *Journal of the American College of Cardiology*, vol. 54, no. 10, pp. 911-918, 9/1/ 2009.
- [139] P. S. Gunning, N. Saikrishnan, L. M. McNamara, and A. P. Yoganathan, "An in vitro evaluation of the impact of eccentric deployment on

- transcatheter aortic valve hemodynamics," (in eng), *Ann Biomed Eng*, vol. 42, no. 6, pp. 1195-206, Jun 2014.
- [140] R. P. Gooley, J. D. Cameron, and I. T. Meredith, "Assessment of the Geometric Interaction Between the Lotus Transcatheter Aortic Valve Prosthesis and the Native Ventricular Aortic Interface by 320-Multidetector Computed Tomography," *JACC: Cardiovascular Interventions*, vol. 8, no. 5, pp. 740-749, 4/27/ 2015.
- [141] R. Zegdi *et al.*, "Is it reasonable to treat all calcified stenotic aortic valves with a valved stent? Results from a human anatomic study in adults," (in eng), *J Am Coll Cardiol*, vol. 51, no. 5, pp. 579-84, Feb 5 2008.
- [142] R. K. Binder *et al.*, "Transcatheter Aortic Valve Replacement With a New Self-Expanding Transcatheter Heart Valve and Motorized Delivery System," *JACC: Cardiovascular Interventions*, vol. 6, no. 3, pp. 301-307, 3// 2013.
- [143] A. B. Willson *et al.*, "Transcatheter Aortic Valve Replacement With the St. Jude Medical Portico ValveFirst-in-Human Experience," *Journal of the American College of Cardiology*, vol. 60, no. 7, pp. 581-586, 2012.
- [144] P. S. Gunning, N. Saikrishnan, A. P. Yoganathan, and L. M. McNamara, "Total ellipse of the heart valve: the impact of eccentric stent distortion on the regional dynamic deformation of pericardial tissue leaflets of a transcatheter aortic valve replacement," *J R Soc Interface*, vol. 12, no. 113, p. 20150737, Dec 06 2015.
- [145] G. van Nooten, S. Ozaki, P. Herijgers, P. Segers, P. Verdonck, and W. Flameng, "Distortion of the stentless porcine valve induces accelerated leaflet fibrosis and calcification in juvenile sheep," (in eng), *J Heart Valve Dis*, vol. 8, no. 1, pp. 34-41, Jan 1999.
- [146] M. J. Mack *et al.*, "Patient Selection for Transcatheter Aortic Valve Replacement," *Journal of the American College of Cardiology*, vol. 62, no. 17_S, 2013.
- [147] *CARDIOVASCULAR IMPLANTS - CARDIAC VALVE PROSTHESES - PART 2: SURGICALLY IMPLANTED HEART VALVE SUBSTITUTES (ISO 5840-2:2015)*, 2015.
- [148] M. Raffel, C. Willert, S. T. Wereley, and J. Kompenhans, "Particle Image Velocimetry A Practical Guide Second Edition Preface," in *Particle Image Velocimetry: a Practical Guide, Second Edition* (Experimental Fluid Mechanics. Berlin: Springer-Verlag Berlin, 2007, pp. V-+.
- [149] S. Stuhle *et al.*, "In-vitro investigation of the hemodynamics of the Edwards Sapien transcatheter heart valve," (in Eng), *J Heart Valve Dis*, vol. 20, no. 1, pp. 53-63, Jan 2011.

- [150] A. Ducci, S. Tzamtzis, M. J. Mullen, and G. Burriesci, "Hemodynamics in the Valsalva sinuses after transcatheter aortic valve implantation (TAVI)," (in Eng), *J Heart Valve Dis*, vol. 22, no. 5, pp. 688-96, Sep 2013.
- [151] M. Scharfschwerdt, R. Meyer-Saraei, C. Schmidtke, and H.-H. Sievers, "Hemodynamics of the Edwards Sapien XT transcatheter heart valve in noncircular aortic annuli," *The Journal of Thoracic and Cardiovascular Surgery*, vol. 148, no. 1, pp. 126-132, 7// 2014.
- [152] M. Kuetting *et al.*, "In vitro assessment of the influence of aortic annulus ovality on the hydrodynamic performance of self-expanding transcatheter heart valve prostheses," *Journal of Biomechanics*, vol. 47, no. 5, pp. 957-965, 3/21/ 2014.
- [153] E. M. Groves, A. Falahatpisheh, J. L. Su, and A. Kheradvar, "The Effects of Positioning of Transcatheter Aortic Valve on Fluid Dynamics of the Aortic Root," *ASAIO journal (American Society for Artificial Internal Organs : 1992)*, vol. 60, no. 5, pp. 545-552, Sep-Oct 2014.
- [154] FDA, "Reporting of Computational Modeling Studies in Medical Device Submissions - Draft Guidance for Industry and Food and Drug Administration Staff," 2014.
- [155] P. Schoenhagen, A. Hill, T. Kelley, Z. Popovic, and S. S. Halliburton, "In vivo imaging and computational analysis of the aortic root. Application in clinical research and design of transcatheter aortic valve systems," (in eng), *J Cardiovasc Transl Res*, vol. 4, no. 4, pp. 459-69, Aug 2011.
- [156] K. Li and W. Sun, "Simulated Thin Pericardial Bioprosthetic Valve Leaflet Deformation Under Static Pressure-Only Loading Conditions: Implications for Percutaneous Valves," *Annals of Biomedical Engineering*, vol. 38, no. 8, pp. 2690-2701, 2010// 2010.
- [157] A. N. Smuts, D. C. Blaine, C. Scheffer, H. Weich, A. F. Doubell, and K. H. Dellimore, "Application of finite element analysis to the design of tissue leaflets for a percutaneous aortic valve," *Journal of the Mechanical Behavior of Biomedical Materials*, vol. 4, no. 1, pp. 85-98, 1// 2011.
- [158] R. K. Binder *et al.*, "Impact of Post-Implant SAPIEN XT Geometry and Position on Conduction Disturbances, Hemodynamic Performance, and Paravalvular Regurgitation," *JACC: Cardiovascular Interventions*, vol. 6, no. 5, pp. 462-468, 5// 2013.
- [159] M. Abbasi and A. N. Azadani, "Leaflet stress and strain distributions following incomplete transcatheter aortic valve expansion," *Journal of Biomechanics*, vol. 48, no. 13, pp. 3663-3671, 10/15/ 2015.
- [160] C. Martin and W. Sun, "Modeling of long-term fatigue damage of soft tissue with stress softening and permanent set effects," (in English),

- Biomech Model Mechanobiol*, vol. 12, no. 4, pp. 645-655, 2013/08/01 2013.
- [161] C. Martin and W. Sun, "Simulation of long-term fatigue damage in bioprosthetic heart valves: effects of leaflet and stent elastic properties," (in eng), *Biomech Model Mechanobiol*, vol. 13, no. 4, pp. 759-70, Aug 2014.
- [162] C. Martin and W. Sun, "Comparison of transcatheter aortic valve and surgical bioprosthetic valve durability: A fatigue simulation study," *Journal of Biomechanics*, vol. 48, no. 12, pp. 3026-3034, 9/18/ 2015.
- [163] C. Martin and W. Sun, "Transcatheter Valve Underexpansion Limits Leaflet Durability: Implications for Valve-in-Valve Procedures," *Annals of Biomedical Engineering*, pp. 1-11, 2016// 2016.
- [164] R. Gurvitch *et al.*, "Transcatheter valve-in-valve implantation for failed surgical bioprosthetic valves," (in Eng), *J Am Coll Cardiol*, vol. 58, no. 21, pp. 2196-209, Nov 15 2011.
- [165] J. Bailey, N. Curzen, and N. W. Bressloff, "The impact of imperfect frame deployment and rotational orientation on stress within the prosthetic leaflets during transcatheter aortic valve implantation," *Journal of Biomechanics*, vol. 53, pp. 22-28, 2017/02/28/ 2017.
- [166] J. Bailey, N. Curzen, and N. W. Bressloff, "Assessing the impact of including leaflets in the simulation of TAVI deployment into a patient-specific aortic root," *Computer Methods in Biomechanics and Biomedical Engineering*, vol. 19, no. 7, pp. 733-744, 2016/05/18 2016.
- [167] S. Schievano, C. Capelli, A. M. Taylor, and P. Bonhoeffer, "Application of computational simulations for percutaneous pulmonary valve implantation: (Percutaneous pulmonary valve computer analysis)," *Progress in Pediatric Cardiology*, vol. 30, no. 1-2, pp. 15-21, 12// 2010.
- [168] S. Schievano *et al.*, "Patient specific finite element analysis results in more accurate prediction of stent fractures: Application to percutaneous pulmonary valve implantation," *Journal of Biomechanics*, vol. 43, no. 4, pp. 687-693, 3/3/ 2010.
- [169] M. Gessat, L. Altwegg, T. Frauenfelder, A. Plass, and V. Falk, "Cubic Hermite Bezier spline based reconstruction of implanted aortic valve stents from CT images," (in eng), *Conf Proc IEEE Eng Med Biol Soc*, vol. 2011, pp. 2667-70, 2011.
- [170] M. Gessat *et al.*, "Image-based mechanical analysis of stent deformation: concept and exemplary implementation for aortic valve stents," (in eng), *IEEE Trans Biomed Eng*, vol. 61, no. 1, pp. 4-15, Jan 2014.
- [171] M. Bianchi *et al.*, "Effect of Balloon-Expandable Transcatheter Aortic Valve Replacement Positioning: A Patient-Specific Numerical Model," *Artificial Organs*, vol. 40, no. 12, pp. E292-E304, 2016.

- [172] F. Sturla *et al.*, "Impact of different aortic valve calcification patterns on the outcome of transcatheter aortic valve implantation: A finite element study," *Journal of Biomechanics*.
- [173] S. Morganti *et al.*, "Simulation of transcatheter aortic valve implantation through patient-specific finite element analysis: Two clinical cases," *Journal of Biomechanics*, vol. 47, no. 11, pp. 2547-2555, 8/22/ 2014.
- [174] C. Russ *et al.*, "Simulation of transcatheter aortic valve implantation under consideration of leaflet calcification," (in eng), *Conf Proc IEEE Eng Med Biol Soc*, vol. 2013, pp. 711-4, 2013.
- [175] S. Grbic *et al.*, "Image-based computational models for TAVI planning: from CT images to implant deployment," (in eng), *Med Image Comput Comput Assist Interv*, vol. 16, no. Pt 2, pp. 395-402, 2013.
- [176] A. Finotello, S. Morganti, and F. Auricchio, "Finite element analysis of TAVI: Impact of native aortic root computational modeling strategies on simulation outcomes," *Medical Engineering & Physics*, vol. 47, pp. 2-12, 2017/09/01/ 2017.
- [177] T. Walther, J. Blumenstein, A. van Linden, and J. Kempfert, "Contemporary management of aortic stenosis: surgical aortic valve replacement remains the gold standard," (in eng), *Heart*, vol. 98 Suppl 4, pp. iv23-9, Nov 2012.
- [178] B. Iung *et al.*, "A prospective survey of patients with valvular heart disease in Europe: The Euro Heart Survey on Valvular Heart Disease," (in eng), *Eur Heart J*, vol. 24, no. 13, pp. 1231-43, Jul 2003.
- [179] C. Cao, S. C. Ang, M. P. Vallely, M. Ng, M. Adams, and M. Wilson, "Migration of the transcatheter valve into the left ventricle," *Annals of Cardiothoracic Surgery*, vol. 1, no. 2, pp. 243-244, 06/20/received 07/19/accepted 2012.
- [180] R. J. Hunter, Y. Liu, Y. Lu, W. Wang, and R. J. Schilling, "Left Atrial Wall Stress Distribution and Its Relationship to Electrophysiologic Remodeling in Persistent Atrial Fibrillation," *Circulation: Arrhythmia and Electrophysiology*, 10.1161/CIRCEP.111.965541 vol. 5, no. 2, p. 351, 2012.
- [181] F. Auricchio, R. L. Taylor, and J. Lubliner, "Shape-memory alloys: macromodelling and numerical simulations of the superelastic behavior," *Computer Methods in Applied Mechanics and Engineering*, vol. 146, no. 3-4, pp. 281-312, 7/15/ 1997.
- [182] F. Auricchio and R. L. Taylor, "Shape-memory alloys: modelling and numerical simulations of the finite-strain superelastic behavior," *Computer Methods in Applied Mechanics and Engineering*, vol. 143, no. 1-2, pp. 175-194, 4/15/ 1997.

- [183] R. W. Ogden and D. G. Roxburgh, "A pseudo-elastic model for the Mullins effect in filled rubber," *Proceedings of the Royal Society of London. Series A: Mathematical, Physical and Engineering Sciences*, 10.1098/rspa.1999.0431 vol. 455, no. 1988, p. 2861, 1999.
- [184] C. Martin, T. Pham, and W. Sun, "Significant differences in the material properties between aged human and porcine aortic tissues," (in eng), *Eur J Cardiothorac Surg*, vol. 40, no. 1, pp. 28-34, Jul 2011.
- [185] H. M. Loree, A. J. Grodzinsky, S. Y. Park, L. J. Gibson, and R. T. Lee, "Static circumferential tangential modulus of human atherosclerotic tissue," (in eng), *J Biomech*, vol. 27, no. 2, pp. 195-204, Feb 1994.
- [186] I. Pericevic, C. Lally, D. Toner, and D. J. Kelly, "The influence of plaque composition on underlying arterial wall stress during stent expansion: The case for lesion-specific stents," *Medical Engineering & Physics*, vol. 31, no. 4, pp. 428-433, 5// 2009.
- [187] C. Conway, F. Sharif, J. P. McGarry, and P. E. McHugh, "A Computational Test-Bed to Assess Coronary Stent Implantation Mechanics Using a Population-Specific Approach," *Cardiovascular Engineering and Technology*, vol. 3, no. 4, pp. 374-387, 2012// 2012.
- [188] P. Gunning, S.,.
- [189] A. M. Kasel *et al.*, "Standardized Imaging for Aortic Annular Sizing Implications for Transcatheter Valve Selection," *JACC: Cardiovascular Imaging*, vol. 6, no. 2, pp. 249-262, 2013.
- [190] H. Zahedmanesh, D. John Kelly, and C. Lally, "Simulation of a balloon expandable stent in a realistic coronary artery—Determination of the optimum modelling strategy," *Journal of Biomechanics*, vol. 43, no. 11, pp. 2126-2132, 8/10/ 2010.
- [191] M.-C. Hsu and Y. Bazilevs, "Blood vessel tissue prestress modeling for vascular fluid-structure interaction simulation," *Finite Elements in Analysis and Design*, vol. 47, no. 6, pp. 593-599, 2011/06/01/ 2011.
- [192] M. Urena *et al.*, "Predictive factors and long-term clinical consequences of persistent left bundle branch block following transcatheter aortic valve implantation with a balloon-expandable valve," (in Eng), *J Am Coll Cardiol*, vol. 60, no. 18, pp. 1743-52, Oct 30 2012.
- [193] J. Baan, Jr. *et al.*, "Factors associated with cardiac conduction disorders and permanent pacemaker implantation after percutaneous aortic valve implantation with the CoreValve prosthesis," (in eng), *Am Heart J*, vol. 159, no. 3, pp. 497-503, Mar 2010.
- [194] A. Vahanian *et al.*, "Transcatheter valve implantation for patients with aortic stenosis: a position statement from the European Association of Cardio-Thoracic Surgery (EACTS) and the European Society of Cardiology (ESC), in collaboration with the European Association of

- Perc..., " *European Heart Journal*, vol. 29, no. 11, pp. 1463-1470, 2008-06-01 00:00:00 2008.
- [195] M. Haensig and A. J. Rastan, "Aortic valve calcium load before tavi: Is it important?," *Annals of Cardiothoracic Surgery*, vol. 1, no. 2, pp. 160-164, 2012.
- [196] A. Reinders, C. S. de Vries, and G. Joubert, *Pre-interventional assessment and calcification score of the aortic valve and annulus, with multi-detector CT, in transcatheter aortic valve implantation (TAVI) using the Medtronic CoreValve* (2015, no. 1). 2015.
- [197] A. W. Leber *et al.*, "Aortic valve calcium score as a predictor for outcome after TAVI using the CoreValve revalving system," (in eng), *Int J Cardiol*, vol. 166, no. 3, pp. 652-7, Jul 1 2013.
- [198] D. Wendt *et al.*, "In vitro results of a new minimally invasive aortic valve resecting tool," (in eng), *Eur J Cardiothorac Surg*, vol. 35, no. 4, pp. 622-7; discussion 627, Apr 2009.
- [199] M. Seiffert *et al.*, "Device landing zone calcification and its impact on residual regurgitation after transcatheter aortic valve implantation with different devices," *European Heart Journal - Cardiovascular Imaging*, vol. 17, no. 5, pp. 576-584, 2016.
- [200] S. Vad, A. Eskinazi, T. Corbett, T. McGloughlin, and J. P. Vande Geest, "Determination of Coefficient of Friction for Self-Expanding Stent-Grafts," *Journal of Biomechanical Engineering*, vol. 132, no. 12, pp. 121007-121007, 2010.
- [201] M. A. Cavero, J. Goicolea, C. García-Montero, and J. F. Oteo, "Prognostic Implications of Asymmetric Morphology in Transcatheter Aortic Valve Implantation: a Case Report," *Revista Española de Cardiología (English Edition)*, 10.1016/j.rec.2011.04.002 vol. 65, no. 01, pp. 104-105, 2012.
- [202] J. G. Webb *et al.*, "Transcatheter Aortic Valve Implantation," *Circulation*, 10.1161/CIRCULATIONAHA.108.837807 vol. 119, no. 23, p. 3009, 2009.
- [203] T. D. Yan *et al.*, "Transcatheter aortic valve implantation for high-risk patients with severe aortic stenosis: A systematic review," (in eng), *J Thorac Cardiovasc Surg*, vol. 139, no. 6, pp. 1519-28, Jun 2010.
- [204] R. Moreno *et al.*, "Cause of complete atrioventricular block after percutaneous aortic valve implantation: insights from a necropsy study," (in eng), *Circulation*, vol. 120, no. 5, pp. e29-30, Aug 4 2009.
- [205] A. Sinhal *et al.*, "Atrioventricular Block After Transcatheter Balloon Expandable Aortic Valve Implantation," *JACC: Cardiovascular Interventions*, vol. 1, no. 3, pp. 305-309, 2008.
- [206] Abaqus, *Abaqus Theory Manual*. Dassault Systèmes, 2014.

- [207] W. C. Roberts, "The congenitally bicuspid aortic valve," *The American Journal of Cardiology*, vol. 26, no. 1, pp. 72-83, 1970/07/01 1970.
- [208] C. Basso *et al.*, "An echocardiographic survey of primary school children for bicuspid aortic valve," (in eng), *Am J Cardiol*, vol. 93, no. 5, pp. 661-3, Mar 01 2004.
- [209] E. Tutar, F. Ekici, S. Atalay, and N. Nacar, "The prevalence of bicuspid aortic valve in newborns by echocardiographic screening," (in eng), *Am Heart J*, vol. 150, no. 3, pp. 513-5, Sep 2005.
- [210] S. Nistri, C. Basso, C. Marzari, P. Mormino, and G. Thiene, "Frequency of bicuspid aortic valve in young male conscripts by echocardiogram," (in eng), *Am J Cardiol*, vol. 96, no. 5, pp. 718-21, Sep 01 2005.
- [211] W. C. Roberts and J. M. Ko, "Frequency by Decades of Unicuspid, Bicuspid, and Tricuspid Aortic Valves in Adults Having Isolated Aortic Valve Replacement for Aortic Stenosis, With or Without Associated Aortic Regurgitation," *Circulation*, 10.1161/01.CIR.0000155623.48408.C5 vol. 111, no. 7, p. 920, 2005.
- [212] W. C. Roberts, K. G. Janning, J. M. Ko, G. Filardo, and G. J. Matter, "Frequency of Congenitally Bicuspid Aortic Valves in Patients ≥ 80 Years of Age Undergoing Aortic Valve Replacement for Aortic Stenosis (With or Without Aortic Regurgitation) and Implications for Transcatheter Aortic Valve Implantation," *The American Journal of Cardiology*, vol. 109, no. 11, pp. 1632-1636, 6/1/ 2012.
- [213] C. J. O'Sullivan and S. Windecker, "Implications of Bicuspid Aortic Valves for Transcatheter Aortic Valve Implantation," *Circulation: Cardiovascular Interventions*, 10.1161/CIRCINTERVENTIONS.113.000461 vol. 6, no. 3, p. 204, 2013.
- [214] M. J. Reardon *et al.*, "Surgical or Transcatheter Aortic-Valve Replacement in Intermediate-Risk Patients," *New England Journal of Medicine*, vol. 376, no. 14, pp. 1321-1331, 2017/04/06 2017.
- [215] M. B. Leon *et al.*, "Transcatheter or Surgical Aortic-Valve Replacement in Intermediate-Risk Patients," *New England Journal of Medicine*, vol. 374, no. 17, pp. 1609-1620, 2016/04/28 2016.
- [216] K. Phan, S. Wong, S. Phan, H. Ha, P. Qian, and T. D. Yan, "Transcatheter Aortic Valve Implantation (TAVI) in Patients With Bicuspid Aortic Valve Stenosis – Systematic Review and Meta-Analysis," *Heart, Lung and Circulation*, vol. 24, no. 7, pp. 649-659, 7// 2015.
- [217] R. Zegdi, D. Blanchard, A. Azarine, T. Folliguet, and J. N. Fabiani, "Elliptical shape of a SAPIEN XT prosthesis deployed in a patient with bicuspid aortic valve stenosis," (in eng), *J Heart Valve Dis*, vol. 21, no. 6, pp. 764-6, Nov 2012.

- [218] P. T. L. Chiam *et al.*, "Percutaneous Transcatheter Heart Valve Implantation in a Bicuspid Aortic Valve," *JACC: Cardiovascular Interventions*, 10.1016/j.jcin.2009.11.024 vol. 3, no. 5, p. 559, 2010.
- [219] R. Zegdi *et al.*, "Increased radial force improves stent deployment in tricuspid but not in bicuspid stenotic native aortic valves," (in eng), *Ann Thorac Surg*, vol. 89, no. 3, pp. 768-72, Mar 2010.
- [220] N. Wijesinghe *et al.*, "Transcatheter aortic valve implantation in patients with bicuspid aortic valve stenosis," (in eng), *JACC Cardiovasc Interv*, vol. 3, no. 11, pp. 1122-5, Nov 2010.
- [221] D. Himbert *et al.*, "Feasibility and outcomes of transcatheter aortic valve implantation in high-risk patients with stenotic bicuspid aortic valves," (in eng), *Am J Cardiol*, vol. 110, no. 6, pp. 877-83, Sep 15 2012.
- [222] S. C. Siu and C. K. Silversides, "Bicuspid Aortic Valve Disease," *Journal of the American College of Cardiology*, vol. 55, no. 25, pp. 2789-2800, 6/22/ 2010.
- [223] T. Bauer *et al.*, "Comparison of the Effectiveness of Transcatheter Aortic Valve Implantation in Patients With Stenotic Bicuspid Versus Tricuspid Aortic Valves (from the German TAVI Registry)," *The American Journal of Cardiology*, vol. 113, no. 3, pp. 518-521, 2/1/ 2014.
- [224] C. Costopoulos *et al.*, "Comparison of results of transcatheter aortic valve implantation in patients with severely stenotic bicuspid versus tricuspid or nonbicuspid valves," (in eng), *Am J Cardiol*, vol. 113, no. 8, pp. 1390-3, Apr 15 2014.
- [225] G. Y. Perlman *et al.*, "Bicuspid Aortic Valve Stenosis: Favorable Early Outcomes With a Next-Generation Transcatheter Heart Valve in a Multicenter Study," (in eng), *JACC Cardiovasc Interv*, vol. 9, no. 8, pp. 817-824, Apr 25 2016.
- [226] S. H. Yoon *et al.*, "Transcatheter Aortic Valve Replacement With Early- and New-Generation Devices in Bicuspid Aortic Valve Stenosis," (in eng), *J Am Coll Cardiol*, vol. 68, no. 11, pp. 1195-1205, Sep 13 2016.
- [227] W. C. Roberts and J. M. Ko, "Frequency by decades of unicuspid, bicuspid, and tricuspid aortic valves in adults having isolated aortic valve replacement for aortic stenosis, with or without associated aortic regurgitation," (in eng), *Circulation*, vol. 111, no. 7, pp. 920-5, Feb 22 2005.
- [228] D. R. Holmes, Jr. *et al.*, "2012 ACCF/AATS/SCAI/STS expert consensus document on transcatheter aortic valve replacement," (in eng), *J Am Coll Cardiol*, vol. 59, no. 13, pp. 1200-54, Mar 27 2012.
- [229] T. Kilic and I. Yilmaz, "Transcatheter aortic valve implantation: a revolution in the therapy of elderly and high-risk patients with severe aortic stenosis," in *J Geriatr Cardiol*, vol. 14no. 3), 2017, pp. 204-17.

- [230] R. Gooley, P. R. Antonis, and I. T. Meredith, "The Lotus transcatheter aortic valve: a next-generation repositionable, resheathable and recapturable prosthesis," *Interventional Cardiology*, vol. 6, no. 4, pp. 357 - 365, 2014.
- [231] O. M. McGee, P. S. Gunning, A. McNamara, and L. M. McNamara, "The impact of implantation depth of the Lotus™ valve on mechanical stress in close proximity to the bundle of His," *Biomechanics and Modeling in Mechanobiology*, 2018/08/20 2018.
- [232] G. A. Holzapfel, "Nonlinear Solid Mechanics: A Continuum Approach for Engineering.," ed: Wiley, 2000.
- [233] P. E. McHugh and O. M. D., "Finite Element Methods: Fundamentals and Applications in Biomedical Engineering," in *Topics in Biomedical Engineering*, E. P. P.J and P.E. McHugh, Ed., 2004.
- [234] F. J. Harewood and P. E. McHugh, "Comparison of the implicit and explicit finite element methods using crystal plasticity," *Computational Materials Science*, vol. 39, no. 2, pp. 481-494, 2007/04/01/ 2007.
- [235] S. H. Choi, "Simulation of stored energy and orientation gradients in cold-rolled interstitial free steels," *Acta Materialia*, vol. 51, no. 6, pp. 1775-1788, 2003/04/02/ 2003.
- [236] W. J. Chung, J. W. Cho, and T. Belytschko, "On the dynamic effects of explicit FEM in sheet metal forming analysis," *Engineering Computations*, vol. 15, no. 6, pp. 750-776, 1998/09/01 1998.

Appendix I: Theoretical Framework

A.1 Introduction

This chapter provides an outline of the finite element theory and the theoretical basis used in the computational models developed in Chapters 3, 5 and 6 of this Thesis.

A.2 Notation

This section provides a clarification of the notation used in this chapter. Capital letters are used to signify tensors and matrices while vectors are denoted using lowercase letters. Bold typeface font is given to vectors, tensors and matrices with their components being shown in italics. The use of the Roman italic symbol with Roman subscript i referred to as index notation is used to simply represent a manipulation of these quantities, where a repeated index denotes summation. A coordinate system with three axes x_1 , x_2 and x_3 , can be represented by x_i where $i=1,2,3$. The e_i are known as basis vectors that define coordinate axes and are defined as $e_1(1,0,0)$, $e_2(0,1,0)$ and $e_3(0,0,1)$. A demonstration of indicial notation can be demonstrated using the dot product (scalar product), a summation of the component parts of two vectors in 3D (\mathbf{u}, \mathbf{v}).

$$\mathbf{u} \cdot \mathbf{v} = u_i v_i = u_1 v_1 + u_2 v_2 + u_3 v_3 \quad (1.1)$$

Second order tensors have 9 components in 3D and are a product of two vectors. In general, they are linear vector functions. Each component in the 2nd order tensor is

denoted by two subscripts defining the components location in the tensor. In a second order tensor A component A_{ij} is located in row i and column j . Stress and strain are examples of second order tensors. Fourth order tensors are linear tensor functions of second order tensors. For example the fourth order tensor of linear elasticities, C , relating the second order tensors of stress and strain, whereby:

$$\boldsymbol{\sigma} = \mathbf{C} : \boldsymbol{\varepsilon} \quad (1.2)$$

$$\sigma_{ij} = C_{ijkl} \varepsilon_{kl} \quad (1.3)$$

A.3 Finite Element Analysis of Solid Structures

A.3.1 Fundamental Principles and Theoretical Formulations

Large deformation kinematics describes the deformation of a body from an initial undeformed (reference) configuration to a deformed (current) configuration. This can be seen in Figure A.1 where \boldsymbol{x} is the position of the material point in the reference configuration and \boldsymbol{y} is the position of the material point in the current configuration.

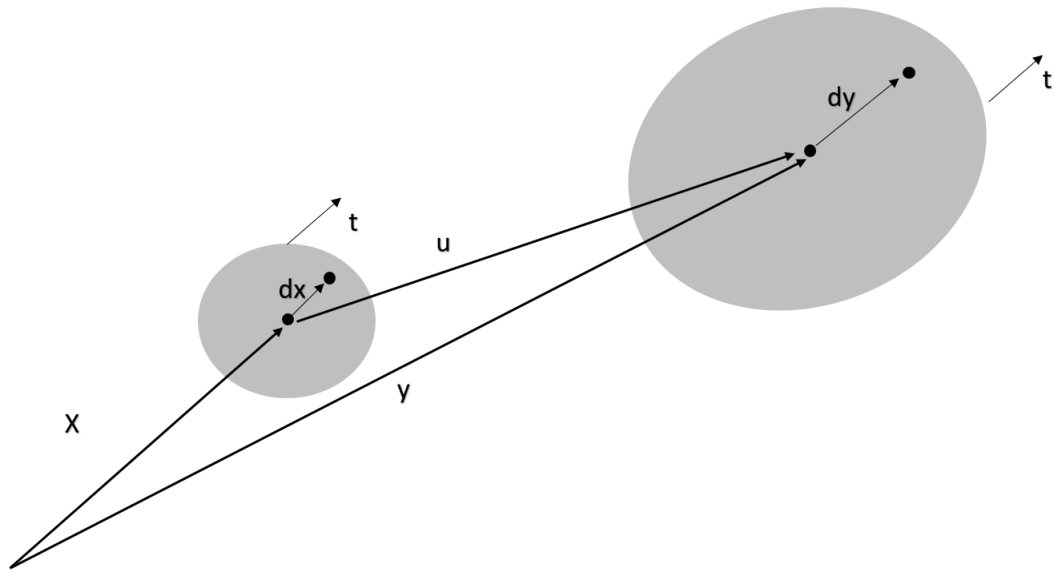


Figure A.1: Illustration of finite element deformation mechanics.

\mathbf{u} is the displacement vector of the material point, where:

$$\mathbf{u}(\mathbf{x}, t) = \mathbf{y}(\mathbf{x}, t) - \mathbf{x} \quad (1.4)$$

\mathbf{v} is the velocity vector which is found by differentiating \mathbf{u} with respect to time t :

$$d\mathbf{u} = \mathbf{v}(\mathbf{x}, t) = \frac{\partial \mathbf{u}}{\partial t} \quad (1.5)$$

The 2nd order tensor \mathbf{F} is known as the deformation gradient and relates the deformation between the two neighbouring material points, it can be defined as:

$$d\mathbf{y} = \mathbf{F} \cdot d\mathbf{x} \quad (1.6)$$

$$\mathbf{F} = \frac{\partial \mathbf{y}}{\partial \mathbf{x}} \quad (1.7)$$

The determinant of \mathbf{F} , J , is known as the Jacobian and is the ratio of volume change that occurs during deformation from the reference to the deformed configuration.

$$J = \det(\mathbf{F}) \quad (1.8)$$

Strain is a measure of the changes in the distance of two neighbouring particles. The Green strain tensor, \mathbf{E} , also known as the Lagrangian strain tensor, measures large 3D deformations where:

$$\mathbf{E} = \frac{1}{2}(\mathbf{F}^T\mathbf{F} - \mathbf{I}) \quad (1.9)$$

where T denotes the transpose and \mathbf{I} is a second order tensor identity tensor such that for a second order tensor \mathbf{A} , $\mathbf{AI} = \mathbf{A}$.

Using the polar decomposition for the deformation gradient \mathbf{F} we may form two one point symmetric tensors; the left (\mathbf{B}) and right (\mathbf{C}) Cauchy-Green tensors, measures of deformation:

$$\mathbf{B} = \mathbf{FF}^T \quad (1.10)$$

$$\mathbf{C} = \mathbf{F}^T\mathbf{F} \quad (1.11)$$

The left and right Cauchy tensor have the same first three principal invariants which can be identified as:

$$I_1 = \text{tr}(\mathbf{C}) = \lambda_1^2 + \lambda_2^2 + \lambda_3^2 \quad (1.12)$$

$$I_2 = [I_1^2 - \text{tr}(\mathbf{C}^2)] = \lambda_1^2\lambda_2^2 + \lambda_2^2\lambda_3^2 + \lambda_3^2\lambda_1^2 \quad (1.13)$$

$$I_3 = \det(\mathbf{C}) = [\text{def}(\mathbf{F})]^2 = J^2 = \lambda_1^2\lambda_2^2\lambda_3^2 \quad (1.14)$$

where λ is stretch.

Where F is a second order Cartesian tensor with a determinant greater than zero. There exist unique positive definite symmetric tensors U and V and a unique proper orthogonal tensor R that can be defined by:

$$F = RU = VR \quad (1.15)$$

where

$$V^2 = B = FF^T \quad (1.16)$$

$$U^2 = C = F^T F \quad (1.17)$$

The spatial velocity gradient L can also be derived from the deformation gradient:

$$L = \dot{F}F^{-1} \quad (1.18)$$

where F describes the change in length and orientation between to neighbouring points and L describes the rate of these changes. L can be decomposed into D a symmetric rate of deformation tensor and W an asymmetric spin tensor.

$$L = D + W \quad (1.19)$$

D measures the rate at which line elements change their square lengths. W is the body spin and can be interpreted as the rate of rotation.

$$D = \frac{1}{2}(L + L^T) \quad (1.20)$$

$$W = (L - L^T) \quad (1.21)$$

The Cauchy (true) stress tensor $\boldsymbol{\sigma}$ is a second order tensor that gives force per unit area on the current configuration. It linearly relates the traction force \boldsymbol{t} (force per unit area) on a surface to the unit normal vector to the surface, \boldsymbol{n} :

$$\boldsymbol{t} = \boldsymbol{\sigma} \boldsymbol{n} \quad (1.22)$$

The Cauchy stress tensor has both a hydrostatic pressure, p , responsible for volume change, and a deviatoric stress, \boldsymbol{S} , responsible for shape change:

$$p = \frac{\text{tr}(\boldsymbol{\sigma})}{3} \quad (1.23)$$

$$\boldsymbol{t} = \boldsymbol{S} - p\boldsymbol{I} \quad (1.24)$$

The eigenvalues of the Cauchy stress tensor are known as the principal stresses. While $\boldsymbol{\sigma}$ measures the force per unit deformed area, the nominal stress tensor (engineering stress), $\tilde{\boldsymbol{\sigma}}$, measures the force per unit reference area can be defined as :

$$\tilde{\boldsymbol{\sigma}} = J\boldsymbol{F}^{-1}\boldsymbol{\sigma} \quad (1.25)$$

The mean von Mises stress which is an output examined in Chapters 3, 5 and 6 of this thesis can be defined as:

$$\sigma_e = \sqrt{\frac{3}{2}S_{ij}S_{ij}} \quad (1.26)$$

Two other important stress tensors; the Kirchhoff stress tensor (symmetric), $\boldsymbol{\tau}$, and the second Piola-Kirchhoff stress tensor, \boldsymbol{T} ,(symmetric) can be defined as:

$$\boldsymbol{\tau} = J\boldsymbol{\sigma} \quad (1.27)$$

$$\boldsymbol{T} = J\boldsymbol{F}^{-1}\boldsymbol{\sigma}(\boldsymbol{F}^{-1})^T \quad (1.28)$$

This section provides a brief overview of the fundamental principles of deformation kinematics. A more in-depth description can be found at Abaqus Theory Manual [206] and Holzapfel [232].

A.3.2 Finite Element Method

The software Abaqus is used in Chapter 3,5 and 6 of this Thesis to solve boundary value problems. Abaqus uses a finite element method to solve constitutive equations of material under different boundary conditions. Boundary Value Problems (BVP) require that for a given body at a given point in time its complete mechanical state can be determined. This is done using the equilibrium equation, the constitutive equation and the compatibility equation together forming a set of partial differential equations, combining these PDE with the boundary conditions we are given a BVP that can be solved [233].

A.3.2.1 The Principle of Virtual Work

The principle of virtual work (PVW) is an expression of conservation of energy that can be written on either the reference or deformed configuration. In rate form, it is known as the principle of virtual power [233]. The virtual work statement can be physically interpreted as “the rate of work done by the external forces subjected to any

virtual velocity field is equal to the rate of work done by the equilibrating stresses on the rate of deformation of the same virtual velocity field” [206].

The PVW in its rate form is expressed as:

$$\delta W = \int_V (\nabla \boldsymbol{\sigma} - \mathbf{f}\mathbf{u}) \cdot \delta \mathbf{v} dV = 0 \quad (1.29)$$

where δW is the virtual work per unit volume, $\delta \mathbf{v}$ is the virtual velocity field, V is the volume of body β . This can be separated into internal and external virtual power:

$$\int_V \boldsymbol{\sigma} : \delta \boldsymbol{\varepsilon} dV = \int_V \mathbf{f} \cdot \delta \mathbf{u} dV + \int_S \mathbf{t} \cdot \delta \mathbf{u} dS \quad (1.30)$$

Where S is the surface of body β . $\boldsymbol{\sigma}$ is the stress vector, \mathbf{f} is the body force vector and \mathbf{t} is the surface traction vector. $\delta \boldsymbol{\varepsilon}$ and $\delta \mathbf{u}$ are the virtual strain and displacement vectors respectively. In the case of no body forces we can say:

$$\int_V \boldsymbol{\sigma} : \delta \boldsymbol{\varepsilon} dV = \int_S \mathbf{t} \cdot \delta \mathbf{u} dS \quad (1.31)$$

The Finite Element Method (FEM) is based upon the principle of virtual work.

A given body is discretized into sections called elements these elements are interconnected through points called nodes. This collection of elements and nodes is referred to as a finite element mesh.

For element e in a given mesh we can say:

$$\delta \mathbf{u} = \mathbf{N}_e \delta \mathbf{u}_e \quad (1.32)$$

$$\delta \boldsymbol{\varepsilon} = \mathbf{B}_e \delta \mathbf{u}_e \quad (1.33)$$

Where N_e is the shape function matrix and B_e is the shape function gradient matrix.

The PVW then becomes:

$$\sum_e \int_V \delta \mathbf{u}_e^T \mathbf{B}_e^T \boldsymbol{\sigma} dV = \sum_e \int_{S_2} \delta \mathbf{u}_e^T \mathbf{N}^T \mathbf{t} dS \quad (1.34)$$

Where the summation is over all the elements “e” in the mesh. Performing the summation, which essentially means assembling elemental quantities into global quantities and eliminating the arbitrary virtual fields yields the following global expression:

$$\int_V \mathbf{B}^T \boldsymbol{\sigma} dV = \int_S \mathbf{N}^T \mathbf{t} dS \quad (1.35)$$

Where the left-hand side is now the global internal force vector and the right-hand side is now the external force vector. These equations can be assembled to create the balance force vector \mathbf{G} , at any point in time, \mathbf{G} should be equal to zero:

$$\mathbf{G}(\mathbf{u}) = \int_V \mathbf{B}^T \boldsymbol{\sigma}(\mathbf{u}) dV - \int_S \mathbf{N}^T \mathbf{t} dS = 0 \quad (1.36)$$

where \mathbf{u} is the global nodal displacement vector of the mesh.

A.3.2.2 *Implicit Method*

The finite element software used in this thesis, Abaqus (Simulia, Providence, Rhode Island), uses two different numerical approaches Implicit and Explicit in solving equation 1.36. In Abaqus/Standard a series of implicit solution procedures are available. In the case of static structural problems, a form of the Newton-Raphson method is used to iteratively solve equation 1.36. Given a solution at time t , and looking for the solution at time $t+\Delta t$, an initial estimate is made for the solution at time $t+\Delta t$. Using the Newton-Raphson iterations with incremental steps the problem is solved iteratively until convergence is achieved at all nodal displacements using:

$$\mathbf{u}_{i+1}^{t+\Delta t} = \mathbf{u}_i^{t+\Delta t} - \left[\frac{\partial \mathbf{G}(\mathbf{u}_i^{t+\Delta t})}{\partial \mathbf{u}} \right]^{-1} \cdot \mathbf{G}(\mathbf{u}_i^{t+\Delta t}) \quad (1.37)$$

where t is the start time of the increment, Δt is the magnitude of the time increment, $\mathbf{u}_i^{t+\Delta t}$ is the initial estimate of nodal displacements and is then used as an approximation for the next iteration, $\mathbf{u}_{i+1}^{t+\Delta t}$.

The solution converges when \mathbf{G} is less than a specified tolerance. The Newton-Raphson method solves the equation iteratively allowing for the boundary conditions to be applied incrementally giving an accurate solution. However, in cases where there the solution contains highly non-linear materials or where there is contact and sliding between two surfaces many iterations are needed to solve a given increment and leading to the need for progressively smaller time steps. If large nonlinearities are encounter convergence can be difficult to achieve within a practical timeframe. The explicit method does not involve iteration; therefore, convergence is not an issue. In

Chapters 3, 5 and 6 of this thesis, Abaqus/Explicit was used to solve complex contact problems involving large deformations.

A.3.2.3 Explicit Method

Abaqus/Explicit uses an explicit dynamic analysis that is based upon the explicit integration rule combine with “lumped” mass matrices [206]. For the explicit solution method accelerations and velocities at a given point in time, t , are assumed constant and are used to solve for the next point in time. The explicit method is not iterative like implicit FEM which makes it more conducive when working with large deformations as convergence problems don't arise when modelling highly non-linear responses and contact between irregularly shaped surfaces. Abaqus/Explicit integrates the equations of motion for the body using the central difference integration rule:

$$\mathbf{u}^{(i+1)} = \mathbf{u}^{(i)} + \Delta t^{(i+1)} \dot{\mathbf{u}}^{(i+\frac{1}{2})} \quad (1.38)$$

$$\dot{\mathbf{u}}^{(i+\frac{1}{2})} = \dot{\mathbf{u}}^{(i-\frac{1}{2})} + \frac{\Delta t^{(i+1)} + \Delta t^i}{2} \ddot{\mathbf{u}}^{(i)} \quad (1.39)$$

where $\dot{\mathbf{u}}$ is velocity and $\ddot{\mathbf{u}}$ is acceleration, the superscript i is the increment number with $i - \frac{1}{2}$ and $i + \frac{1}{2}$ referring to mid-incremental values. The central difference operator predicts the kinematic state using known $\dot{\mathbf{u}}^{(i-\frac{1}{2})}$ and $\ddot{\mathbf{u}}^i$ values from the previous increment [206]. Unlike the implicit method i is not an increment number within a certain time increment, i in the explicit method refers to the time increment number. Nodal accelerations are computed at the start of each increment using:

$$\ddot{\mathbf{u}}^i = \mathbf{M}^{-1}(\mathbf{F}^i - \mathbf{I}^i) \quad (1.40)$$

where \mathbf{M} is the lumped mass matrix:

$$\mathbf{M}^i = \int_V \rho \mathbf{N} dV \quad (1.41)$$

and \mathbf{I}^i is the vector of internal element forces given by:

$$\mathbf{I}^i = \int_V \mathbf{B}^T \boldsymbol{\sigma}^i dV \quad (1.42)$$

and is the vector of externally applied forces.

$$\mathbf{F}^i = \int_S \mathbf{N}^T \mathbf{t}^i dS + \int_V \mathbf{N}^T \mathbf{P}^i dV \quad (1.43)$$

which means equation 1.41 can be written as:

$$\begin{aligned} \ddot{\mathbf{u}} &= \mathbf{M}^{-1} \left(- \int_V \mathbf{B}^T \boldsymbol{\sigma}^n(\mathbf{u}) dV + \int_S \mathbf{N}^T \mathbf{t}^n dS \right) u_{n+1}^{t+\Delta t} \\ &= u_n^{t+\Delta t} - \left[\frac{d\mathbf{G}(u_n^{t+\Delta t})}{du} \right] \cdot \mathbf{G}(u_n^{t+\Delta t}) \end{aligned} \quad (1.44)$$

The lumped mass matrix \mathbf{M} is diagonalised and can be inverted easily which leads to efficiency in solving each time increment. Although an incremental solution is easy to obtain using the explicit method using a quasi-static analysis can often take large numbers of increments to solve a minute time point. The minimum stable time increment is dependent on the edge length of the smallest element and the dilatational wave speed which can be expressed in terms of the material moduli and density. Therefore, during a quasi-static analysis, it should be ensured element size is regular so as not to increase the time due to one small element. Therefore, it is often impractical to run a quasi-static solution on its true timescale. Mass scaling is a method that is used to reduce the time scale. This is where the density of the materials are

artificially increased resulting in an increase in the stable time increment. An increase in the material density by a factor of f^2 leads to a reduction by a factor of f in the runtime [206, 234]. In order to prevent unrealistic dynamic results during a quasi-static, it is important to ensure internal forces do not affect the solution, therefore, the total internal strain energy should remain below 5-10% in order to ensure inertial forces do not affect the mechanical response of the materials modelled [235, 236].

A.3.3 Constitutive Models

In Chapters 3, 5 and 6 of this thesis, the commercial finite element solver Abaqus 3.13 is used to solve complex continuum mechanics problems. Constitutive models are mathematical descriptions of the response of a material to an external stimulus (e.g. displacement, force etc.). The constitutive models implemented in the methods of this thesis describe the material behaviour of the aortic sinus, the ascending aorta, calcification, leaflet tissue and the nitinol stent frame. Further information on the theoretical framework can be found in can be found at Abaqus Theory Manual [206].

A.3.3.1 Hyperelastic Constitutive Models

This section describes the constitutive behaviour of hyperelastic materials in the context of an isotropic response. In this thesis, hyperelastic material models are used to describe the aortic sinus and ascending aorta. Typically, hyperelastic materials cannot be described using linear stress-strain response. Therefore, a strain energy potential, U , is used to describe the material behaviour. U , defines the strain energy stored per unit reference volume as a function of deformation. The polynomial strain energy potential is given by:

$$U = \sum_{i+j=1}^N C_{ij}(\bar{I}_1 - 3)(\bar{I}_2 - 3) + \sum_{i=1}^N \frac{1}{D_i} (J^{el} - 1)^{2i} \quad (1.45)$$

Where C_{ij} and D_i are material constants, J^{el} is the elastic volume ratio, \bar{I}_1 and \bar{I}_2 are the first and second invariants respectively, and N determine the number of terms in the polynomial. For more information see the Abaqus Theory Manual [206]. In Chapter 3 of this thesis, the calcifications were modelled using a third order Mooney-Rivlin hyperelastic material model

$$U = C_{10}(I_3 - 3) + C_{01}(I_2 - 3) + C_{20}(I_1 - 3)^2 + C_{11}(I_1 - 3)(I_2 - 3) + C_{30}(I_1 - 3)^3 \quad (1.46)$$

The ascending aorta and the aortic sinus were modelled using the first order Ogden model [183] whose strain energy can be defined by:

$$U = \frac{2\mu_i}{\alpha_i^2} \left(\lambda_1^{-\alpha_i} + \lambda_2^{-\alpha_i} + \lambda_3^{-\alpha_i} - 3 \right) + \frac{1}{D_i} (J^{el} - 1)^{2i} \quad (1.47)$$

where μ_i are α_i material parameters.

A.3.3.2 Nitinol Constitutive Model

Nitinol is a shape memory alloy and exhibits superelastic material properties. Nitinol was modelled using a superelastic material model. An Abaqus 6.13 inbuilt user subroutine (VUMAT), based on the Auricchio and Taylor model, was used in assigning the superelastic properties [181, 182]. The theory is based on general plasticity whereby the change in strain, $\Delta\varepsilon$, is described by:

$$\Delta\varepsilon = \Delta\varepsilon^{el} + \Delta\varepsilon^{tr} \quad (1.48)$$

where, $\Delta\varepsilon^{el}$, is the linear elastic strain component and, $\Delta\varepsilon^{tr}$, is a transfemoral strain component.

The transformation from the austenite phase to the martensite phase occurs between a range of stresses (σ_{tL}^S to σ_{tL}^E) determined by characteristic specific to the alloy, the transformation component is defined by:

$$\Delta\varepsilon^{tr} = \alpha\Delta\zeta \frac{\delta F}{\delta \sigma} \quad (1.49)$$

$$F^S \leq F \leq F^E \quad (1.50)$$

where α is a scalar denoting the upper limit of the martensite detwinning deformation, ζ is the martensite fraction, and F is the transformation potential. The reverse transformation follows the same expression but at a lower range of stress (σ_{uL}^S to σ_{uL}^E).

The intensity of the transformation is governed by a stress potential law:

$$\Delta\zeta = f(\sigma, \zeta)\Delta F \quad (1.51)$$

To account for the effects of temperature on the levels of stress where transformation occurs and the small volume change associated with the stresses induced transformations a linear Drucker-Prager approach is used:

$$F = \sigma_e - p \tan\beta + CT \quad (1.52)$$

where σ_e is the von Mises equivalent stress (previously defined in equation 1.26), p is the pressure stress, β and C are material constants and T is temperature. The material parameters required to model the superelastic only behaviour of nitinol in Abaqus are

outline in Table A.1. A more detailed description of the constitutive theory can be obtained in the studies by Auricchio and Taylor [181, 182].

Table A.1: Parameters Implemented in Nitinol VUMAT.

Parameter
Austenite Elasticity (E_a)
Austenite Poisson's Ratio (ν_a)
Martensite Elasticity (E_m)
Martensite Poisson's Ratio (ν_m)
start of transformation loading (σ_l^S)
end of transformation loading (σ_l^E)
start of transformation unloading (σ_u^S)
end of transformation unloading (σ_u^E)
start of transformation stress during loading in compression (σ_{cl}^S)
strain limit
reference temperature (t_0)
density

A.4 Summary

In this chapter, an overview of the principles of continuum mechanics and finite element theory are presented. The theory outlined in this section of the thesis was applied to develop the computer simulations implemented in Chapters 3, 5 and 6 of this Thesis.